Marco Gui Alves Pinto

CdTe Matrix Polarimetric Analysis with a Crystal Polarizer

Thesis for the Master in Astrophysics and Space Instrumentation

October 2014

· U C ·

UNIVERSIDADE DE COIMBRA

Abstract

Gamma-ray astronomy is a hot topic in the scientific community. In fact, in the last decades, the gamma-ray sky has evolved from one non-existent to one thriving with different objects divided into even more classes.

The INTErnational Gamma-Ray Astrophysics Laboratory (INTEGRAL) and FERMI are the current missions that observe the gamma-ray universe with the former being sensitive to radiation up to 10 MeV and the latter from 30 MeV to energies greater than 300 GeV. Even though the FERMI satellite still has many years of activity in front of it, INTEGRAL has a shorter lifetime predicted with no foreseeable replacement.

With this in mind international consortiums have been trying to develop new instruments that would surpass INTEGRAL in both sensitivity and polarimetric performance.

With a new ESA M-class mission call imminent and with sensitivity improvements already in progress with the development of Laue Lenses and the separation of semiconductor detectors into layers, it is urgent that the polarimetric performance is also enhanced. Due to the synchrotron accelerators' busy schedule, an experiment has been developed to perform polarimetric measurements in laboratory. In this first step we seek to polarize a high energy gamma-ray beam with a target material via Compton scattering and then study its polarization parameters with a pixelated CdTe semi-conductor detector.

In a first stage simulations were performed to optimize the experiment geometry. This included an original software, to study the polarization of the initial beam in different target materials, and a study of the behaviour of the detector when irradiated with a polarized beam using the GEANT4 library developed in CERN. While the first one revealed that aluminium is the most suitable material while the second predicted a value of ~ 0.44 for the modulation factor of a 7x7 matrix and of ~ 0.36 for the one of a 3x3 matrix.

With the knowledge provided by the simulations the system was adapted, and various experimental parameters were tested in order to optimize the experiment and start studying the detectors polarimetric performance. The final assemble allowed to measure a degree of polarization of $\sim 32\%$ that can be explained by the dispersion in the initial and final beam and as well as by the noise.

Resumo

A astronomia de raios gamma é um tópico quente na comunidade científica. De facto, nas últimas décadas o céu de raios gamma evoluiu de um não existente para um com vários tipos de objetos divididos em ainda mais classes.

O INTErnational Gamma-Ray Astrophysics Laboratory (INTEGRAL) e o FERMI são as missões atuais que observam os raios gamma do universo em que o primeiro é sensível para radiação até 10 MeV e o último para energias entre 30 MeV e mais de 300 GeV. Apesar do satélite FERMI ainda ter muitos anos de atividade pela frente, o INTEGRAL tem um tempo de vida previsto mais curto sem um substituto planeado.

Com isto em mente consórcios internacionais têm tentado desenvolver instrumentos que ultrapassem o INTEGRAL tanto em sensibilidade como em performance de polarimetria.

Com a aproximação de uma nova chamada da ESA para uma missão de classe M, e com a sensibilidade melhorada através do uso de lentes de Laue e da estratificação de detetores semi-condutores, é urgente que também a capacidade polarimétrica também seja melhorada. Como os aceleradores de sincrotrão têm uma agenda preenchida, tem sido desenvolvida uma experiência para fazer medições de polarimetria em laboratório. Neste primeiro passo procura-se polarizar um feixe de raios gamma de alta energia com dispersão de Compton num material alvo e depois estudar os parâmetros da polarização com um detetor pixelizado de telureto de cádmio.

Na primeira fase fizeram-se simulações para otimizar a geometria da experiência. Estas simulações incluíram o desenvolvimento de software original, para estudar a polarização de um feixe inicial em vários materiais alvo e o estudo do comportamento do detetor quando irradiado com um feixe polarizado usando a biblioteca GEANT4 desenvolvida pelo CERN. Enquanto a primeira mostrou que o alumínio é o material mais indicado para a experiência, a segunda previu um valor de ~ 0.44 para o factor de modelação de uma matriz 7x7 e um valor de ~ 0.36 para uma matriz 3x3.

Com o conhecimento adquirido pelas simulações adaptou-se o sistema e testaram-se vários parâmetros experimentais de modo a otimizar a experiência e começar a estudar a performance polarimétrica do detetor. A montagem final permitiu medir um valor de grau de polarização de $\sim 32\%$ que pode ser explicado pela dispersão nos feixes iniciais e finais assim como pelo ruído presente.

Acknowledgements

First I would like to thank Dr. Rui Silva for suggesting the theme for this thesis and guiding me in what has been my first step in research. I can only hope to take the most out of his teachings and expertise.

To Dr. Jorge Maia I can only thank for all his support, patience and willingness to teach, his energy and enthusiasm have been contagious.

To Dr.ª Filomena dos Santos I would like to thank for her helpful advices and insights.

I would also like to thank Dr.ª Benilde de Oliveira e Costa for her help. Without it this work would not have been done.

I must also thank ICNAS, in particular Dr. Nuno Chichorro Ferreira and Dr. Sérgio Ramos for their valuable contribution to this work.

To Pedro Crispim and André Cortez my deepest thanks, I cannot begin to describe how much important your companionship was this past year.

I would also like to thank everyone in LIP, especially José Marques, for his support and encouragement, Alexandre Trindade and Américo Pereira, for all their help, and Luis Pereira, without his help with the LabView software and his insight in other matters, this work would have been a lot harder.

I would also like to thank everyone back in Fadjoja for their continuous support and friendship.

Another special thanks to all my friends in “residência S.Salvador”. You have been a second family this past years. I could not wish a different experience in Coimbra.

This list would not be complete without my friends and colleagues that shared this journey with me. I cannot mention you all but I feel I must leave a special thanks to Cristiana Francisco, Raimundo Martins, Ricardo Laborda, Diniz Sá, Gonçalo da Cruz, Natacha Leite, Luís Antunes, Afonso Sousa, Mário Sardinha, Filipe Pereira, Inês Grilo and Catarina Santos.

To finalize I must thank my family especially my parents and my sister. Without them nothing of this would have been possible. It was their comprehension, their support and their trust that carried me through all this years.

List of Contents

Abstract……………………………………………………………………………………………………….i

Resumo……………………………………………………………………………………………………iii

Acknowledgements………………………………………………………………………………………v

List of Contents…………………………………………………………………………………………vii

List of Figures……………………………………………………………………………………………xi

List of Tables……………………………………………………………………………………………xix

Acronyms………………………………………………………………………………………………xxi

Chapter 1. Introduction……………………………………………………………………………1

1.1. Motivation……………………………………………………………………………………2
1.2. Cosmic Vision…………………………………………………………………………………3
1.3. Instrumental Proposals………………………………………………………………………5
1.4. AstroMeV……………………………………………………………………………………8
1.5. Science Drivers and Instrumental Constraints……………………………………………9
1.6. Present Work…………………………………………………………………………………11

Chapter 2 – Gamma-Ray Polarization……………………………………………………………13

2.1. Polarization……………………………………………………………………………………14
2.1.1. Linear Polarization…………………………………………………………………………15
2.1.2. Elliptical Polarization………………………………………………………………………15
2.1.3. Degree and Angle of Polarization…………………………………………………………16
2.2. Emission Mechanisms…………………………………………………………………………18
2.2.1. Thermal Bremsstrahlung……………………………………………………………………18
2.2.2. Magnetic Bremsstrahlung……………………………………………………………………20
2.2.2.1. Cyclotron Emission………………………………………………………………………21
2.2.2.2. Synchrotron Emission……………………………………………………………………22
2.2.3. Magnetic Photon Splitting……………………………………………………………………25
2.2.4. Compton Scattering……………………………………………………………………………26
2.3. Scientific Interest on Gamma-Ray Astronomy…………………………………………………30
2.3.1. Supernovas……………………………………………………………………………………30
2.3.2. Black Holes and Neutron Stars………………………………………………………………32
2.3.2.1. Gamma-Ray Bursts…………………………………………………………………………32
2.3.2.2. Pulsars………………………………………………………………………………………34
2.3.2.3. Binary Systems……………………………………………………………………………35
2.3.3. The Sun and the Earth…………………………………………………………………………36
2.3.3.1. Solar Flares…………………………………………………………………………………36
2.3.3.2. Terrestrial Gamma-Ray Flashes……………………………………………………………36

Chapter 3. Gamma-ray Detection……41

3.1. General Properties……42
3.1.1. Simplified Detector Model……42
3.1.2. Sensitivity……43
3.1.3. Efficiency……43
3.1.4. Energy Resolution……44
3.1.5. Polarization Modulation Factor……46
3.1.6. Minimum Detectable Polarization……46
3.2. Detector Working Principles……47
3.2.1. Gaseous Detectors……47
3.2.2. Scintillators……49
3.2.3. Semi-Conductors……50
3.3. MeV Telescopes……53
3.3.1. Interaction of Light with Matter……53
3.3.1.1. Photoelectric Effect……53
3.3.1.2. Compton Scattering……54
3.3.1.3. Pair Production……54
3.3.2. Compton Telescopes……56
3.3.3. Pair Production Telescopes……57
3.3.4. Coded Masks……58
3.3.5. Laue Lenses……59
3.4. State of the Art……59
3.4.1. The past and the Present……59
3.4.1.1. CGRO……60
3.3.1.2. Integral……61
3.4.2. AstroMev, the future……63

Chapter 4. Compton Polarimetry……65

4.1. Rotational Polarimeters……67
4.2. Non-Rotational Polarimeters……67
4.3. Data Analysis for Non-Rotational Polarimeters……69
4.3.1. The Moving Mask Technique (MMT)……69
4.3.2. The Radial Bin Technique (RBT)……70
4.4. Systematic Effects Removal……72
4.4.1. Non-Uniform Response……72
4.4.2. Off-Axis Incidence……73
4.4.3. Background Noise……74
4.4.4. Pixellation……74
4.4.5. Full Surface Irradiation……74

Chapter 5. Experimental Setup……79

5.1. Scattering material analysis……81
5.1.1. Implementation……82

- 5.1.1.1. Photon’s Path in a Scattering Material……82
- 5.1.1.2. Intersection with the Detector……85
- 5.1.2. Results……85
- 5.2. POLCA II……87
  - 5.2.1. CZT Detector and the Front-End Electronics……88
  - 5.2.2. TAKES……90
  - 5.2.3. Data Acquisition and Quick Look S/W……90
    - 5.2.3.1. Acquisition Control……91
    - 5.3.2.2. Storage……91
    - 5.3.2.3. Data Reproduction……92
  - 5.2.4. System Adaptations……93
    - 5.2.4.1. Physical Modifications……93
    - 5.2.4.2. Software Modifications……94

Chapter 6. Polarimetry Results……97

- 6.1. Polarimetry with GEANT4……98
  - 6.1.1. Unpolarized Beam……98
  - 6.1.2. Angle of Polarization at 0 Degrees……100
  - 6.1.3. Angle of Polarization at 45 Degrees……103
  - 6.1.4. Angle of Polarization at 90 Degrees……104
  - 6.1.5. Angle of Polarization at 135 Degrees……105
- 6.2. Uniformity Tests……106
- 6.3. Energy Calibration……109
- 6.4. Experimental Work……111
  - 6.4.1. Unpolarized beam……114
  - 6.4.2. Experimental Polarimetry……116
  - 6.4.3. Final results……118

Chapter 7 – Conclusions and Future Work……125

Annex A……129

Annex B……133

List of Figures

Figure 1.1: Light absorption in the atmosphere. Here lines represent the fraction of the atmosphere that different wavelengths can travel before being absorbed. We can observe that in the gamma ray part of the spectrum light can only travel 1% of the atmosphere.

Figure 1.2: a) Chronology of space telescopes above keV energies. b) Sensitivity limits of space instruments above keV energies.

Figure 1.3: Artist conception of the GRI composed by the lens module and the focal plane module GRI.

Figure 1.4 Schematics of the DUAL instrument adapted from. In it one can see the geometry three main instruments, the ASCI, the Laue lens and the coded mask.

Figure 1.5: Representation of the CAPSiTT modules.

Figure 1.6: Schematics of the GRIPS satellite proposed in the ESA M3 call.

Figure 1.7: Concept for the PACT instrument including the Silicon tracker, the Scintillator calorimeter and the plastic anti-coincidence system.

Figure 2.1: Propagation of an electromagnetic wave with wavelength λ along the z axis. The electric and magnetic field vary in the x and y axis respectively perpendicular to each other and to the propagation direction.

Figure 2.2 – Electric field’s orientation in the polarization plane.

Figure 2.3: Radiation emission by the acceleration of an electron in the electrostatic field of a nucleus.

Figure 2.4: Degree of linear polarization given an electron of energy $10m_ec^2$.

Figure 2.5: Polar diagram for dipolar emission from cyclotron radiation. Here ε is the polarization vector of the emitted photon.

Figure 2.6: Polar diagram for dipolar emission from synchrotron radiation as seen in the observer frame.

Figure 2.7: Shape of the function F(x).

Figure 2.8: Schematics of Compton Scattering.

Figure 2.9: Differential cross-section in function of the scattering angle in logarithmic scale for the unpolarized Compton scattering. From E.B. Podgorsak, Radiation Physics for Medical Physicists.

Figure 2.10: Degree of polarization with respect to the scattering angle in Compton Scattering for several energies.

Figure 2.11 a) and b): Azimuthal distribution of 100% polarized beam of photons emerging from Compton scattering. In the left side, the polar angle θ is kept constant at 90°. In the right one it is the energy that is kept constant at 200 keV while θ varies.

Figure 2.12: Supernova classification scheme.

Figure 2.13: Average polarization of long GRBs as a function of their duration (Shaviv and Dar, 1995).

Figure 3.1: Evolution of the current produced by an interaction within the detector with time.

Figure 3.2: Representation of the FWHM for an energy curve and the superposition of two of such curves.

Figure 3.3: Basic cylindrical model of a gaseous detector.

Figure 3.4: Number of ions collected as a function of the voltage applied in gaseous detectors.

Figure 3.5: Scintillator coupled with a Photo Multiplier Tube.

Figure 3.6: Band structure of electron energies in insulators and semiconductors. The size of the gap determines if a crystal is an insulator or a semiconductor [1].

Figure 3.7: Schematics of the joined p an n doped semiconductors.

Figure 3.8: On the left a photon with energy hv interacts with an electron in the k-band. On the right the electron that interacted with the gamma-ray leaves the atom with total energy equal to the photon’s energy subtracted by the bound energy of the electron.

Figure 3.9: Pair production in the presence of a nuclei.

Figure 3.10: Dominance of photon interactions with matter as a function of their energy and the atomic number of the matter they interact with.

Figure 3.11: Concept of a Compton Telescope.

Figure 3.12: Schematic of a coded-mask subject to two different fluxes.

Figure 3.13: Timeline of the development of gamma-ray astronomy up to 1997.

Figure 3.14: Schematics for the COMPTEL instrument aboard the CGRO [3].

Figure 4.1: Azimuthal angular distribution of a polarized beam of photons after being Compton scattered.

Figure 4.2 Principle of operation of a Compton polarimeter.

Figure 4.3: Compton scattering in a pixelated CZT detector.

Figure 4.4: Schematics for the 7x7 pixelated detection area.

Figure 4.5: Illustration of the four quadrants in the MMT in the initial state and when rotated by an angle φ. Each quadrant is identified as N_1, N_2, N_3 and N_4 and with the colours blue, red, green and yellow respectively.

Figure 4.6: Illustration of the MMT using a small window. The angles used are exaggerated for better illustration of the principle but there's no loss of generality transitioning to bins of 24° or 15°.

Figure 4.7: Referential for the area calculations. The origin corresponds to the center of the central pixel in the matrix.

Figure 4.8: Events in a 4x4 matrix reduced to a central pixel in a 7x7 matrix. The black pixel corresponds to the initial interaction and the red and blue lines represent the initial and final pixel of double interactions.

Figure 5.1: Beam polarization simplified geometry. In reality photons leaving the source are not parallel to each other.

Figure 5.2: Flowchart of the simulation about the polarization of a beam by Compton scattering in a scattering material.

Figure 5.3: Scattering material's reference frame.

Figure 5.4: Schematics for the CZT detector and all its' components [1] [2]. In it is possible to see the 3 main components, the 256 CZT pixel detector connected to the front-end electronics, the TAKES unit that treats the signals generated in the detector and finally the Data Acquisition Control and Quick Look S/W that finalizes the signal treatment and displays the information.

Figure 5.5: Pixel association with the 8 ASIC channels. Pixel numbers start at 85 because not all the matrix is being used.

Figure 5.6: The top figure shows the output channels of the ASIC channels. Pins from 1 to 16 correspond to pixels in the detector that depend on the ASIC channel. The other 11 pins are connected to the ground. The bottom figure shows the input of each channel in the TAKES unit. After the inversion pins 1 through 21 are connected to ground while the others connect pixels to the TAKES. The association between both is linear, pin 1 in the ASIC connects to pin 37 in TAKES, pin 2 to 36 and so on.

Figure 5.7: Meaning of the 16 bit words. The end of event bit is only one for the last interaction in a multiple event. The TAKES outputs data in a serial form.

Figure 5.8: Acquisition interface. In this tab of the software selection options regarding the ASIC channel used (top left nob), the use of a lookup table for pixel number conversion (bottom left switch), limitation of the acquisition duration regarding either time or the number of counts (top right) and the number of pixels connected and existent in the detector.

Figure 5.9: Storage interface of the LabView S/W. It includes a switch in top left side that dictates the data type of the stored information and three text boxes where the name of the file, suffix and comments can be inserted.

Figure 5.10: Full interface of the LabView S/W.

Figure 5.11: Algorithm used to change the ASIC channel to read.

Figure 6.1: Double interaction matrix for an unpolarized beam. The number of interactions increases from black to white.

Figure 6.2: N(θ) distribution. The red line is the fitted function. The fit is obtained with the MATLAB "fit" function. This function uses the least squares method to fit the data to a model function, in this case a $Acos(2\theta + \varphi) + C$ where A, φ and C are the coefficients to be calculated.

Figure 6.3: Double interaction matrix for a 100% polarized beam with its angle of polarization at 0°. The number of interactions increases from black to white.

Figure 6.4: N(θ) distribution for a 100% polarized beam with its angle of polarization at 0°. The red line is the fitted function. The equation of this function its presence is merely representative.

Figure 6.5: Q(θ) distribution for a 100% polarized beam with its angle of polarization at 0° fitted to a $\cos(2\theta)$ form. The red line is the fitted function.

Figure 6.6: Measured vs Expected degree of polarization of a simulation with a beam at 0 degree angle with the horizontal axis.

Figure 6.7: Measured vs Expected degree of polarization of a simulation with a beam at a 45 degree angle with the horizontal axis.

Figure 6.8: Measured vs Expected degree of polarization of a simulation with a beam at a 90 degree angle with the horizontal axis.

Figure 6.9: Measured vs Expected degree of polarization of a simulation with a beam at a 135 degree angle with the horizontal axis.

Figure 6.10 a) and b): In the left image one can see the lead collimator with a 0.5 mm aperture and a 3 cm thickness where the 122 keV source was placed. The circle to its right is an opening in the support table where the collimator is placed. In the right image the collimator is already placed in the table. It remains in the same position while the detector is moved from pixel to pixel.

Figure 6.11: A possible path for the uniformity tests. This was not the one used since many of the channels had pixels with a lot of background that did not allow an easy reading of the irradiated pixel. In this case pixel measurements started in pixel 217 and followed no specific order.

Figure 6.12: Intensity map from the uniformity tests on the full active detector surface.

Figure 6.13: Intensity map from the uniformity tests on the 4x4 matrix. The numbers in each square correspond to the pixel number

Figure 6.14: Calibration plot of pixel 234.

Figure 6.15: Assemble of the experiment (vou tirar a fotografia amanhã ou 2ª feira. In we can see the collimator (object A), the detector (object B), the supports for the scattering material (object C) and the scattering material (object D) notice that the supports and the scattering material are made of the same element.

Figure 6.16: Shielded version of the experiment. Notice that the aluminum supports are no longer included and that the support is now made with blocks of lead. The spacing between the lead has the dimensions of the 4x4 matrix used, 1.5 cm.

Figure 6.17: Spectrum of the noise in the pixel 201 for a 200000s acquisition. Only signals that were counted as coincidences are considered.

Figure 6.18: Double interaction matrix generated by a 200000s acquisition with no source.

Figure 6.19: Double interaction matrix for an unpolarized 511 keV beam. The number of interactions increases from black to white.

Figure 6.20: N(θ) distribution for the unpolarized 511 keV beam with its angle of polarization at 0°. The red line is the fitted function.

Figure 6.21: Double interaction matrix for a setup where the polarization beam expected to be at 0°.

Figure 6.23: Double interaction matrix for a setup where the polarization beam expected to be at 45°.

Figure 6.25: Double interaction matrix for a setup where the polarization beam expected to be at 90°.

Figure 6.27: N(θ) distribution for the unpolarized 511 keV beam with its angle of polarization at 0°. The red line is the fitted function.

Figure 6.28: N(θ) distribution for a setup where the polarization beam expected to be at 0°.The red line is the fitted function

Figure 6.29: N(θ) distribution for a setup where the polarization beam expected to be at 45°.The red line is the fitted function

Figure 6.30: N(θ) distribution for a setup where the polarization beam expected to be at 90°.The red line is the fitted function.

Figure 6.31: Different trajectories for photons leaving the source and interacting in the scattering material.

Figure 6.32: Schematic view of central pixels irradiated by a polarized inclined beam at angle θ with respect to the detector optical axis. In this case photons crossing the irradiated pixels surface will not be scattered uniformly inside this pixels. Preferentially they will be scattered closer or inside the first order pixels laying in the horizontal projections of the photon propagation direction.

Figure A.1: Mass attenuation coefficient for the Photoelectric effect and Compton scattering in Silicon for the 0.1-1MeV range.

Figure A.2: Mass attenuation coefficient for the Photoelectric effect and Compton scattering in Germanium for the 0.1-1MeV range.

Figure A.3: Mass attenuation coefficient for the Photoelectric effect and Compton scattering in CdTe for the 0.1-1MeV range.

Figure A.4: Mass attenuation coefficient for the Photoelectric effect and Compton scattering in a Plastic Scintillator for the 0.1-1MeV range.

Figure A.5: Mass attenuation coefficient for the Photoelectric effect and Compton scattering in Aluminum for the 0.1-1MeV range.

Figure A.6: Mass attenuation coefficient for the Photoelectric effect and Compton scattering for a league of stainless steel for the 0.1-1MeV range.

Figure B.1: Double interactions matrix (a) and Q distribution fitted to a cos(2θ) function for a 80% polarized beam with its polarization vector at 0°

Figure B.2: N distribution fitted to a cos(2θ) function for a 80% polarized beam with its polarization vector at 0°.

Figure B.3: Double interactions matrix (a) and Q distribution fitted to a cos(2θ) function for a 60% polarized beam with its polarization vector at 0°.

Figure B.4: N distribution fitted to a cos(2θ) function for a 60% polarized beam with its polarization vector at 0°.

Figure B.5: Double interactions matrix (a) and Q distribution fitted to a cos(2θ) function for a 40% polarized beam with its polarization vector at 0°.

Figure B.6: N distribution fitted to a cos(2θ) function for a 40% polarized beam with its polarization vector at 0°.

Figure B.7: Double interactions matrix (a) and Q distribution fitted to a cos(2θ) function for a 20% polarized beam with its polarization vector at 0°.

Figure B.8: N distribution fitted to a cos(2θ) function for a 20% polarized beam with its polarization vector at 0°.

Figure B.9: Double interactions matrix (a) and Q distribution fitted to a cos(2θ) function for a 100% polarized beam with its polarization vector at 45°.

Figure B.10: N distribution fitted to a cos(2θ) function for a 100% polarized beam with its polarization vector at 45°.

Figure B.11: Double interactions matrix (a) and Q distribution fitted to a cos(2θ) function for a 80% polarized beam with its polarization vector at 45°.

Figure B.12: N distribution fitted to a cos(2θ) function for a 80% polarized beam with its polarization vector at 45°.

Figure B.13: Double interactions matrix (a) and Q distribution fitted to a cos(2θ) function for a 60% polarized beam with its polarization vector at 45°.

Figure B.14: N distribution fitted to a cos(2θ) function for a 60% polarized beam with its polarization vector at 45°.

Figure B.15: Double interactions matrix (a) and Q distribution fitted to a cos(2θ) function for a 0% polarized beam with its polarization vector at 45°.

Figure B.16: N distribution fitted to a cos(2θ) function for a 40% polarized beam with its polarization vector at 45°.

Figure B.17: Double interactions matrix (a) and Q distribution fitted to a cos(2θ) function for a 20% polarized beam with its polarization vector at 45°.

Figure B.18: N distribution fitted to a cos(2θ) function for a 20% polarized beam with its polarization vector at 45°.

Figure B.19: Double interactions matrix (a) and Q distribution fitted to a cos(2θ) function for a 100% polarized beam with its polarization vector at 90.

Figure B.20: N distribution fitted to a cos(2θ) function for a 100% polarized beam with its polarization vector at 90.

Figure B.21: Double interactions matrix (a) and Q distribution fitted to a cos(2θ) function for a 80% polarized beam with its polarization vector at 90.

Figure B.22: N distribution fitted to a cos(2θ) function for a 80% polarized beam with its polarization vector at 90.

Figure 23: Double interactions matrix (a) and Q distribution fitted to a cos(2θ) function for a 60% polarized beam with its polarization vector at 90.

Figure B.24: N distribution fitted to a cos(2θ) function for a 60% polarized beam with its polarization vector at 90.

Figure B.25: Double interactions matrix (a) and Q distribution fitted to a cos(2θ) function for a 0% polarized beam with its polarization vector at 90°

Figure B.26: N distribution fitted to a cos(2θ) function for a 40% polarized beam with its polarization vector at 90°.

Figure B.27: Double interactions matrix (a) and Q distribution fitted to a cos(2θ) function for a 20% polarized beam with its polarization vector at 90°.

Figure B.28: N distribution fitted to a cos(2θ) function for a 20% polarized beam with its polarization vector at 90°.

Figure B.29: Double interactions matrix (a) and Q distribution fitted to a cos(2θ) function for a 100% polarized beam with its polarization vector at 135°.

Figure B.30: N distribution fitted to a cos(2θ) function for a 100% polarized beam with its polarization vector at 135°.

Figure B.31: Double interactions matrix (a) and Q distribution fitted to a cos(2θ) function for a 80% polarized beam with its polarization vector at 135°.

Figure B.32: N distribution fitted to a cos(2θ) function for a 80% polarized beam with its polarization vector at 135°.

Figure B.33: Double interactions matrix (a) and Q distribution fitted to a cos(2θ) function for a 60% polarized beam with its polarization vector at 135°.

Figure B.34: N distribution fitted to a cos(2θ) function for a 60% polarized beam with its polarization vector at 135°.

Figure B.35: Double interactions matrix (a) and Q distribution fitted to a cos(2θ) function for a 0% polarized beam with its polarization vector at 135°.

Figure B.36: N distribution fitted to a cos(2θ) function for a 40% polarized beam with its polarization vector at 135°.

Figure B.37: Double interactions matrix (a) and Q distribution fitted to a cos(2θ) function for a 20% polarized beam with its polarization vector at 135°.

Figure B.38: N distribution fitted to a cos(2θ) function for a 20% polarized beam with its polarization vector at 135°.

List of Tables

Table 1.1: Science topics in the MeV range and the performances they require. Blank spaces concern properties that are not restrained by the source requirements. MDP stands for Minimum Detectable Polarization.

Table 2.1: Duration and polarization limits of some GRBs.

Table 5.1: Results of the polarization of a beam scattered in different materials. The multiple interactions % refers to the photons that interacted more than once in the scattering volume.

Table 5.2: Efficiency, average energy and average polarization of photon beams generated by different scattering materials.

Table 6.1: Results for the simulations with polarization at a 0 degree angle with the horizontal axis.

Table 6.2: Results for the simulations with polarization at a 45 degree angle with the horizontal axis.

Table 6.3: Results for the simulations with polarization at a 90 degree angle with the horizontal axis.

Table 6.4: Results for the simulations with polarization at a 135 degree angle with the horizontal axis.

Table 6.5: Results for the energy calibration of each pixel. The slope and the intercept were calculated with a linear fit.

Table 6.6: Measured polarization angle, modulation factor and estimated polarization degree.

Acronyms

ASCI – All-Sky Compton Imager
ASIC – Application Specific Integrated Circuits
BATSE – Burst and Transient Source Experiment
CdTe – Cadmium Telluride
CGRO – Compton Gamma–Ray Observatory
CMO – Coded Mask Optic
COMPTEL – Compton Telescope
CsI – Caesium Iodide
EGRET – Energetic Gamma Ray Experiment Telescope
ESA – European Space Agency
ESFR – European Synchrotron Radiation Facility
FE – Front End
FOV – Field of View
FWHM – Full Width at Half Maximum
Ge – Germanium
GRB – Gamma–Ray Burst
GRI – Gamma–Ray Imager
GRM – Gamma–Ray Monitor
INTEGRAL – INTErnational Gamma-Ray Astrophysics Laboratory
IBIS – Imager On-Board INTEGRAL
MMT – Moving Mask Technique
MDP – Minimum Detectable Polarization
OSSE – Oriented Scintillation Spectrometer Experiment
PACT – Pair And Compton Telescope
PMT – Photo Multiplier Tube
RBT – Radial Bin Technique
ROI – Region Of Interest
Si – Silicon
SN – SuperNova
SPI – SPectrometer on INTEGRAL
TGF – Terrestrial Gamma-ray Flash
XRM – X–Ray Monitor

Chapter 1

Introduction

1.1– Motivation

Polarization of high energy sources is a key observational parameter to understand the emission mechanisms and geometry of a wide number of cosmic objects such as gamma-ray bursts, pulsars and others, where some degree of polarization is expected [3]. Even though this has been known for quite some time in the scientific community, no dedicated polarimeter has ever been launched in either a satellite or a balloon mission. Since earth telescopes are not an option due to the atmosphere's opacity to short wavelengths (see figure 1.1), this field remains fairly unexplored [4].

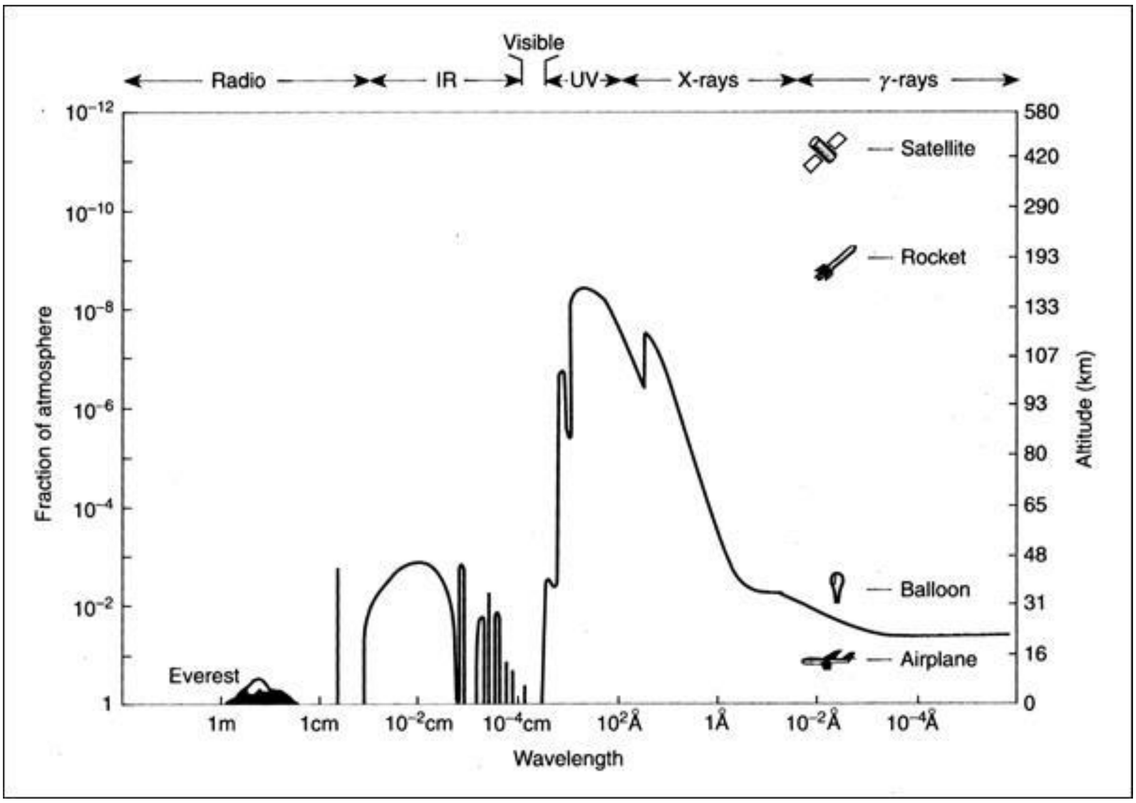

Figure 1.1: Light absorption in the atmosphere. Here lines represent the fraction of the atmosphere that different wavelengths can travel before being absorbed. We can observe that in the gamma ray part of the spectrum light can only travel 1% of the atmosphere [1].

In the same regard, sensitivity in the MeV range (0.1-10MeV) is also low in respect to other energies.

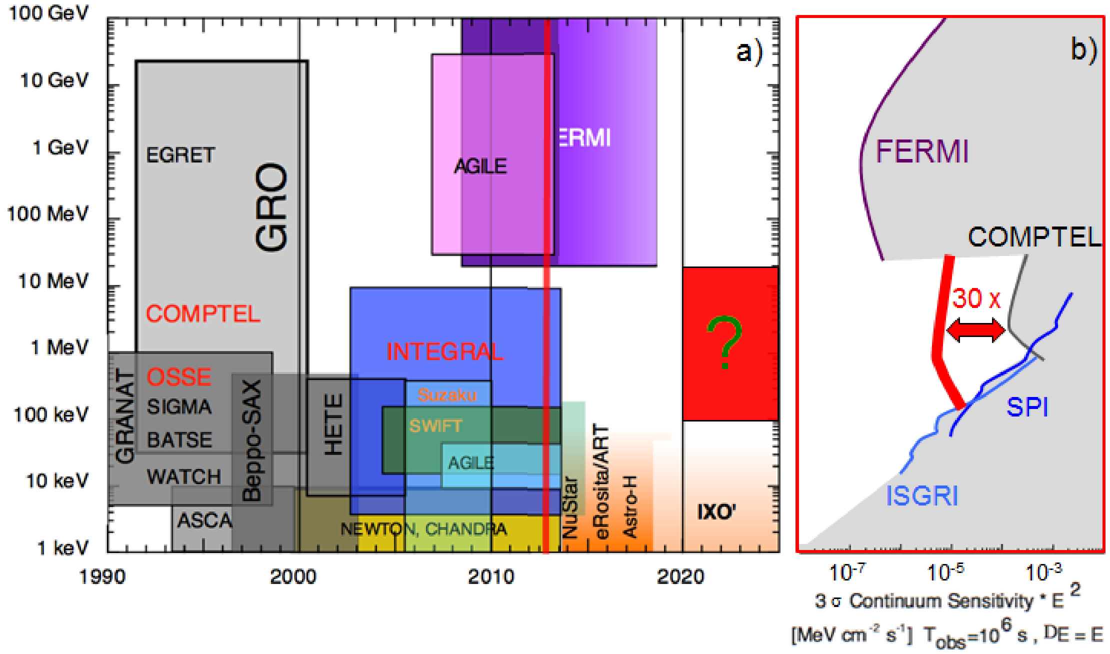

Figure 1.2: a) Chronology of space telescopes above keV energies. b) Sensitivity limits of space instruments above keV energies [2]. A future MeV region gamma-ray mission is expected to improve 30 to 100 times observation sensitivity.

As it can be seen in the left part of the image above, the mid to high end of the spectrum is a lot less covered than the low end. Despite discrepancy in number of missions, the high energy satellite FERMI provides good sensitivity in the GeV range. However, in the intermediate energies there is a noticeable gap in sensitivity with the COMPton TELescope (COMPTEL) and the SPectrometer on INTEGRAL (SPI) instruments aboard the Compton Gamma-Ray Observatory (CGRO) and INTEGRAL satellites respectively lagging behind their counterparts in other energies. Furthermore, if the AL – INTErnational Gamma-Ray Astrophysics Laboratory (INTEGRAL) mission is discontinued by 31st December 2016 (foreseen date) we will be blind to these wavelengths [6].

The scientific community has been exploring ways to launch a new mission that would not only, improve the sensitivity by 2 orders of magnitude, but also, allow polarimetric measures to be performed.

1.2 – Cosmic Vision

The Cosmic Vision is the European Space Agency's (ESA) current program for future missions that should be launched between 2015 and 2025. There are four main themes that comprise this program and that will be the focus of its missions [6]:

Theme 1 – What are the conditions for planet formation and the emergence of life?

Theme 1 focuses on the long-term question about the emergence of life. To investigate this matter we have to look not only to the first chemical reaction that originated living beings but also to the steps that made this reaction possible starting with the Big Bang and leading to the formation of stars and the planets that orbit them [7].

Theme 2 – How does the Solar System work?

In the same spirit of theme 1, theme 2 explores the development of our own Solar System, a case of success in the life department. Understanding the evolution of our home system, its planets, and shielding mechanisms against harmful radiation can provide clues about our origin and about where to look for other life forms [8].

Theme 3 – What are the fundamental physical laws of the Universe?

Another prospect of modern physics lies in the extreme energies and temperatures where our current knowledge doesn’t apply. These conditions are found in the first fraction of seconds after the Big Bang when neither electrons nor protons existed. The scientific community expects laws and forces to converge into a unified theory in this limit [9].

Theme 4 – How did the Universe originate and what is it made of?

Last but not least the 4th theme tackles a subject of the same nature as the first one. Since the dawn of mankind that we search for the origin of the Universe and of what it is made of. By acknowledging that the Earth is only one of many objects that orbit the Sun which by its turn orbits a common spiral galaxy all the way to perceiving the Big Bang as the initial point of the Universe, we have been brought step by step closer to the answer. With this theme another step in this quest is sought [10].

As we will see most of the science done in the MeV range meets the program in this last theme particularly in its subsection “4.3 -The evolving violent Universe”. Here the concern is about objects subject to extreme conditions of gravity, temperature and density like black holes or neutron stars, drivers of the birth and evolution of galaxies and typical gamma-ray sources. The other subsections for this theme are “4.1 – The early Universe” and “4.2 – The Universe taking shape”. These themes concern both expansions of the universe its first structures respectively.

Currently the program has already selected 6 missions, 3 of which belong to the M-class (Medium sized). These 3 M-class missions, Solar Orbiter [M1], Euclid [M2] and PLATO [M3] have been contested by three MeV Telescope proposals GRI [M2], DUAL, CAPSiTT and GRIPS [M3] [11] .

The three concurrent proposals for MeV telescopes in the M3 call showed different views in the scientific community about the instrumental concept and it is up to it to further research and discuss what the best concept is.

1.3 – Instrumental Proposals

Each of these proposals had different approaches to the problem leading to the development of several instruments for each mission.

GRI (Gamma Ray Imager)

GRI’s proposal consisted in a standard telescope design with a focusing Laue lens and a pixelated stack of Ge, CdTe, CZT or Si detector layers. Both parts would be in formation flight at a distance of less than 100m as shown in figure 1.3. While the Laue lens would work as a radiation concentrator, the detector would perform position sensitive imagery allowing both spectrometric and polarimetric measurements. Both the Laue Lens and the formation flight were still developing techniques at the time [2].

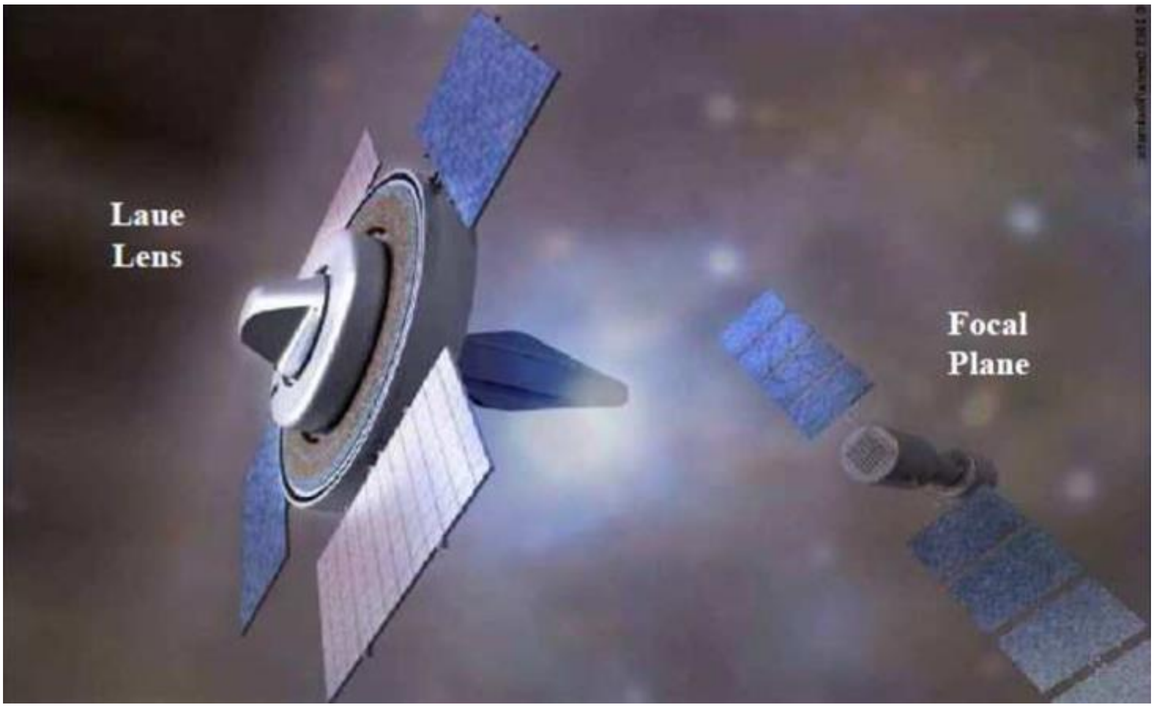

Figure 1.3: Artist conception of the GRI composed by the lens module and the focal plane module [2].

DUAL

The DUAL mission continued the work of GRI featuring many of the same members. Once again a standard telescope design was considered consisting of a Laue Lens and a pixelated stack of Ge detector layer, the All-Sky Compton Imager (ASCI) (subject of this work), that would work both as a focal plane for the Laue Lens and as an all-sky detector. This time however, as it can be seen in figure 1.4, both instruments would be connected by a mast of 30m and would be joined by a 3rd instrument, the Coded-Mask Optic (CMO). The latter would allow substantial increase of the angular resolution to 10'-40' in the Galactic Center and Bulge and an increase in the signal to noise ratio [12].

CAPSiTT

CAPSiTT is singular in regards to other proposals as it only carries one instrument. This instrument is a combined Compton and pair telescope consisting in a stack of silicon stripped detectors with a total size of 1.2x1.2x0.9m and divided in 6x6 detection units [13]. Below a representation of the instrument with its 36 modules can be seen.

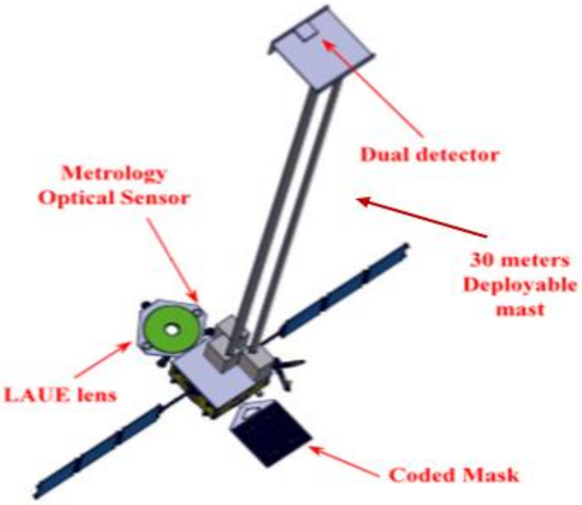

Figure 1.4: Schematics of the DUAL instrument adapted from [12]. In it one can see the geometry three main instruments, the ASCI, the Laue lens and the coded mask.

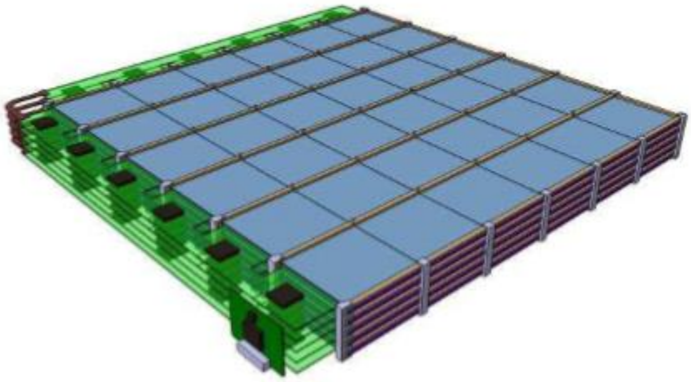

Figure 1.5: Representation of the CAPSiTT modules [13].

GRIPS

The German mission GRIPS presented 3 instruments, a Gamma Ray Monitor (GRM), an imaging X-ray telescope (XRM) and an optical/NIR telescope. Only the first is important to our discussion and as such I will not write about the other two, leaving only a note that these two additional instruments are an effort to have additional detail on Gamma Ray Bursts (GRB) in the same way the SWIFT satellite did, while at the same time expanding the science it can do. GRM consists in two main parts, an electron tracker based on Silicon detectors and a plethora of LaBr3 scintillator crystals functioning as a calorimeter [14]. The proposed satellite and its instruments are schematized below.

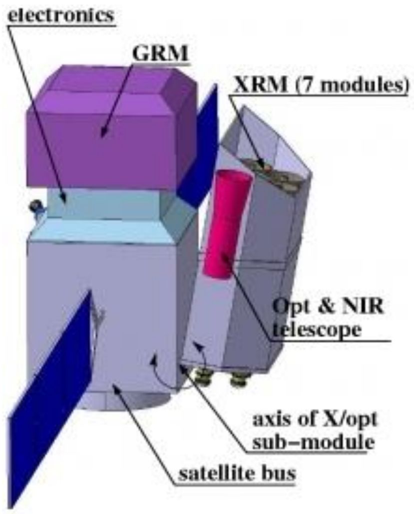

Figure 1.6: Schematics of the GRIPS satellite proposed in the ESA M3 call [14].

All proposals had in common the use of a semiconductor as the basis of the gamma detector either supported by other instruments such as a Laue lens or as a standalone device as in the case of CAPSiTT. The semiconductor material on the other hand was torn between Silicon and Germanium leaving CdTe (or CZT) as a contender. Since all materials have their pros and cons it is up to the scientific community's job to choose the best according to the mission's parameters.

1.4 – AstroMeV

Following the last M-call and the issues that were acknowledged, an international consortium, the AstroMeV, was created. The collaboration objectives are to discuss the science drivers behind a MeV mission, the design of the instruments that will meet the mission requirements, and finally the implementation of such a mission, if chosen in announcements of opportunity from space agencies, either the M4-call from ESA or others. As a part of this consortium it is our work to study the polarimetric capabilities of the main instrument [15].

With this in mind there have been 3 instruments under study by the different groups, the Pair And Compton Telescope (PACT), a wide field camera to study polarization of X and Gamma-ray sources (WPOL) and ASCI [15]. These instruments are all based on the proposals presented in section 1.3.

PACT is a gamma-ray tracker made of stacked Silicon stripped detectors joined by position-sensitive scintillator modules working as a calorimeter (same as in GRIPPS). Such device would cover a wide range of wavelengths from ~100keV to ~100MeV surpassing by far the instruments used so far [16]. A schematics of the instrument can be found in figure 1.7.

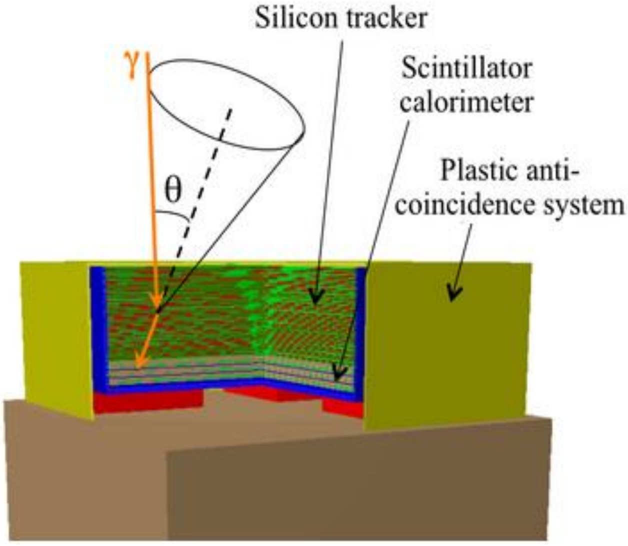

Figure 1.7: Concept for the PACT instrument including the Silicon tracker, the Scintillator calorimeter and the plastic anti-coincidence system [16].

WPOL on the other hand is an auxiliary instrument designed to map and measure polarized sources in our galaxy and to alert the main instrument and the scientific community when a transient object is detected. The detector comprises a coded mask, a double sided stripped silicon detector, a passive collimator and a tungsten mask.

1.5 – Science drivers and Instrumental Constraints

There are two main constraints associated with a space mission. The first one is in the logistics department concerning weight and size of the payload, funding of the devices, among others. The second one the quality of the observations expected.

In order to assess the latter, one must evaluate the science drivers behind the mission and the performances they require from observational instruments.

The MeV domain is rich in astronomical sources each one with its own peculiarities. In the following table a list of some of these sources along with the parameters they impose on the mission is presented.

Source	Spectral Resolution (ΔE/E @ Energy)	Line Sensitivity (@ Energy) ($cm^{-2}s^{-1}$,3σ, Ms)	Cont. Sensitivity ($cm^{-2}s^{-1}.keV^{-1}$, $\Delta E = E, 3\sigma, \mathrm{Ms}$)	Polarimetric Capability (Minimum Polarization Fraction in Crab Sources in 1 Ms)
Galactic Center	3-5% @4.4 MeV	$< 10^{-5}$@4.4 and 6.2 MeV	3.12 $eV.cm^{-2}.s^{-1}$	
Core Collapse SN	0.3%	10^{-6}@@ 847 keV 10^{-7}@@ 415 keV	10^{-7}@ 100 keV	
Gamma ray lines from X-ray binaries		0.5% @511 keV 1% @1.5 MeV 0.5% @2.2 MeV	10^{-6} @511 keV $7 * 10^{-7}$@1.5 MeV 10^{-6}@2.2 MeV	10% @ 1 MeV
Black Holes and accreting objects			10^{-9} @1 MeV	10% @1 MeV
Gamma-Ray Bursts	<10% @ 300 keV		5-6x10^{-8}@ 1 MeV	<10%
Magnetars and isolated Pulsars		<10%	30x COMPTEL (figure 1.1 a)	1%
Pulsar wind Nebulae			$3 * 10^{-9}$ @ 1 MeV	0.2%
Dark Matter annihilation or decay	10^{-6}	10^{-6} @ 511 keV	10^{-6}– 10^{-7}@1 MeV	

Table 1.1: Science topics in the MeV range and the performances they require. Blank spaces concern properties that are not restrained by the source requirements [11]. MDP stands for Minimum Detectable Polarization and will be discussed in chapter 3.

At this point it is easy to realise why a MeV range mission is so appealing. The science drivers are vast and make up some of the most fascinating objects in the Universe. In regard to the present work we can see that it is expected that many of these sources are polarized even if by only a small factor in some cases.

1.6– Present work

In the present work the polarimetric performance of the last instrument, ASCI, in the soft gamma spectrum is studied. From the four semiconductor materials considered only CZT is used.

To analyse its polarimetric capabilities, first, a uniformity test was made to each pixel which will allow correcting for the efficiency differences between pixels.

After this study it was necessary to focus a polarized beam of photons in the detector. In order to polarize it, a target material is placed between the detector and the source at a right angle. This will provide the polarization of the beam via Compton scattering. The distribution of the double interactions inside the detector when it is irradiated by the polarized beam will then allow to measure the polarization and the angle of polarization of the beam.

In the first three chapters the physics behind the polarization mechanisms of gamma radiation, the instruments that detect them and the polarimetry techniques developed to measure it will be discussed.

In chapter five the experimental setup is discussed. This includes the simulations that were made to optimize the efficiency of the experiment as well as a discussion about the detector at hand, the electronics, the acquisition system and the adaptations that were made to make this work possible

Chapter six regards the polarimetry work that was done. This included simulations with the GEANT4 library and the experimental work that required uniformity tests, energy calibration of each pixel, and the actual experiment made to attest the detectors polarimetric capabilities.

Finally, in chapter seven the conclusions and the future work are presented.

References

[1] Léna, P., “Astrophysique – Méthodes physiques de l’observation”, 2nd edition,

InterÉdition/CNRS Éditions (1996)

[2] P.I. Jürgen Knödlseder, “GRI exploring the extremes”, submitted proposal to Cosmic

Vision 2015-2025 call for missions, June 2007

[3] CdZnTe Focal Plane Polarimetric Performances for a Laue Lens Point Spread Function, Curado et al, IEEETRANSACTIONSONNUCLEARSCIENCE,VOL.59,NO.4,AUGUST2012.

[4] F. Lei, A. J. Dean, and G. L. Hills, “Compton Polarimetry in Gamma-

Ray Astronomy”, *Space Science Review*, Vol. 82, p. 309, (1997)

[5] http://sci.esa.int/integral/47360-fact-sheet/

[6] http://sci.esa.int/cosmic-vision/46510-cosmic-vision/

[7] http://sci.esa.int/cosmic-vision/38658-cosmic-vision-2015-2025-planets-and-life/

[8] http://sci.esa.int/cosmic-vision/38658-cosmic-vision-2015-2025-the-solar-system/

[9] http://sci.esa.int/cosmic-vision/38658-cosmic-vision-2015-2025-the-fundamental-laws/

[10] http://sci.esa.int/cosmic-vision/38658-cosmic-vision-2015-2025-the-universe/

[11] Seminaire de Prospective Scientifique 2014 Appel a Idees, CNES

[12] “A DUAL mission for nuclear astrophysics”, P. von Ballmoos, J. Alvarez, N. Barrière, S. Boggs, A. Bykov, J. M. D. Velayos, F. Frontera, L. Hanlon, M. Hernanz, E. Hinglais, J. Isern, P. Jean, J. Knödlseder, L. Kuiper, M. Leising, B. Pirard, J. P. Prost, R. M. Curado da Silva, T. Takahashi, J. Tomsick, R. Walter, A. Zoglauer, Experimental Astronomy vol 33, 2012, DOI: 10.1007/s10686-011-9286-6.

[13] F. Lebrun et al., “CAPSiTT: a sensitive 100 keV – 100 MeV all sky survey”, Proceedings of Science (INTEGRAL 2010) 034.

[14] http://www.grips-mission.eu/?article=4

[15] http://astromev.in2p3.fr/

[16] http://astromev.in2p3.fr/?q=aboutus/pact

[17] http://astromev.in2p3.fr/?q=aboutus/wpol

Chapter 2

Gamma-ray Polarization

It was Maxwell who first calculated the velocity of electromagnetic waves and inferred that light must be one of such waves [1]. In fact the plane wave solution to Maxwell's equations shows us that both electromagnetic waves and light have the same speed of propagation. As such we expect to find the same properties in light as in electromagnetic waves in particular polarization.

2.1 – Polarization

Polarization refers to the oscillation orientation of waves. In this regard it is easy to see that waves are required to oscillate in more than one direction in order for this property appear, since otherwise there is only one possible orientation making it irrelevant to talk about its polarization.

Since light is a propagation of an electric field **E** and a magnetic field **B** both perpendicular to each other and to the direction of motion as represented in figure 2.1, light's electric field can follow any direction along π.

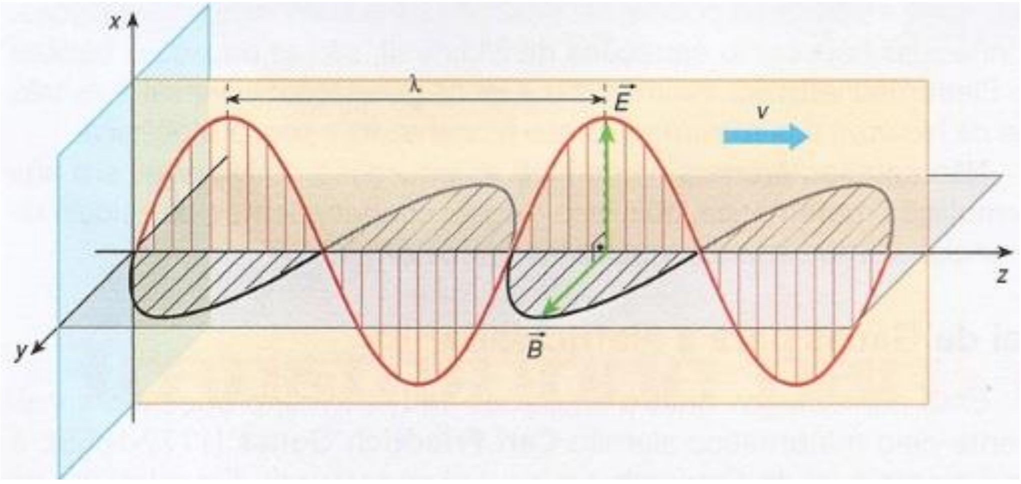

Figure 2.1: Propagation of an electromagnetic wave with wavelength λ along the z axis. The electric and magnetic field vary in the x and y axis respectively perpendicular to each other and to the propagation direction [2].

In the figure above we have the propagation of an electromagnetic wave along the z axis while the electric and magnetic field are coincident with the x and the y axis respectively. There is no restriction in the **E** orientation in the plane normal to the propagation direction, i.e., if z is fixed and θ is the angle between the x axis and **E** there is no value that θ cannot have as long as **B** makes the same angle with the y axis. The polarization vector **P** can be defined by its relation with **E** according to the following equation:

$$\boldsymbol{P} = \frac{\boldsymbol{E}}{|\boldsymbol{E}|} \tag{2.1}$$

This relation establishes that the direction the polarization vector is the same as the direction of the electric field. Since we are only interested in the direction of the vector rather than its magnitude, we can speak of one instead of the other.

2.1.1-Linear polarization

When the electric field's direction is the same for a group of waves (beam of photons) we define the beam as linearly polarized. One such beam can also be only partially polarized if only a fraction of the waves oscillate in the same direction while the remaining ones oscillate in all other directions.

2.1.2-Eliptical Polarization

Let us now consider two waves with perpendicular fields $(\boldsymbol{E_1}, \boldsymbol{B_1})$ and $(\boldsymbol{E_2}, \boldsymbol{B_2})$ respectively. We can omit all calculations made on $\vec{B}$ since it has the same shape as **E** with a 90° rotation in the polarization plane. The equations that describe the electric fields $\boldsymbol{E_1}$ and $\boldsymbol{E_2}$ in this plane are in a point in space:

$$\begin{cases} E_x = E_{0x}\cos(\omega t) \\ E_y = E_{0y}\cos(\omega t + \varphi) \end{cases} \tag{2.2}$$

Where ω is the frequency of the wave and φ is the phase between solutions. Expanding the cosine in the second equation and rewriting the first we get:

$$\begin{cases} \cos(\omega t) = \frac{E_x}{E_{0x}} \\ E_y = E_{0y}\left[\cos(\omega t)\cos(\varphi) - \sin(\omega t)\sin(\varphi)\right] \end{cases} \tag{2.3}$$

Rearranging the second equation:

$$\begin{cases} \cos(\omega t) = \frac{E_x}{E_{0x}} \\ \sin(\omega t)\sin(\varphi) = \frac{E_x}{E_{0x}}\cos(\varphi) - \frac{E_y}{E_{0y}} \end{cases} \tag{2.4}$$

Squaring and adding both equations we obtain:

$$sin^2(\varphi) = \left(\frac{E_x}{E_{0x}}\right)^2 + \left(\frac{E_y}{E_{0y}}\right)^2 - 2\frac{E_x}{E_{0x}}\frac{E_y}{E_{0y}}\cos(\varphi) \tag{2.5}$$

This is the equation of an ellipse. Hence we conclude that an electromagnetic wave's electric field will describe an ellipse in the polarization plane with z constant. There are however some special cases dependent on the phase value. For instance if $\varphi = 0$ or $\varphi = \pi$ the equation will reduce to that of a line thus making the polarization linear. Another important result comes when $\varphi = \frac{\pi}{2}$ and $\varphi = \frac{3\pi}{2}$. For this values the polarization will be elliptical with retrograde motion in the first case and direct in the second for an observer at $z > 0$. Both last cases become circular when $E_{0x} = E_{0y}$. Two circularly polarized waves with phases $\varphi = -\frac{\pi}{2}$ and $\varphi = \frac{\pi}{2}$ respectively will in turn overlap to become a linearly polarized wave.

Except for cyclotron radiation that produces circular polarization (difficult to measure and not an object of study in this work), emission mechanisms in the hard X-ray and soft gamma-ray spectrum are dominated by linear polarization [3]. For this reason this will be the only state of polarization considered.

2.1.3-Degree and Angle of Polarization

Measurements of the degree and angle of polarization added to spectral and time variability analysis will double the number of observational parameters we can analyze in astrophysical sources. To understand these two parameters let us consider the orientation of the electric vector in the polarization plane in the figure below.

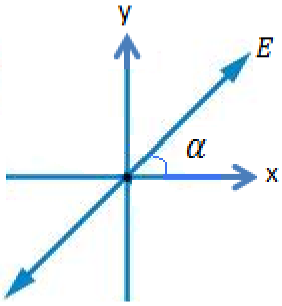

Figure 2.2 – Electric field's orientation in the polarization plane.

Let **E** be the electric field vector of an electromagnetic wave and α the angle it makes with the x axis it is easy to see that it in practice any wave whose electric field is not aligned with one of the axis can be thought of as two independent waves perpendicular to each other along the x and y axis and with magnitudes $Ecos(\alpha)$ and $Esin(\alpha)$ respectively.

Now let us consider a beam of photons. If this beam is unpolarized the probability that we find a wave with a specific value for α is the same independently of the value chosen. Another characteristic of this beam is that if we decompose all its waves in their x and y components the total magnitude along both axis will be the same. If the all the waves have the same orientation however (α is the same for each one of them), we say that the beam is a 100% polarized. This will lead to an asymmetry in the total magnitudes except for angles that are odd integer multiples of π/4 since in this case the magnitude in both directions is the same. One way to easily visualize this concept is by giving α a null value which makes the total magnitude along the y axis equal to zero.

Overlapping both cases will lead to a beam that is only partially polarized. Given the same intensity for both the unpolarized and the polarized beam the resulting beam will be 50% polarized. Establishing I_{unpol} and I_{pol} as the intensity of the unpolarized and polarized beam respectively it is easy to see the resulting beam will become more or less polarized depending on which intensity is greater. The degree of polarization Π (careful to not confuse it with the number π), is then defined as the ratio between the intensity of the polarized beam and the total beam intensity:

$$\Pi = \frac{I_{pol}}{I_{unpol}+I_{pol}} \tag{2.6}$$

From this equation we can easily calculate the cases mentioned before. An unpolarized beam will have $I_{pol} = 0$ and 0% degree of polarization. In the other end of the spectrum $I_{unpol} = 0$ will result in $\Pi = 1$ or a degree of polarization of 100%. If both intensities are equal then a 50% polarized beam is obtained.

Another way to calculate the degree of polarization comes from the cross-section of the wave having polarization to parallel $d\sigma_{\parallel}$ and perpendicular $d\sigma_{\perp}$ to the emission plane:

$$\Pi = \frac{d\sigma_{\perp} - d\sigma_{\parallel}}{d\sigma_{\perp} + d\sigma_{\parallel}} \tag{2.7}$$

Finally it becomes obvious that the angle of polarization will be the one that the polarization vector of the polarized beam makes with the x axis. Remember that this discussion is valid only for linear polarization.

In chapter 4 measurement techniques for these parameters will be discussed.

2.2 – Emission Mechanisms

There are several mechanisms that produce polarized gamma radiation. These mechanisms are mainly non-thermal, the exception being thermal Bremsstrahlung emission, and are often associated with strong magnetic fields found in the most extreme objects in the universe. The mechanisms can be further categorized by those originated in the acceleration of charged particles (Bremsstrahlung and Magnetic Bremsstrahlung emission) and those emerging from previous gamma rays such as Compton Scattering and Magnetic Photon Splitting. The radiation emergent from either of these mechanisms is linearly polarized and can give insight not only to the physics that occurs in astrophysical sources but also to the geometry of such objects [3].

2.2.1-Thermal Bremsstrahlung

An accelerated charged particle will lose energy by emission of photons. This process, called Bremsstrahlung radiation or free-free emission, can occur either in the electrostatic field of an ion or of an atomic nucleus. A schematics of the interaction is show in figure 2.3.

In the gamma-ray range we expect non-relativistic Bremsstrahlung to be dominant over its relativistic counterpart. The non-relativistic expression for the intensity of the radiation emitted by a single electron with kinetic energy E and velocity v has been derived by Bethe and Heitler and is as follows:

$$I(\varepsilon) = \frac{8}{3} Z^2 \alpha r_e^2 m_e c^2 v N \ln\left[\frac{1+\left(1-\frac{\varepsilon}{E}\right)^{\frac{1}{2}}}{1-\left(1-\frac{\varepsilon}{E}\right)^{\frac{1}{2}}}\right] \tag{2.8}$$

Where Z is the atomic number of the nucleus, α the fine structure constant, r_e the classical electron radius, N the number density of the nuclei and ε the energy of the emergent photon. An interesting result arises when $\varepsilon = E$. In this case the term inside the logarithm is equal to one and the intensity goes to zero. It is obvious at this point that there is a cut-off frequency when the photon energy reaches the value of the electron energy as the latter cannot lose any more energy. In the opposite side of spectra, when $\varepsilon \ll E$, this term becomes $4\frac{E}{\varepsilon}$. The variation will thus be slow and the spectrum will resemble a constant one [4].

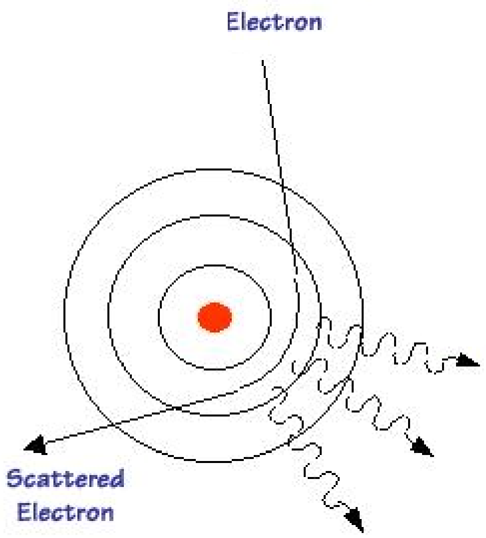

Figure 2.3: Radiation emission by the acceleration of an electron in the electrostatic field of a nucleus (http://www.physics.isu.edu/health-physics/tso/rad_training/ussalpha.html).

In the astrophysical paradigm Bremsstrahlung radiation has origin in hot plasmas at temperatures above 10^6 K [5]. A Maxwell distribution for the electrons velocity is therefore expected. Integrating 2.7 over this distribution, and considering that the medium where the process occurs is optically thin to this emission, we find that the power radiated is weakly dependent on the frequency of the radiation and can be expressed as:

$$P(\varepsilon)d\varepsilon \propto k \tag{2.9}$$

Where k is a constant. *The value of* k determines the shape of the power spectrum. In this case the intensity will be independent from the energy and will follow a straight line across the spectrum.

The degree of linear polarization of the emitted photon is given by [5]:

$$\Pi = \frac{(E_e - pccos\theta)m_e c^2 \varepsilon - 2{m_e}^3 c^6}{(E_e - pcos\theta)(E^2 - m_e c^2 \varepsilon) + 2{m_e}^3 c^6} \tag{2.10}$$

Here E_e stands for the total energy of the incident electron, p for the momentum of the electron and θ is the emission angle with respect to the incident particle's direction. In figure 2.4 we can see the degree of polarization for incident electrons with energies 5.11 MeV for several emission angles. The high degree of polarization observed for small angles along with its negative value suggest that the polarization of the emitted photons tends to be parallel to the velocity of the electron and their direction tends to be normal to the electron's path [3]. It is also possible to see that high energy photons will have a higher degree of polarization, up to almost 100% for a very small emission angle.

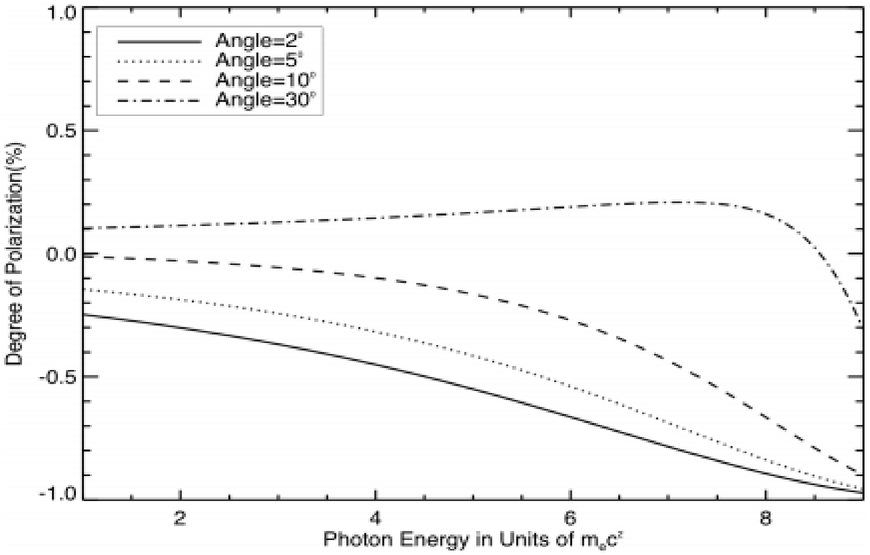

Figure 2.4: Degree of linear polarization given an electron of energy $10m_ec^2$.

2.2.2-Magnetic Bremsstrahlung

Magnetic Bremsstrahlung is another mechanism that generates Bremsstrahlung radiation. In this case however, the acceleration of the charged particle is due to the presence of a constant magnetic field **B** instead of a static electric field. Before continuing let me just leave a note that most of this section is inspired in [3] since the treatment made in it is what is sought. The force experienced by the particle is proportional to its charge q and is perpendicular to the plane defined by the magnetic field and to the particle's velocity:

$$\boldsymbol{F} = \frac{q}{c}(\boldsymbol{v} \times \boldsymbol{B}) \tag{2.11}$$

Where c is the velocity of light. The particle will then describe a circular path around the magnetic field line. If $\boldsymbol{v}$ and **B** are not at a right angle the particle's velocity will also have a component along the magnetic direction and the motion will become helical. An important property of this movement is its frequency v_r also called gyrofrequency which can be found with the following expression:

$$v_r = \frac{qB}{2\pi\gamma mc} \tag{2.12}$$

Where m and γ are the mass and the Lorentz factor of the particle respectively. This result can be used to obtain the emission rate of radiation:

$$-\frac{dE}{dt} = \frac{\sigma_T}{4\pi}\left(\frac{v}{c}\right)^2 c\gamma^2 B^2 \sin^2\theta \tag{2.13}$$

Where σ_T is the Thompson cross-section, θ is the angle the velocity makes with the magnetic field and v is the velocity of the charged particle. There are two important cases that must be discussed, cyclotron and synchrotron radiation corresponding to the non-relativistic and the relativistic limits of the process respectively. Another case we must discuss is the curvature radiation which occurs in the relativistic limit but with a curved magnetic field.

2.2.2.1-Cyclotron emission

In the non-relativistic, i.e., when v<<c, equations 2.12 and 2.13 become:

$$v_r = \frac{qB}{2\pi mc} \tag{2.14}$$

$$-\frac{dE}{dt} = \frac{\sigma_T}{4\pi}\left(\frac{v}{c}\right)^2 cB^2 \sin^2\theta \tag{2.15}$$

In the figure below it is easy to see that the emission will have dipolar form in the plane defined by the velocity and acceleration of the particle.

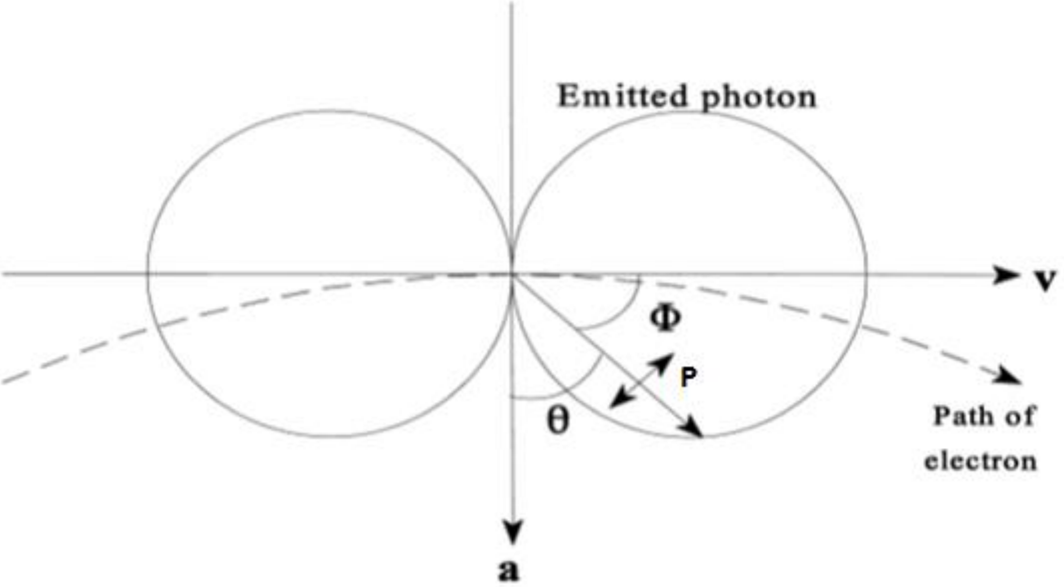

Figure 2.5: Polar diagram for dipolar emission from cyclotron radiation [3]. Here **P** is the polarization vector of the emitted photon.

The intensity of the emission is proportional to $\sin^2\theta$ hence the zero value in the direction parallel to $\boldsymbol{a} = \frac{\boldsymbol{F}}{m}$ and the maximum one in the direction perpendicular to it. The polarization vector can be found in the plane formed by **a** and **v.**

In the case of astrophysical sources, since we are in the optical infinity, a magnetic field is perpendicular to the line of sight will result in the acceleration vector perform a simple harmonic motion which will cause the polarization to be linear. In any other case the acceleration will be seen rotating which will lead to elliptically polarized radiation which becomes circularly polarized when the magnetic field reaches a parallel direction in regards to us, the observer.

This being the case we conclude that the polarization of radiation by this mechanism will not be addressed in a polarimeter of this kind since only in very specific cases where the magnetic field is perpendicular to our line of sight will the polarization be linear. Another point limiting the performance of our devices measuring the polarization of this radiation is the energy limitation that cyclotron emission has. In fact, knowing that astrophysically speaking electrons are the most important particle accelerated in magnetic fields due to its low mass, and that the stronger magnetic fields found in astrophysical sources have 10^9T, we see, substituting in 2.14, that the energy excepted is below 100 keV, a region not addressed in this work.

2.2.2.2-Synchrotron emission

In the relativistic side of this mechanism we have synchrotron radiation, the relativistic solution for an accelerated charged particle in a magnetic field. In this case the gyrofrequency expression will not lose the Lorentz factor turning out to be dependent on the energy of the electron, therefore requiring a different treatment that takes into account the energy distribution of the electrons. The gyrofrequency in the observer frame can be obtained from 2.12:

$$\nu_r = \frac{qB}{2\pi mc}\frac{3}{2}\,\gamma^2 sin\theta \qquad (2.16)$$

Let us now look at the polar diagram of the emission shown in figure 2.6. Unlike in the rest frame of the electron where the diagram has the same shape as the cyclotron one, the observer frame the emission reveals a concentration of energy in the forward direction of the electron in detriment of the other directions. It becomes apparent then, that an observer outside this small window of radiation will scarcely see any radiation.

To study the emission of this mechanism we can start by separating the power emitted in its components parallel and perpendicular to the projection of the magnetic field direction as seen by the observer:

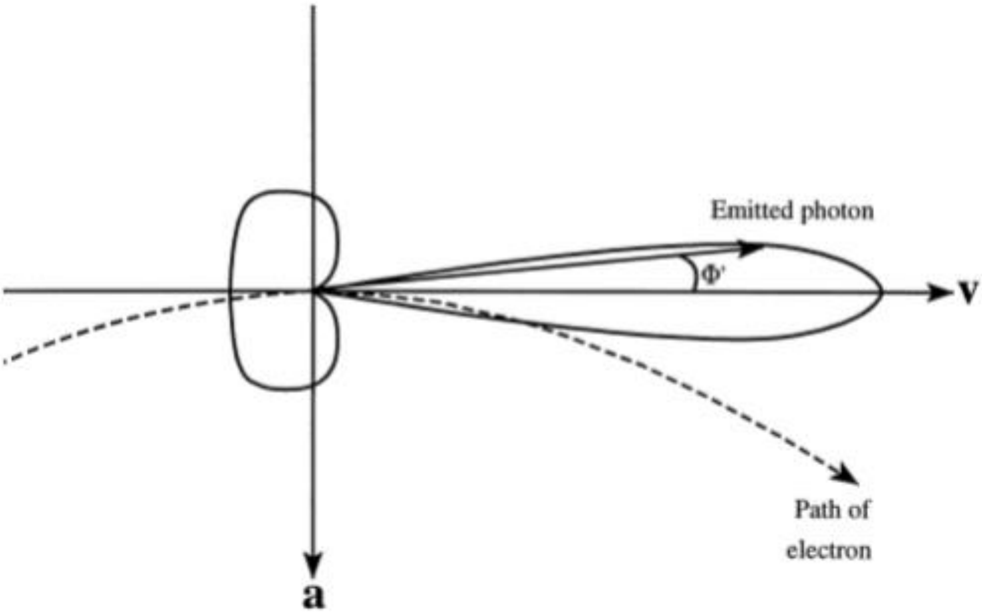

Figure 2.6: Polar diagram for dipolar emission from synchrotron radiation as seen in the observer frame [3].

$$P_{\perp}(\omega) = \frac{\sqrt{3}e^3 B sin\theta}{4\pi m_e c^2}[F(x) + G(x)] \tag{2.17}$$

$$P_{\parallel}(\omega) = \frac{\sqrt{3}e^3 B sin\theta}{4\pi m_e c^2}[F(x) - G(x)] \tag{2.18}$$

Where $F(x) = x\int_x^{\infty} K_{5/3}(z)dz$ and $G(x) = xK_{2/3}(x), K_{5/3}$ and $K_{2/3}$ are modified Bessel functions with $x = \frac{2\omega_r r}{3c\gamma^3} = \frac{\omega_r}{\omega_c}$. ω_r and ω_c are the relativistic angular gyrofrequency and the critical angular frequency respectively and $r = \frac{v}{\omega_r} sin\theta$ is the radius of curvature for the electron [3].

The total power emitted is the sum of the two components:

$$P(\omega) = \frac{\sqrt{3}e^3 B sin\theta}{2\pi m_e c^2} F(x) \tag{2.19}$$

Which gives a spectrum for a single electron with the shape of F(x) as seen in figure 2.7 and will have a broad maximum centered at $\frac{0.29}{2\pi}\omega_c$[3]

Before analyzing the polarization let us look at the energies we can expect in astrophysical sources. In the same way we did for cyclotron emission one can extract from equation 2.16 the energy of the emitted photon.

$$E(keV) = \frac{B(T)\gamma^2 sin\theta}{1.99*10^7} \tag{2.20}$$

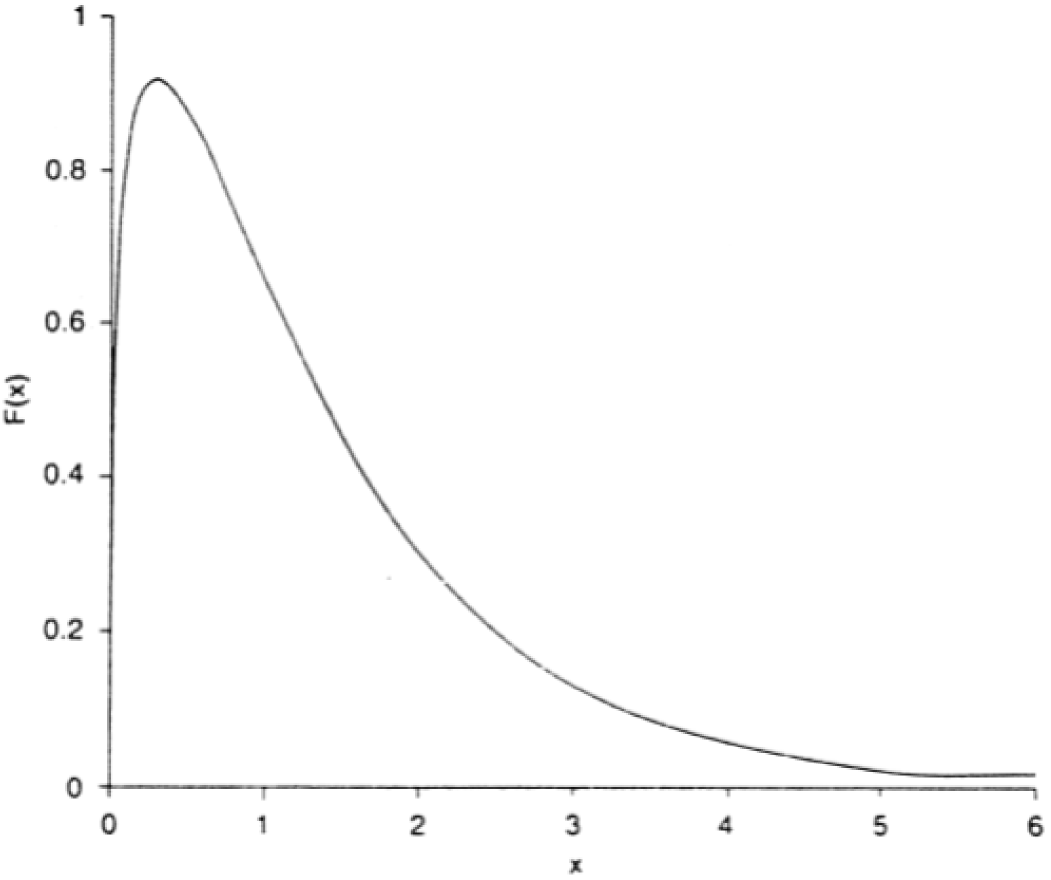

Figure 2.7: Shape of the function F(x).

Giving the same value to the magnetic field leaves us only with a dependence on the kinetic energy of the electron. A simple calculation shows that to produce a photon with 1MeV requires only a Lorentz factor of 4.46 which corresponds to an electron kinetic energy of 2.28MeV. Since in this context we have a power-law distribution for the energies of the electrons, the power emitted will have the following form:

$$P(\omega)d\omega \propto \omega^{-\frac{k-1}{2}} \tag{2.21}$$

We can then conclude that, energetically speaking, synchrotron emission is a potential mechanism for our work. In fact tests made before this in 2002, 2006 and 2008 were made in the European Synchrotron Radiation Facility (ESFR) in Grenoble used synchrotron emission as a source of polarized radiation [6] [7] [8] [9].

In terms of polarization we can substitute equations 2.17 and 2.18 in equation 2.7 in place of the corresponding cross-sections:

$$\Pi = \frac{P_{\perp}(\omega) - P_{\parallel}(\omega)}{P_{\perp}(\omega) + P_{\parallel}(\omega)} = \frac{G(x)}{F(x)} \tag{2.22}$$

Assuming a power-law distribution for the electron energies:

$$\Pi = \begin{cases} \frac{1}{2} \quad for\ x \ll 1 \\ \frac{k+1}{k+\frac{7}{3}} for\ x \gg 1 \end{cases} \tag{2.23}$$

Bearing in mind that, in the astrophysical context, the power-law indices observed vary from 1.5 to 5.0, makes us expect a maximum degree of linear polarization between 65% and 80%. Note that this result is valid only for a structured uniform magnetic field, which differs for those found in nature where the degree of polarization will be lower [9].

Elliptically polarization is also found in synchrotron radiation from a single electron when the angle between the velocity and the magnetic field is different than 90°. In such case the acceleration vector will be seen rotating through small angles inducing an elliptical component of polarization. When we add more electrons to the equation however, a distribution of pitch angles will appear and the elliptical polarization produced by electrons with opposite angles will cancel out.

Another important result appears when we consider a bent magnetic field. If the regime remains relativistic and if the radius of curvature R is small there will be synchrotron emission with frequencies:

$$v_c = \frac{3c}{4\pi R}\gamma^3 \tag{2.24}$$

This emission has γ times more power than its counterpart with a polarization orthogonal to the local magnetic vector with a similar degree of linear polarization [3].

2.2.3- Magnetic Photon Splitting

In resemblance to the electromagnetic cascade, a process known as magnetic photon splitting, where a photon splits itself into two photons, is expected to emerge in the presence of very strong magnetic fields (a fraction of $10^9 T$). This process should have inverse polarization of about 20% to 30% [3]. Since the conditions that are required to make this mechanism possible are far from those that we can create in laboratory [11], a space polarimeter would represent a great opportunity to study the physics behind the process.

2.2.4-Compton Scattering

Compton scattering is the mechanism by which a photon is scattered incoherently by an electron. The said electron is often weakly bound to a nucleus and can be treated as it was free since the photon's energy should be large in comparison with the latter's bound energy. There is another instance for this interaction called inverse Compton scattering where a relativistic electron scatters a low energy photon up to high energies. Mind that in this case of the relativistic electron we can always transform the interaction to the electron's frame of reference hence it is only necessary to discuss the first one and make the transformation later. Let us now look at a schematics of the interaction [3].

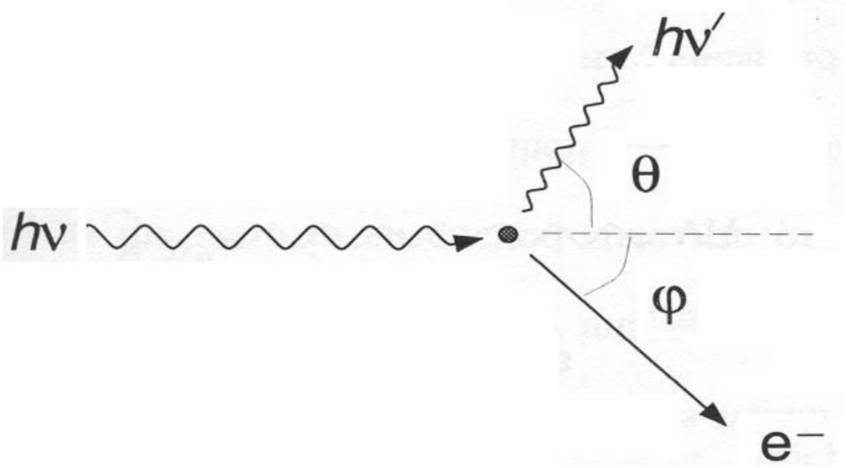

Figure 2.8: Schematics of Compton Scattering.

As shown in the figure above a photon of initial energy $h\nu$, where h is the Planck constant and ν the frequency of the photon, scatters off an electron with a polar angle θ and an energy $h'\nu'$. The energy of the latter relates to that of the incident photon according to:

$$E' = \frac{E}{1+\frac{E}{m_e c^2}(1-\cos\theta)} \tag{2.25}$$

Where E is the energy of the incident photon and E' is its energy after the interaction. Here it is possible to see that the energy of the emergent photon decreases with the scattering angle. Regarding the differential cross-sections of the scattering, named after the authors that calculated them, Klein-Nishima, two different solutions must be considered, one for an unpolarised beam, subscript U from now on, and another for a 100% polarized one, subscript P. Any case between the two can simple be treated as a superposition of them [3].

- For the unpolarised case the Klein-Nishima differential cross-section is as follows:

$$\frac{d\sigma_{KN,U}}{d\Omega} = \frac{1}{2} r_0^2 \varepsilon^2 [\varepsilon + \varepsilon^{-1} - \sin^2\theta] \tag{2.26}$$

Where r_0 is the classical electron radius and ε the ratio between the final and the initial energies of the photon. As for the polarization, it can be found by substituting 2.26 in 2.7 which leads to:

$$\Pi_U = \frac{\sin^2\theta}{\varepsilon + \varepsilon^{-1} - \sin^2\theta} \tag{2.27}$$

These equations give very important information about Compton scattering. In the first case we observe that the cross-section is only a function of the polar scattering angle and of the incident energy of the photon. The second gives the degree of polarization of a beam that goes through Compton scattering. The maximum polarization that can be obtained is $\sim 69\%$ for a scattering occurring at $\theta \sim 82^{\circ}$.

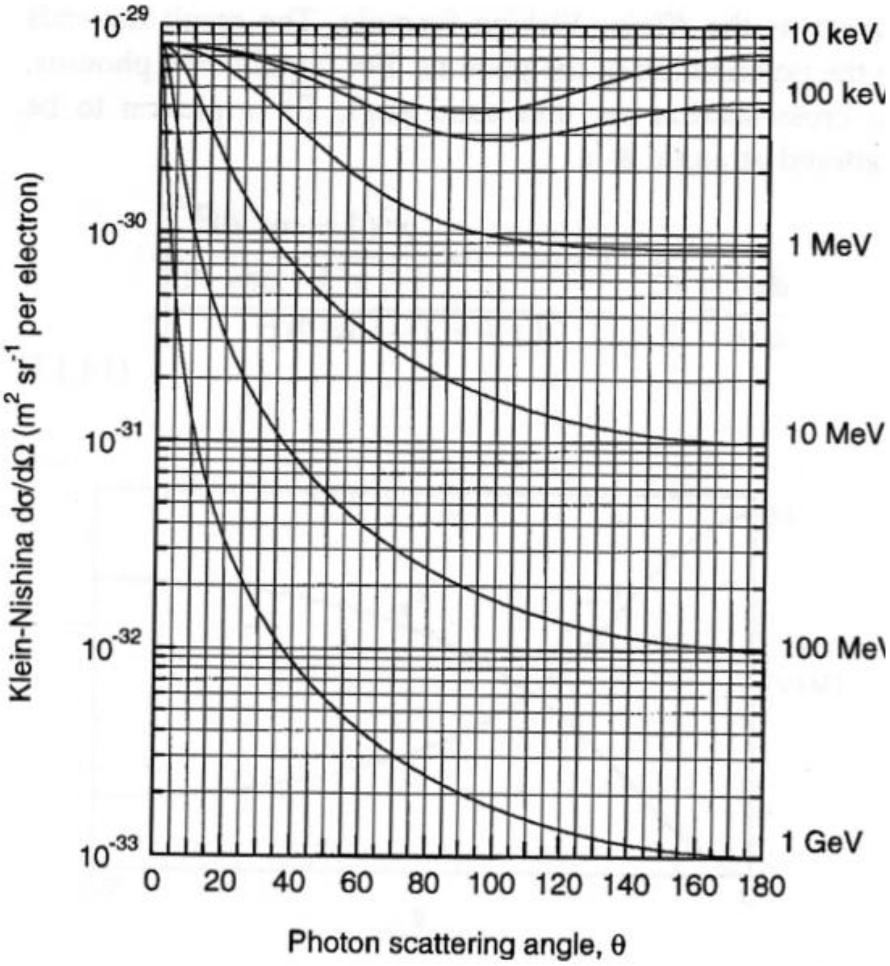

Figure 2.9: Differential cross-section in function of the scattering angle in logarithmic scale for the unpolarized Compton scattering. From E.B. Podgorsak, Radiation Physics for Medical Physicists.

The figure above displays the cross-section as a function of θ for several energies. For energies above one MeV one can see that this cross section decreases with increased scattering angle. Below this energy range however we can see that there is a minimum around 90°. Regarding the polarization of the emerging beam figure 2.10 is very clear. For higher energies polarization will be residual while for lower ones we can expect a high degree of polarization. This degree will have a maximum near 90°. Since one of the premises of studying polarization measurement is to have a beam with a high degree of polarization and since the only source available to this work, ^{22}Na, is unpolarised it is easy to predict that a problem shall arise between having a high degree of polarization or a high intensity beam. The solution to this problem will be discussed in chapter 5 when I will talk about the experimental setup for this work.

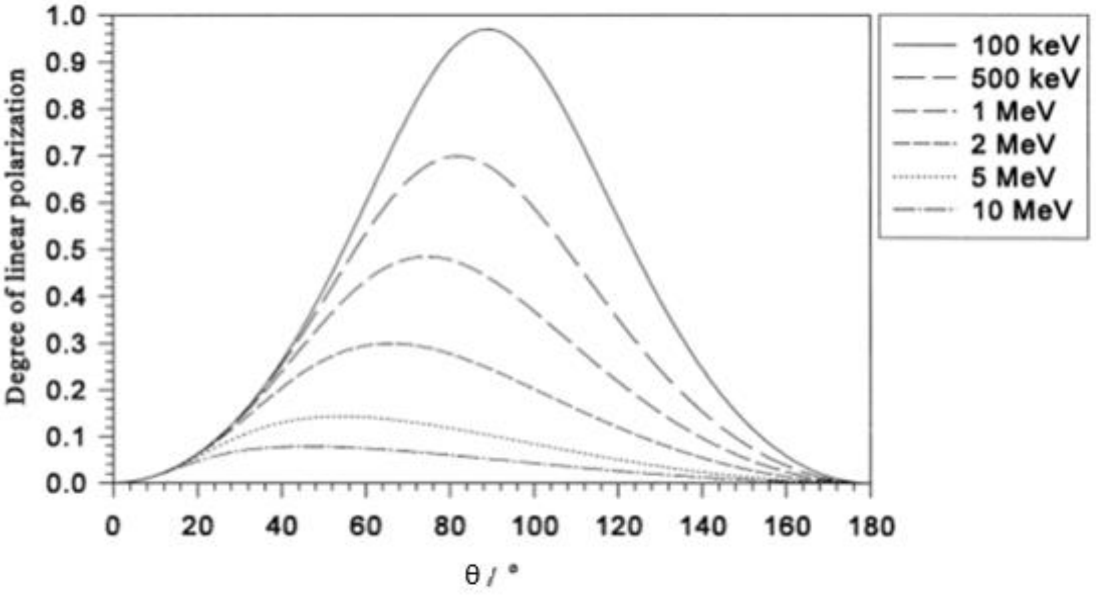

Figure 2.10: Degree of polarization with respect to the scattering angle in Compton Scattering for several energies [3].

In the case of a polarized beam different parameters should be considered leading to different equations for the differential cross-section and the polarization of the outgoing beam. In the first case we obtain:

$$\frac{d\sigma_{KN,P}}{d\Omega} = \frac{1}{2} r_0^2 \varepsilon^2 [\varepsilon + \varepsilon^{-1} - 2\sin^2\theta\cos^2\eta] \tag{2.28}$$

This equation shows a dependency in the azimuthal angle in contrast with the unpolarized one. Because of this, photons from a polarized beam, Compton scattered by an angle θ, will have an asymmetric azimuthal distribution as showed in figure 2.11. Figure 2.11a shows the distribution for a 100% polarized beams with different energies when $\theta = 90°$. In this case one can see that the asymmetry diminishes for higher energies until a point when none is found. The figure to the left shows distributions for photon energies of 200 keV but with different polar angles. As it can be seen the asymmetry will be more prominent as θ approaches the 90° mark and will disappear at $\theta = 0°$.

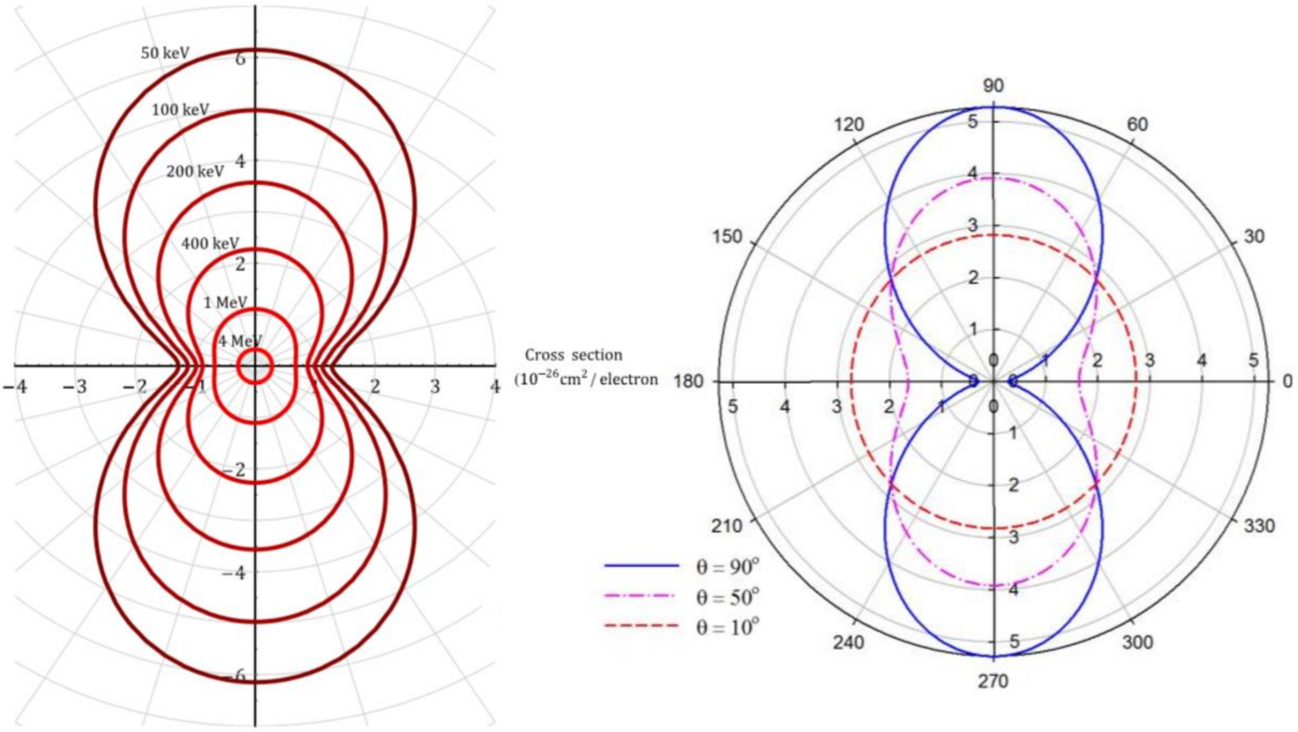

Figure 2.11 a) and b): Azimuthal distribution of 100% polarized beam of photons emerging from Compton scattering. In the left side, the polar angle θ is kept constant at 90° [13]. In the right one it is the energy that is kept constant at 200 keV while θ varies [10].

Regarding the degree of polarization of the emergent beam the dependency on the energy and angles is as follows:

$$\Pi_P = 2\,\frac{1-2\sin^2\theta\cos^2\eta}{\varepsilon+\varepsilon^{-1}-2\sin^2\theta\cos^2\eta} \qquad (2.29)$$

This equation also brings an important result, a polarized beam going through Compton scattering will have its polarization decreased.

Since Compton scattering is the process by which we polarize our beam it is also of importance that we calculate the polarization angle expected. The formula to calculate it was first obtained by (Angel, 1969) [3]:

$$\boldsymbol{P} = \frac{1}{|\boldsymbol{P}|}(\boldsymbol{P_0}\times\boldsymbol{D})\times\boldsymbol{D} \qquad (2.30)$$

Where P is the polarization vector of the polarized fraction of the scattered beam, $\boldsymbol{P_0}$ the polarization vector of the initial beam and D is the scattering direction.

Compton scattering occurs naturally in astrophysical sources, without the need for specific conditions like synchrotron radiation. The fact that its emission spectrum has the same shape as the synchrotron one [3] makes polarization measurements very important since it can distinguish between the two of them. Its asymmetry in the azimuthal distribution for polarized beams is also of importance since it is the basis of the polarimetric techniques used.

2.3 – Scientific Interest on Gamma-Ray Astronomy

The gamma-ray sky is rich in astronomical sources. From the late stages of massive stars that give birth to supernovas, neutrons stars and black holes, the sun and even our planet, there are a lot of objects that would benefit from observational instruments with increased sensitivity and polarimetric performance than those launched so far [16].

Polarization of gamma-ray sources is still fairly unexplored since no dedicated polarimeter has ever been launched. Nonetheless measurements with non-dedicated instruments like SPI have already been done giving insight to the polarization of gamma-rays in the Crab nebula [1] [18]. Future instruments with better sensitivity and polarimetric performance are then invaluable in further studying gamma-ray sources.

In this section I will talk about the different objects that emit gamma-rays either polarized or unpolarized.

2.3.1-Supernovas

The late stages of massive stars are catastrophic. These are ruled by extreme physical conditions which make spectacular phenomena possible. The evolutionary stages that these stars go through depend on their initial mass but always culminates in a supernova (SN).

Supernovas are explosions of stars that can outshine an entire galaxy. There are 2 main divisions for supernovas that are due to the existence (type II) or non-existence (type I) of hydrogen lines. Type I supernovas can be further divided by the presence of a strong Si II line at 615nm (type Ia) or of a strong helium line (type Ib). If none is present the supernova is considered of type Ic [14]. These considerations correspond to the spectra at maximum light output. A classification scheme can be found in the figure below:

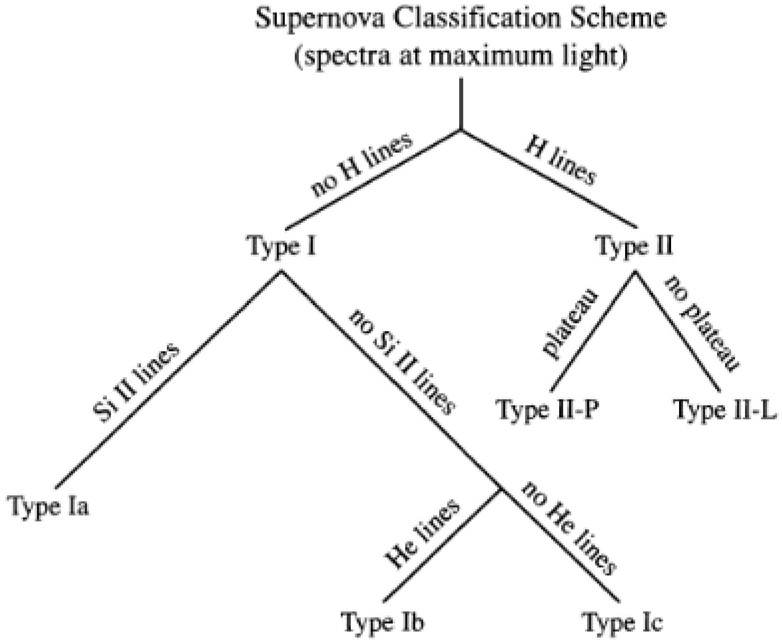

Figure 2.12: Supernova classification scheme [23].

At the moment of this writing it, astrophysicicts believed that supernovas could be originated by two means:

The first one derives from the accumulation of material by a white dwarf from a stellar companion and corresponds to a type Ia supernova. If the mass of the white dwarf reaches values near the Chandrasekhar limit a supernova will occur leaving no remnant behind [15]. The amount and distribution of radioactive isotopes produced in these supernovas strongly depend on the stellar configuration at the onset of the explosion, on the ignition process and on its propagation [16]. Since the most abundant products of the explosion are ^{56}Ni and the isotopes that its' chain gives birth to, the resulting lines will lay in the gamma spectrum, making it essential to develop better instruments to measure these lines and further advance our knowledge of this events.

The second case corresponds to supernovas that have their origin in the core collapse of a massive star. In this case the mass of the star must be high enough (over 8 solar masses) so that the core can achieve a temperature where not only carbon burning is possible but also the burning of its products all the way to the formation of iron is possible. Since the binding energy is at a maximum value for iron, further reactions would be endothermic therefore the burning will stop at this element. At the high temperatures that the core of the star has at this point photodisintegration will begin to appear. This process is especially important in iron and helium nuclei since the photodisintegration of iron produces 14 atoms of helium that in turn disintegrates into two protons and two neutrons. The protons will now assist the heavy nuclei in capturing the electrons that supported the core through degeneracy pressure producing neutrons and neutrinos. The latter will carry enormous amounts of energy away from the nuclei. At this stage the core will start to collapse until neutron degeneracy catches up with gravity. This will cause matter in the core to rebound which creates an outward wave that will collide with the infalling material. The rise in temperature will give rise to photodisintegration that should rob energy from the shock creating a stall. Since below the shock, matter is now so dense that not even neutrinos can escape easily, more energy will be deposited by these particles pulling the shock outward expelling the infalling matter resulting in a supernova [14].

Jets and/or dynamical mixing of core material can enhance the lines from ^{56}Co and ^{57}Co providing insight to the mechanisms at hand. Also, large quantities of the first isotope would show that pair instability supernovae can occur in the recent universe. Finally, pre-supernova mass-loss should emit a hard x–ray continuum as well [16]. This treatment includes the last 3 types of supernovas mentioned; type Ib, Ic and II. In the first two the hydrogen envelope must have been lost prior to the detonation.

Supernovas are not the final stage of these stars, for stars with initial masses inferior to 25 times the solar mass a neutron star supported by neutron degeneracy pressure will arise while stars with initial masses superior to this value will become black holes. The decay of ^{44}Ti produced in supernovas has an extended lifetime of ~85 year emitting 3 lines in the gamma domain at 67.9, 78.4 and 1157 keV. The detection of these lines could help find previously unknown young supernova remnants. Better sensitivity and a wide field of view should be able to further investigate the nature of these amazing explosions [16].

2.3.2-Black Holes and Neutron Stars

Supernova Remnants (SNR) are some of the most exciting objects in the universe. They are what is left of the initial object after going Supernova. These remnants, whose unique conditions allow the occurrence of amazing phenomena that only now has been within our reach, include both black holes and neutron stars, compact objects subject to intense gravity. This objects can be found isolated or in binary systems.

2.3.2.1-Gamma-Ray Bursts

Gamma-Ray Bursts (from now on GRBs) result from the collapse of a massive star or the merge of compact stars. They are the most explosive events in the universe since the Big Bang. In fact, despite their emission time being very low, from some seconds to a hundred seconds, they emit more radiation in that time than the sun will in its entire lifetime. Their emission has an energy content of $\sim 10^{53} ergs$ which corresponds to a luminosity a million times larger than the peak luminosity of a supernova, despite their cosmological origins [19].

They can be decomposed in two stages, a prompt emission, related to the acceleration of charged particles in a jet, that occurs in the first few seconds of the event with peak luminosity in the hundred keV range, and an afterglow emission that involves the collision of the said jet with the interstellar medium that lasts up to a few months shifting the peak to lower frequencies across the spectrum [20]. Since in the afterglow gamma-ray emission is non-existent or negligible the focus will be on the prompt emission. These bursts can be divided in two classes, long and short, depending on their prompt emission duration being over or under one second respectively.

Since the prompt emission peaks in the hundred keV energy range, one can assume that the mechanisms discussed before in this chapter are at work. It so happens that the most popular model for this stage, the internal shocks model, explains the energy lost via synchrotron emission and Compton scattering. A power-like spectrum observation sustains this model despite the problems it has explaining the observed energies below the peak [19]. As it was seen in the previous section, both mechanisms produce the same power-law spectrum but differ in the polarization properties of their emission. Polarization measurements are then essential to understand the process.

A proposal made by Saviv and Dar (1995) indicates inverse Compton scattering from highly relativistic electrons as the source of the gamma emission in GRB. Taken this into account a partially polarized beam should arise with polarization angle perpendicular to the jet axis. A dependence of the degree of polarization with the burst duration has been found. This dependence is not without some dispersion while different redshifts should also introduce variability in the observed polarization [3].

In figure 2.13 one can see the average polarization in long GRBs as a function of their duration. The maximum polarization occurs for GRBs with 5s duration. The degree of polarization is very high in these cases going down to zero for both short and very long bursts. A point also worth taking is that the maximum for the burst rate is not coincident with the one of polarization and is also wider hence we should expect large amounts of GRBs with both high and low degree of polarization.

Some measurements of GRBs has already been made with data from COMPTEL and IBIS despite both these instrument not being dedicated polarimeters [3] [21]. Some of these values can be found in table 2.1 below and show high degrees of polarization.

GRB	Duration (s)	Lower Limit (%)	Highest Limit (%)
061122 [19]	8	33	90
100826A [20]	100	16	38
110301A [20]	10	30	-

Table 2.1: Duration and polarization limits of some GRBs.

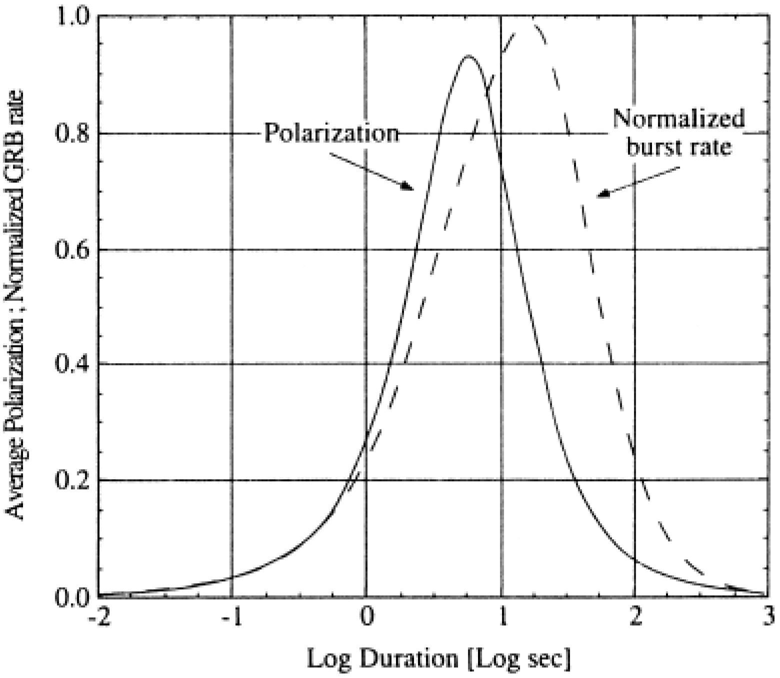

Figure 2.13: Average polarization of long GRBs as a function of their duration (Shaviv and Dar, 1995).

GRBs are a hot topic and some advance in this subject can be expect with the development and launch of a new generation of gamma detectors with better sensitivity, polarimetric capabilities and a wide field of vision.

2.3.2.2-Pulsars

Pulsars are rapidly rotating neutron stars with a very well determined small period T ranging from 1.5ms to 5s and a very intense magnetic field whose axis is at an angle with the rotation axis. This period grows in time as the star slows down but at an extremely slow rate $\dot{T} \approx 10^{-15}$ [3] and [23]. The number of known gamma-ray pulsars is approaching the 150 mark, a great advance if we consider that in the 1997 only 7 had been observed. The number of classes has been increasing as well as half of these are radio quiet while millisecond pulsars are starting to become a big group [24].

The combination of rapid rotation and intense magnetic field makes pulsars very good particle accelerators and as a consequence gamma emitters. There are two models that try to explain emission in these objects, the polar cap model and the outer gap model. In the polar cap model, particles are accelerated by rotation-induced electric fields above the polar cap and move along the dipole magnetic field lines producing curvature radiation. High energy photons will produce positron/electron pairs that will then lose energy via synchrotron radiation [24]. The outer gap model was introduced to try to take into account some features the polar cap could not explain such as the Vela pulsar light curves. In this model particles are accelerated within the vacuum outer gap that extends from the null surface, which separates opposing charges, to a light cylinder, where co-rotation stops, and produce the observed radiation by synchrotron and curvature radiation far from the neutron star [24].

The emission mechanisms in both models are the same hence a similar emission spectrum should been seen. Due to the emission occurring in different locations and geometries different polarization properties are expected making polarimetry a good candidate to help resolve this 47 year old problem.

2.3.2.3 – Binary systems

Compact objects can also form binary systems with others stars (x-ray binaries), massive stars (gamma-ray binaries) or other compact objects. The first two types are usually associated with neutron stars although a black hole can also be found [14].

From x-ray binaries three lines are expected to appear. The first should be a narrow 511 keV line, result of the annihilation of positrons when a jet, misaligned with the binary orbital plane, hits the atmosphere of the companion star. The other two should have 2.2 MeV occurring from the neutron capture by hydrogen atoms. This can occur in the atmosphere of either star which will differentiate the two since the strong gravitational field from the neutron star should redshift the line. Good resolution measurements from this lines should give insight to the nature of the jets in the case of the 511 line and to the mass to radius ration of the neutron star [16].

If instead the companion star is massive the observed emission will range from radio up to TeV energies but with most of their radiation being emitted in the 1-1000 MeV band. Since only five of such systems were discovered so far, not much is known about them, making MeV surveys the best chance to find more of these objects and enhance our knowledge [16].

Last MeV emission has been found in Cyg X-1, a black hole binary. This type of systems are expected to produce both synchrotron and Compton scattering making it crucial to make polarimetric measurements in order to distinguish between both mechanisms and to study the nature of the jet. Sensitivity and angular resolution also play a role here allowing to differentiate contributions from the accretion of matter and from jets [16].

2.3.3-The Sun and the Earth

Gamma-ray astronomy can also be a powerful tool to study our corner of the universe. Gamma emission has been detected in our solar system predominantly from solar flares but can also be found in the Earth possibly associated with thunderstorms.

2.3.3.1-Solar Flares

Solar Flares because of their closeness to Earth are one of the most important phenomenons to be studied. These consist of a sudden brightening of the sun occasional mass ejection. They are associated with sunspots occurring in the vicinity of complex groups of them. Their emission can be found across the spectrum all the way up to hard x-rays and even gamma energies. They can radio blackouts across the world hence their importance [25] [26].

Several models exist to describe these events. There are however some features that can be generalized. Solar flares are short lived, lasting from 20 minutes to 3 hours, coming across 20000 to 40000 km and emitting a total of 10^{23} to 10^{24} J [3].

Most theories have the magnetic field being torn and reconnected causing charged particles to be accelerated into high energies at the top of the coronal loop. The gamma emission should result from this acceleration consisting in line radiation from nuclei excited by collisions with the accelerated particles, electron bremsstrahlung and even pion decay. Line radiation is not expected to be polarized but both the other two processes are. Predictions show a polarization up to 25% for the whole loop at 102 keV [3].

2.3.3.2-Terrestrial Gamma-ray Flashes (TGFs)

TGFs were discovered by the Compton Gamma-Ray Observatory. Its high energy emission, up to 100 MeV, was a surprise due to their planetary origin. FERMI has already showed that these events are very short (50-500 μs) and usually so intense that they affect the detector's deadtime and cause pile-up. They are still a very misunderstood phenomena that could enlight our knowledge of thunderstorms and atmospheric electrodynamics in general [16].

In this chapter an acknowledgement on the topic of polarized gamma-rays has been made, with a focus on the production mechanisms and the main astrophysical objects that emit them. The latter is a vast subject that can be further explored if one considers dark matter emission or decay, cosmic rays and others that were not mentioned. It was acknowledged that sensitivity improvements on instruments coupled with polarimetric capabilities are essential to distinguish models and to understand what production mechanisms are at work in a big variety of astrophysical objects.

References

[1] V.C.A. Ferraro, “Electro-Magnetic Theory”, Watson Press (15 Nov 2010)

[2] http://www.coladaweb.com/fisica/ondas/ondas-eletromagneticas

[3] F. Lei, A. J. Dean, and G. L. Hills, “Compton Polarimetry in Gamma-Ray Astronomy”, *Space Science Review*, Vol. 82, p. 309, (1997)

[4]http://asd.gsfc.nasa.gov/Volker.Beckmann/school/download/Longair_Radiation1.pdf

[5]: Gluckstern & Hull, “Polarization Dependence of the Integrated Bremsstrahlung Cross Section”**,** Phys. Rev. 90, 1030 – Published 15 June 1953

[6] Curado da Silva et all, “Polarization degree and direction angle effects on a CdZnTe focal plane performance”, IEEETRANSACTIONSONNUCLEARSCIENCE,VOL.59,NO.4,AUGUST2012

[7] G. Ventura, E. Caroli, N. Auricchio, A. Donati, G. Landini, F. Schiavone, R. M. Curado da Silva, POLCA: experimental set-up, calibration procedures and results, Internal Report IASF/BO n. 352/2002 (September 2002)

[8] G. Ventura, E. Caroli, N. Auricchio, A. Donati, G. Landini, F. Schiavone, R. M. Curado da Silva, POLCA2 (POLarimetry with CZT Arrays): experimental set-up, calibration procedures and results, CZT-IASF-BO-004.

[9] “Examining Celestial Polarization with the Gamma-Ray Polarimeter Experiment (GRAPE) – Dissertation by Taylor Pyne Connor

[10] E. Caroli, A. Donati, G. Landini, F. Shiavone, J. B. Stephen, G. Ventura, R. M. Curado da Silva, S. Sordo, N. Auricchio, A. Pisa, V. Honkimaki, LAPOLCA: USER MANUAL FOR ESRF 2008 TESTS, CZT-IASF-BO-007

[11] Boyko et al, Pulsed Power Conference, 1999. Digest of Technical Papers. 12th IEEE International (Volume:2)

[12] M. Chauvin, J.P. Roques, D.J. Clark and E. Jourdain, POLARIMETRY IN THE HARD X-RAY DOMAIN WITH INTEGRAL SPI, The Astrophysical Journal, 769:137 (8pp), 2013 June 1

[13] S. Antier et al, Hard X-ray polarimetry with Caliste, a high performance CdTe based imaging spectrometer

[14] An introduction to Modern Astrophysics 2nd Ed., B. Carrol, D. Ostlie (Pearson 2007)

[15] Paolo A. Mazzali,, Friedrich K. Ropke, Stefano Benetti and Wolfgang Hillebrandt, “A Common Explosion Mechanism for Type Ia Supernovae”,

[16] SEMINAIRE DE PROSPECTIVE SCIENTIFIQUE 2014, APPEL A IDEES. CNES

[17] Dean, A. J., Clark, D. J., Stephen, J. B., et al. 2008, Sci, 321, 1183

[18] Forot, M., Laurent, P., Grenier, I. A., Gouiff`es, C., & Lebrun, F. 2008, ApJL, 688, L29

[19] N. Gehrels and S. Razzaque, Invited review article in the special issue of Frontiers of Physics on High Energy Astrophysics, eds. B. Zhang and P. Meszaros, arXiv:1301.0840 [astro-ph.HE].

[20] P. Meszaros, Gamma-Ray Bursts, Rept.Prog.Phys.69:2259-2322 (2006)

[21] D. Gotz, S. Covino, A. Fernandez-Soto, P. Laurent, and Z . Bosnjak. The polarized Gamma-Ray Burst GRB 061122. 2013, 1303.4186.

[22] Yonetoku et al, Magnetic Structures in Gamma-Ray Bursts Jets Probed by Gamma-Ray Polarization, The Astrophysical Journal Letters, Volume 758, Issue 1, article id. L1, 5 pp. (2012).

[23] An Introduction to Modern Astrophysics 2nd Ed – B. Carrol, D. Ostlie (Pearson, 2007)

[24] Patrizia A. Caraveo, Gamma-Ray Pulsar Revolution, Annual Review of Astronomy and Astrophysics, vol. 52, p.211-250

[25] M. S. Longair, “High Energy Astrophysics” Vol 1 2nd Ed, Cambridge University Press

[26] http://www.esa.int/Our_Activities/Space_Science/What_are_solar_flares

Chapter 3

Gamma Radiation Detection

In this chapter only gamma-ray detection will be pursued leaving out other types of radiation. This subject is a very extensive one as it can be seen from [1] and [2] hence a lot of details will be left unchecked. General properties of detectors will be discussed first, followed by the working principle of detectors and ending with the state of the art of polarization detectors.

3.1 – General Properties

When a detector is required one looks for a set of parameters that depend on the function at hand. Some of these parameters like sensitivity, efficiency and energy resolution are quite general while others like the polarization modulation factor and the minimum detectable polarization are more specific. First however one should define the modus operandi of detectors.

3.1.1 – Simplified Detector Model

Current detectors work under the assumption that given a quantum of radiation, a photon in this case, an interaction will occur in the detector volume. For photons we expect one of the interactions mentioned in 3.3.1 to occur. This interaction will result in the appearance of a certain amount of charge that is collected by applying an electric field to the detector, causing the negative and positive charges to move towards the cathode and the anode respectively. A current proportional to the charge can then be found due to the latter's collection.

A photon interacting in the detector will deposit a certain amount of energy in its volume. This energy is transferred to electrons that will then move through the detector medium colliding with its atoms and creating electron/ion pairs that will in turn be accelerated towards the poles of the electric field. Notice that as the energy deposited in the electron by the initial interaction increases, this electron will have more energy giving it the ability to create more pairs in its path hence increasing the collected charge and the current that proceeds it. A conversion can then be made between the output current and the interaction energy. Since the collection of the charges does not take place instantaneously, around nanoseconds for gases and picoseconds for solids [1], the current we expect from an interaction will have a general shape approximately as shown in figure 3.1.

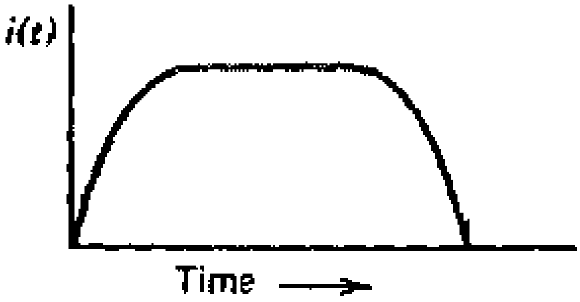

Figure 3.1: Evolution of the current with time produced by an interaction within the detector with time [1].

There are different modes to read this current that shall not be discussed. It is noteworthy to point that if a second interaction occurs within the time frame of the charge collection there will be a superposition that might be critical for signal analysis [1].

3.1.2 – Sensitivity

The first property considered is sensitivity. This is the capability a detector has to produce a useful signal for a given type of radiation and energy [2]. It can be defined as the minimum flux necessary so that a source can be detected with a certain degree of confidence. Sensitivity can depend on a number of factors such as the cross-section of an interaction in the detector, the detector mass, background and shielding of the detector. Equation 3.1 shows this dependence:

$$\phi_{s_{min}} = n_{\sigma}\sqrt{\frac{B}{\varepsilon.A.T}} \tag{3.1}$$

Here $\phi_{s_{min}}$ is the minimum flux that produces a signal-to-background ratio with at least a certain number of standard deviation n_{σ} over the background level B. The other variables are the sensitive area of the detector A, the observation time T and the efficiency ε.

3.1.3 – Efficiency

Efficiency in a detector is the property that refers to its capability to measure the radiation of an incident flux. In general (but with exceptions), for charged particles, due to their short range, most of the flux will interact within the detector volume and create a signal. Gamma radiation however can travel large distances without ever interacting. If this is the case only a fraction of the incident flux will interact in the detector. It is necessary to define two types of efficiency. Let N be the number of particles detected, N_s the number of particles emitted by the source and $N_\phi$the number of particles incident on the detector, then, according to [1], one can define the absolute ε_{abs} and the intrinsic efficiency ε_{int} as:

$$\varepsilon_{abs} = \frac{N}{N_s} \tag{3.2}$$

$$\varepsilon_{int} = \frac{N}{N_\phi} \tag{3.3}$$

Concerning the fraction of particles detected in respect to the source and to the incident flux respectively.

3.1.4 – Energy Resolution

One of the most important properties in a detector is its energy resolution. This property refers to the capability the detector has to measure the radiation energy. In the ideal case, a monochromatic flux would result in a delta function for the energy. However in practice, there are fluctuations in the number of charges a particular interaction produces. What we find instead is a Gaussian curve whose width reflects the magnitude of these fluctuations. Let the Full Width at Half Maximum (FWHM) be the width of the curve when it has half the value of the maximum as shown in figure 3.2, then we can define the resolution R as:

$$R(\%) = \frac{FWHM}{E_0} \tag{3.4}$$

Where E_0 is the energy peak's centroid. From this point one can see that to obtain better detail one must lower the FWHM term hence a better resolution points towards a lower value of R. It must be stressed that energies are considered discernable only when they are separated by more than a FWHM. This is easy explainable, looking again to figure 3.2 it can be seen that the intersection point of the two curves will have a magnitude equal to the peaks while the peaks themselves have a very small increase since they superpose with the tail of the other curve.

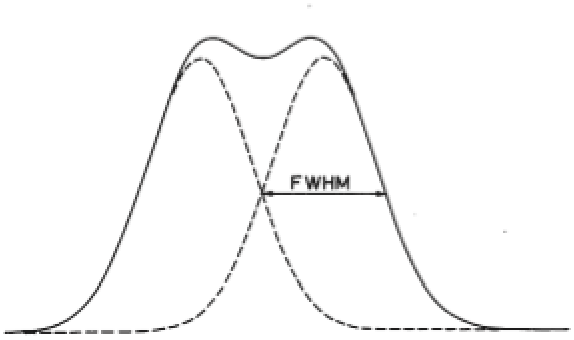

Figure 3.2: Representation of the FWHM for an energy curve and the superposition of two of such curves [1].

Another conclusion taken from equation 3.4 is that resolution is enhanced with an increase in energy. This comes from the Poisson-like statistics of ionization and excitation since a radiation that is more energetic will increase the average number of collected charges, J, hence diminishing fluctuations [1]. If the energy deposited is not a fixed value, then a Poisson distribution is in order and the resolution can be re-written as:

$$R(\%) = \frac{2.35\sqrt{J}}{J} \qquad (3.4)$$

Where 2.35 relates the standard deviation of a Gaussian to its FWHM and J is the variance. Notice that since the value of the energy fluctuates so does J. There are cases however where the incident particle depletes all of its energy. In such cases the Poisson approximation is not valid and a new factor must be considered. Statistically speaking this means that all events cause by the incident radiation are not independent [1]. A new factor must then be introduced:

$$R(\%) = \frac{2.35\sqrt{FJ}}{J} \qquad (3.5)$$

F is the Fano factor and requires a very detailed knowledge of the detector to be calculated. For semiconductors and gases this value is below one meaning that the resolution is actually better than expected. For scintillators F=1 which leads to the original result [1].

In polarimetry some resolution is required but it is not the most important property of the detector.

3.1.5 – Polarization Modulation Factor

The polarization modulation factor Q is an indicator of a detector's intrinsic capability to perform polarimetric measurements. It refers to the spatial response of a polarimeter to a polarized beam [3]. For a Compton polarimeter (polarimeter that makes use of Compton scattering to measure the polarization of a beam) as the one presented in this work, it is the Compton scattering asymmetry that provides an indication of the polarization. As such Q can be found with the following expression:

$$Q = \frac{N_{\perp} - N_{\parallel}}{N_{\perp} + N_{\parallel}} \tag{3.6}$$

Where $N_{\perp}$ and $N_{\parallel}$ are the number of detector counts in two orthogonal directions consistent with the maximum and minimum of the scattered photons distribution respectively. This expression is equivalent to 2.7. The shape of Q as function of the polar angle is equal to that of the degree of polarization shown in figure 2.10 and has a theoretical maximum at:

$$Q = \frac{\sin^2\theta}{\varepsilon + \varepsilon^{-1} - \sin^2\theta} \tag{3.7}$$

A detector can never surpass this limit but the objective when building one is to reach it.

3.1.6 – Minimum Detectable Polarization (MDP)

This last property refers to the minimum polarization a beam can have in order to its polarization be resolved by a device. There are several variables at hand when calculating the value of MDP since it is not only dependent on the detector but also on other factors such as observation time T, background B and source flux ϕ_S:

$$MDP = \frac{n_{\sigma}}{A\varepsilon\phi_S Q_{100}} \sqrt{\frac{\varepsilon A(\phi_S + B)}{T}} \text{ [4]} \tag{3.8}$$

A, n_{σ}, and ε retain their previous meaning and Q_{100} is the modulation factor for an 100% polarized beam. One can see the importance of this property since it will set a threshold for the degree of polarization that can be measured. A few ways to enhance this value, i.e., to lower it are, increasing the area of detection, which is always dependent of design constraints in a space mission, increasing the observational time, which is not always possible due to the mission's observation schedule, diminishing the background through the use of some systems that will be discussed or simply by optimising a detector for polarimetry which will result in higher values for ε and Q_{100}. It is this last option that is pursued in the development and study of polarimetry detectors and ultimately in this work.

3.2 – Detector Working Principles

Despite being described by the same simplified model there are several types of detectors. As it can be seen in [1] this subject is vast but here an effort is made to summarise the primary types of detectors. These are separated mainly by the material that composes them though there are some more specific detectors. The categories herein presented are gaseous detectors, scintillators and semiconductors.

3.2.1 – Gaseous Detectors

Taking into account a simplified detector it is easy to see that the success of charge collection will depend on the medium that fills the detector. Generally, gases are the medium where electron and ion mobility is higher. Logically the first detectors to be developed were of this kind [2]. The simplest case of one such detector is a container, let us say cylindrical, filled with gas, usually a noble gas. Radiation incident on the detector volume interacts with the gas, ionizing it. In this situation the ionized atoms and electrons will just recombine. If an electric potential is applied between the two bases however, the ionized particles will drift towards the anode or the cathode ionizing the gas more until they are collected as shown in figure 3.3.

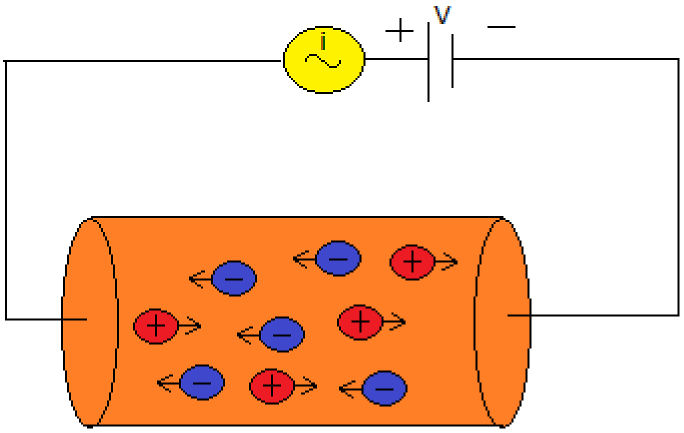

Figure 3.3: Basic cylindrical model of a gaseous detector.

The mean number of pairs created is proportional to the energy deposited. However, this proportionality does not apply to the number of charges collected which is also dependent on the voltage V. As stated before at V=0 there is no drift and the ionized particles will simply recombine. As voltage is raised however the ionized particles will start to be collected and a current arises until every charge is collected and an increase in voltage is futile. Gaseous detectors working in this region, where the voltage versus number of ions collected function reaches a plateau as show in figure 3.4, are named Ionization Chambers and are useful to measure gamma-ray or large fluxes of radiation [2].

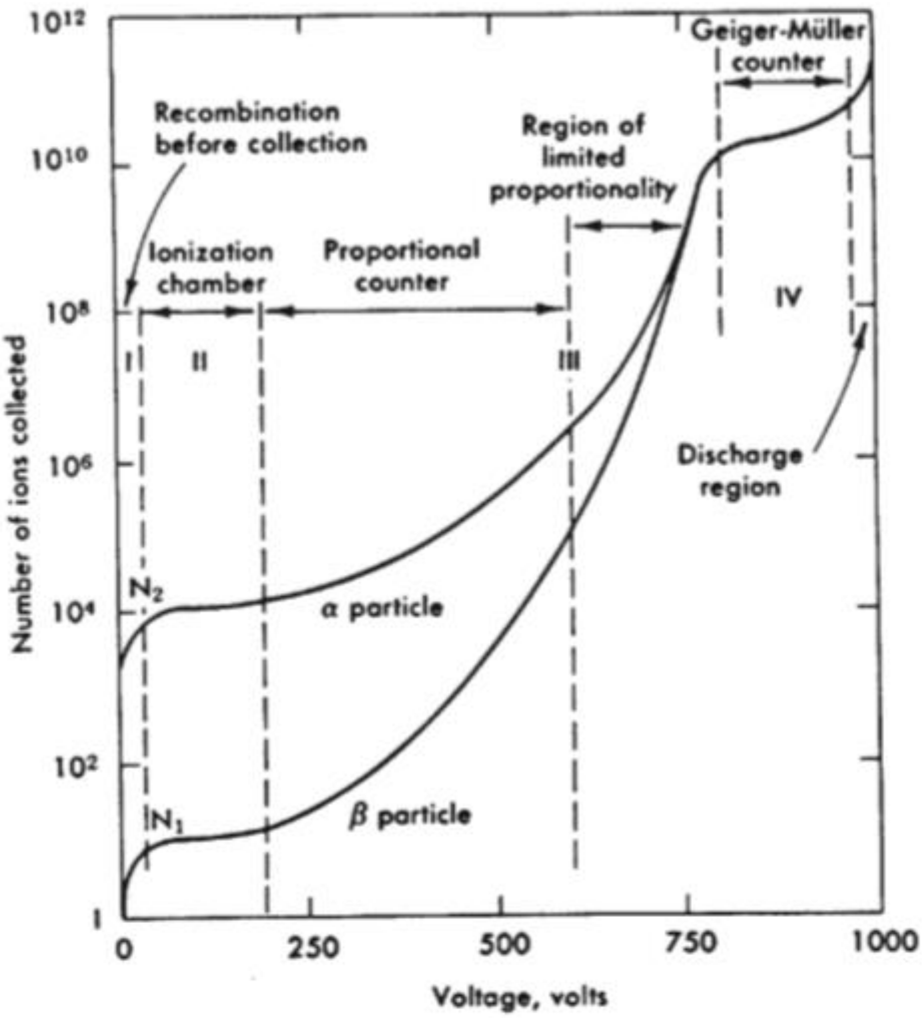

Figure 3.4: Number of ions collected as a function of the voltage applied in gaseous detectors [2].

Other regions of interest are the proportional and the Geiger-Muller counter regions. In the first case the electric field is so strong that primary particles will collide with others and produce an ionization avalanche. The current produce due to an interaction will be a few orders of magnitude higher than that for the Ionization Chamber and will be proportional to the voltage, hence the name, but still proportional to the primary ionization. This means that even for small energies the current will be high enough to be measured. As for the last case the voltage reaches a value that causes discharges in the detector saturating it independently of the incident energy. In this case a quenching gas must be added to absorb photons emitted by the de-excitation of the gas molecules [2]. This way the detector will not be able to distinguish between two different energies but will be very sensible to any radiation no matter the energy. This makes it a very good count detector and very useful to monitor sources. There are more concepts like the multi-wire proportional chamber but they shall not be discussed here.

3.2.2 – Scintillators

Scintillators are unique radiation detectors since their response does not follow the simplified detector model linearly. Atoms and molecules that compose scintillator materials are excited by the radiation crossing its volume. Without a potential to attract the free electrons de-excitation will occur resulting in the emission light, usually in the visible part of the spectrum. Though this alone is not sufficient to make a reading, if the scintillator is both transparent to its own radiation and coupled to a Photo Multiplier Tube (PMT), then a signal is produced that is proportional to the incident radiation energy. A typical assemble of one of such detectors can be seen in figure 3.5.

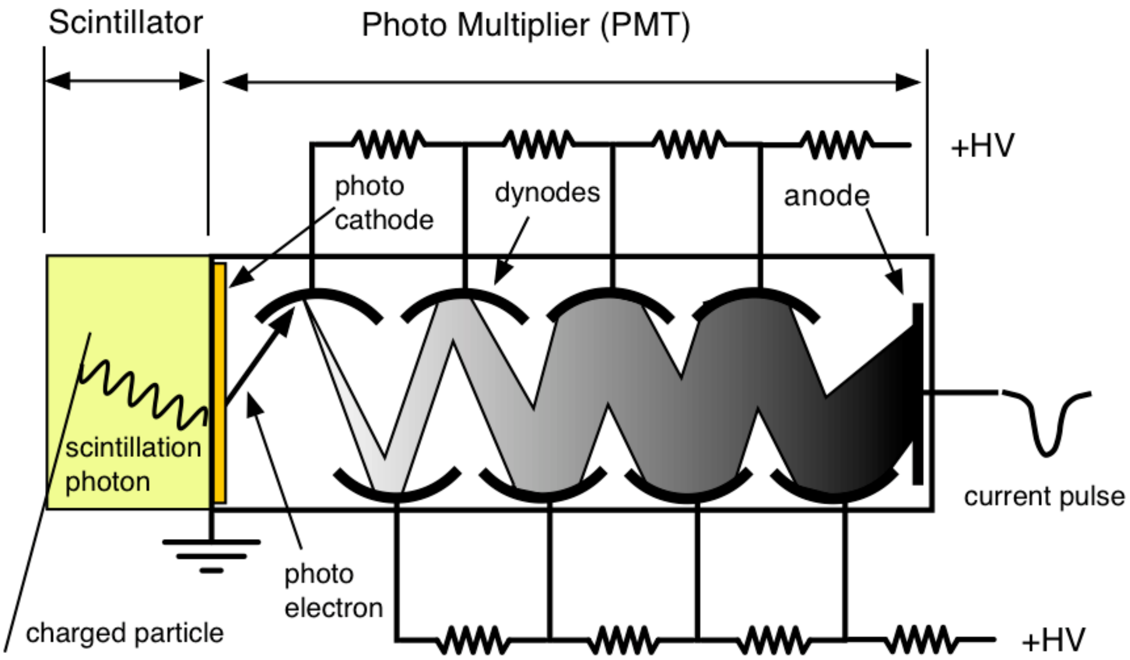

Figure 3.5: Scintillator coupled with a Photo Multiplier Tube [5].

Incident radiation that interacts in the scintillator will result in scintillation photon's that in contact with the photo cathode of the PMT will free electrons from it. Due to the disposition of the dynodes, as it can be seen in the figure above, the electrons be accelerated towards the dynodes which will result in more free electrons. These will then travel towards the next dynode as in the image (successive dynodes are at a higher potential) multiplying the net number of electrons and raising a pulse that can be measured. After a certain energy threshold that is dependent on the scintillator material, the output current will be proportional to the energy of the incident radiation making the assemble energy sensitive [2].

There are several types of scintillator materials most with low atomic number Z which makes them bad gamma-ray detectors. Scintillators with high Z exist however mostly inorganic ones with phosphors [2].

3.2.3 – Semiconductors

Semiconductors or solid-state detectors are similar to gaseous detectors the main difference being the change of medium from a gas to a solid semiconductor. The charge creation however is different in semiconductors since radiation passing through the detector will create electron-hole pairs instead. Due to the energy band structure will be me an order of magnitude greater than that for the gaseous case.

The periodic lattice of crystalline materials establishes the allowed energy bands for electrons. These bands have gaps between them. In figure 3.6, the gap between the valence and the conduction bands can be seen for both insulators and semiconductors.

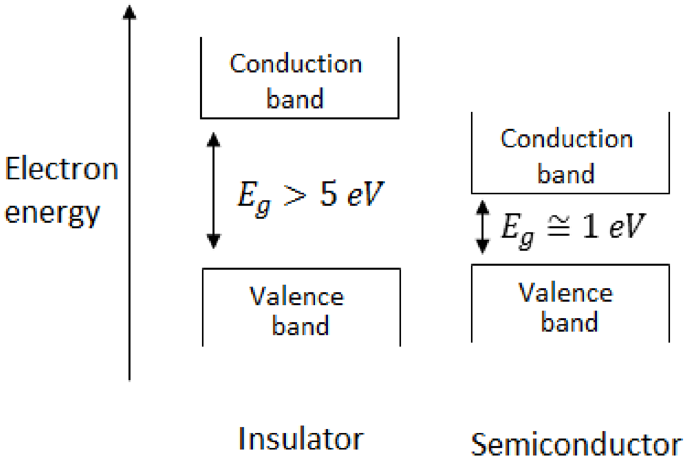

Figure 3.6: Band structure of electron energies in insulators and semiconductors. The size of the gap determines if a crystal is an insulator or a semiconductor [1].

The valence band corresponds to the outer-shell electrons that are bound to specific sites within the crystal. Electrons in the conduction band on the other hand, are free to migrate through the crystal. In the absence of thermal excitation the valence band will be completely filled and the conduction band will be empty. Since the energy gap between these two layers is very small for semiconductors, around ~1eV, thermal excitation will allow some electrons to change bands leaving behind a "hole". As the temperature rises the probability that a pair is created increases from zero to [1]:

$$P(T) = CT^{\frac{3}{2}}\exp(-\frac{E_g}{2kT}) \qquad (3.9)$$

Where T is the temperature, C is a constant intrinsic to the material, E_g is the energy gap between the valence and conduction bands and k is the Boltzmann constant. If no other factors other than the temperature are at work then the pairs will recombine.

Impurities with different number of electrons in the valence band in semiconductors will cause an unbalance between the number of electrons and holes. A lower number of electrons will cause an excess of holes while the opposite will enhance the number of electrons in respect to the number of holes. Semiconductors with this properties are said to be p or n doped respectively. One can then introduce donor impurities knowingly in order to make this properties appear [3].

Generally both p and n doped semiconductors are joined in the same device. Since the p one will have an excess of holes and the n one an excess of electrons a new region subject to an electric field will appear as shown in figure 3.7.

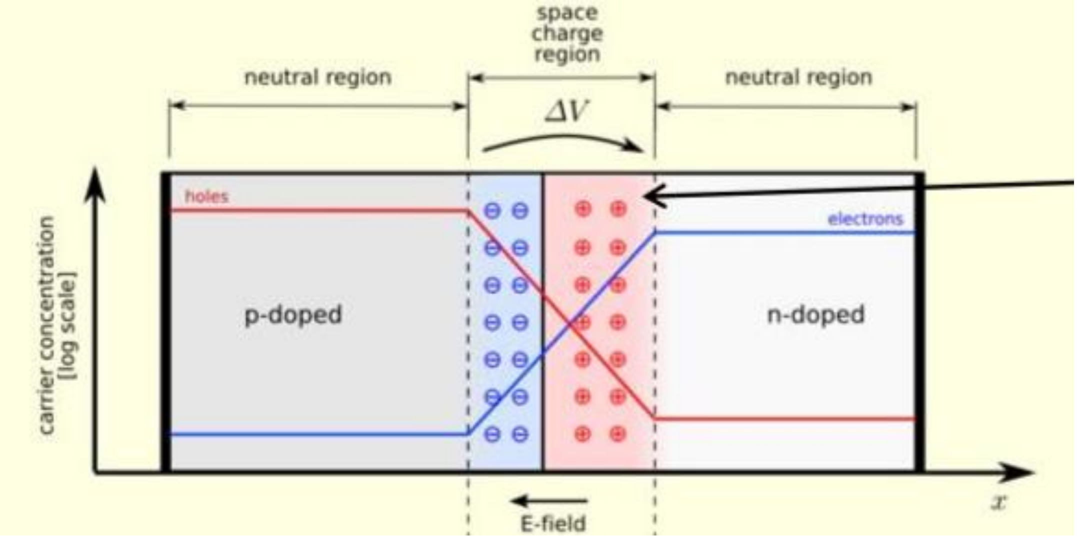

Figure 3.7: Schematics of the joined p an n doped semiconductors.

Due to the potential in this region electrons and holes that appear due to thermal excitation will drift towards the p-doped and the n-doped regions respectively. We can now know that if new pairs appear in the depleted region they must be caused by incident radiation. Applying an electric field between the whole volume allows the collection of these pairs and the measure of the radiation. Since there is a greater number of carriers in this cases than in the scintillator detectors the energy resolution will be better.

There are several materials that compose these crystals each with its own advantages

-Silicon (Si)

Silicon is the 14th element of the periodic table. It has Compton scattering as its primary interaction with gamma-rays in the hundred keV region. This is both an advantage and a disadvantage of the material since most radiation in this energy band will interact with it mainly by Compton scattering, the mechanism that gives information about the polarimetric properties of the photons, but with low efficiency.

- Germanium (Ge)

Unlike in Silicon, Compton scattering is not dominant across the 0.1-1 MeV energy band giving it a better efficiency. This result is not surprising given its higher atomic number Z=32. Germanium also has the best resolution [1] of the 3 materials discussed here but needs to be cooled to low temperatures increasing the complexity of a space mission that used it.

-Cadmium Telluride (CdTe)

CdTe is the most common semiconductor material with high Z. Its higher Z makes it the material with better efficiency. Another feature of CdTe is that it functions at room temperature unlike germanium therefore requiring less payload. CdTe is often doped with Zinc as in the case of the used detector, POLCA II.

The linear attenuation coefficients in the 0.1-1MeV range of this elements as well as the ones for a plastic scintillator, aluminium and a league of stainless steel (used in the simulations in chapter 5) can be found in Annex A.

3.3 – MeV Telescopes

Due to the nature of the interactions that occur between gamma-rays in the MeV range and matter, new telescope concepts had to be developed. Unlike in photoelectric effect, photons undergoing Compton scattering or pair production do not transfer all of their energy in the detector volume in one interaction. In fact, Compton scattering produces a continuum of energies with only a fraction of the photon's energy, which does not allow to know the incident's photon total energy while pair production produces an electron and a positron instead of leaving its energy in the detector.

In this section I will discuss the concepts that were developed to surpass this problem as well as two solutions that can be used increase the sensitivity of the instruments.

3.3.1 – Interaction of Light with Matter

In order to develop a telescope one must know how light interacts with matter. This happens mainly via three processes, the Photoelectric Effect, Compton Scattering and Pair and Production making them the basis of gamma-ray detection.

3.3.1.1 - Photoelectric Effect

The Photoelectric Effect gave Einstein his Nobel Prize in 1921 for its explanation on one of his famous 1905 papers [6]. It consists in the absorption of a photon's total energy by an atomic bound electron releasing it from the atom with. If the photon has energy lower than the electron's binding energy however no interaction will occur and the photon will follow its path. Therefore, the energies required for this interaction to take place must be higher than the electron binding energy which can be from a few electrovolts in light atoms to more than a hundred keV. The atom will then be left in an excited state. Its de-excitation will emit a photon that is characteristic of the said atom. Figure 3.8 describes the process.

The electron after the interaction will have a total kinetic energy $E_k = hv - E_b$ where h is the Planck constant, v is the frequency of the photon and E_b is the bound energy of the electron. This will leave room for an electron in an upper band to migrate to the ground one emitting the characteristic energy equal to the difference between the two shells bound energy. This interaction completely stops the radiation since the photon will no longer exist after it.

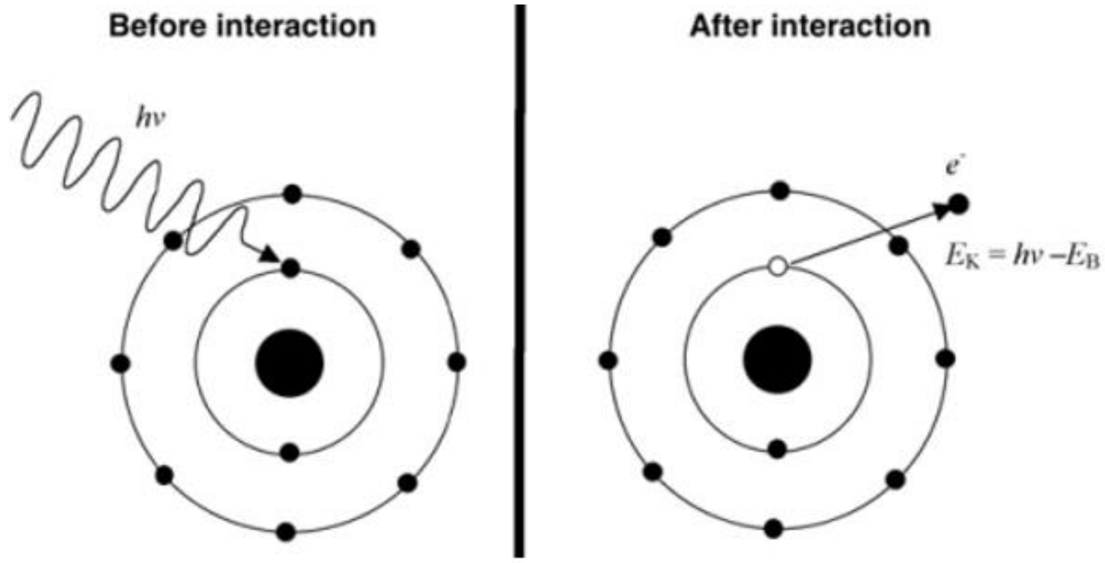

Figure 3.8: On the left a photon with energy hv interacts with an electron in the k-band. On the right the electron that interacted with the gamma-ray leaves the atom with total energy equal to the photon’s energy subtracted by the bound energy of the electron.

3.3.1.2 - Compton Scattering

Compton scattering has already been discussed at length in chapter 2 section 2.2.4. It is noteworthy to say that Compton scattering besides being a mechanism that polarizes radiation is also the basis for a telescope concept and polarimetric techniques in the MeV region.

3.3.1.3 - Pair Production

Pair production consists in the process by which a photon is converted in a positron and an electron in the vicinity of a nuclei. This only becomes possible when the energy of photons reaches 1.022 MeV, the sum of the masses of the two resulting particles. It is fairly easy to see that the 1.022 MeV will go to the masses of the particles while any excess energy will be converted into momentum. In the energy range of this work energies will not be sufficiently high for this mechanism to occur. Nonetheless, this is a very important mechanism in MeV astronomy and it should be analyzed more deeply.

Figure 3.9 shows the transformation of a photon with energy hv into an electron/positron pair. Imposing momentum and energy conservation one arrives at the following equation for the conservation of energy:

$$hv = E_{k+} + E_{k-} + 2m_e c^2 + E_R \tag{3.10}$$

hv is once again the energy of the incident photon, E_{k+} and E_{k-} are the kinetic energies of the positron and the electron respectively, m_e is the mass of the electron, c the velocity of light and E_R the recoil energy of the nuclei. Without this recoil energy conservation would not be possible making it impossible for this process to occur in vacuum. The other terms refer to the fact that a fraction of the photon's energy must be converted into the mass of the two charged particles ($2m_e c^2$), which explains the threshold of the interaction, while any excess to this value should be attributed to the other terms.

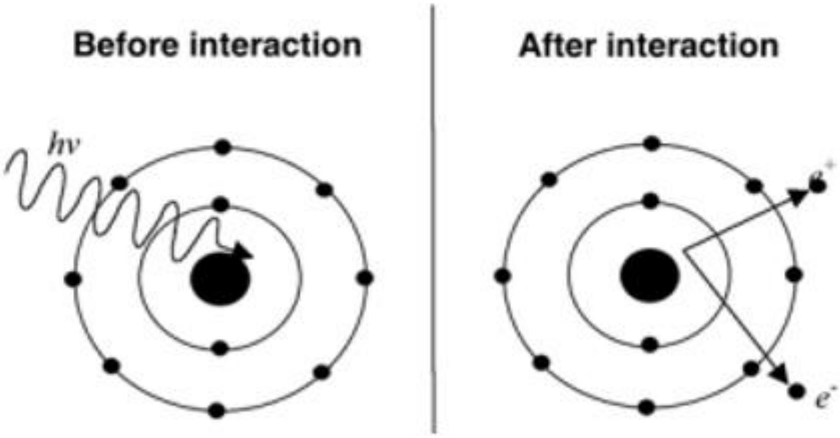

Figure 3.9: Pair production in the presence of a nuclei.

Finally let us analyse figure 3.10. In it the predominance of each interaction can be seen as a function of energy and of the atomic number the interaction occurs. One can see that for the MeV range three stages are observed. In the first, up to the 0.1 keV mark, photoelectric effect prevails over Compton scattering for most atomic numbers, the exception being low mass atoms. Above this energies Compton scattering starts to be the most likely interaction up to the 10 MeV region where Pair Production starts to be dominant. The latter starts to be relevant at these energies despite its lower threshold. These 3 regions require different solutions as far as astronomy is concerned. The discussion of these solutions is found in the next 2 sub-sections.

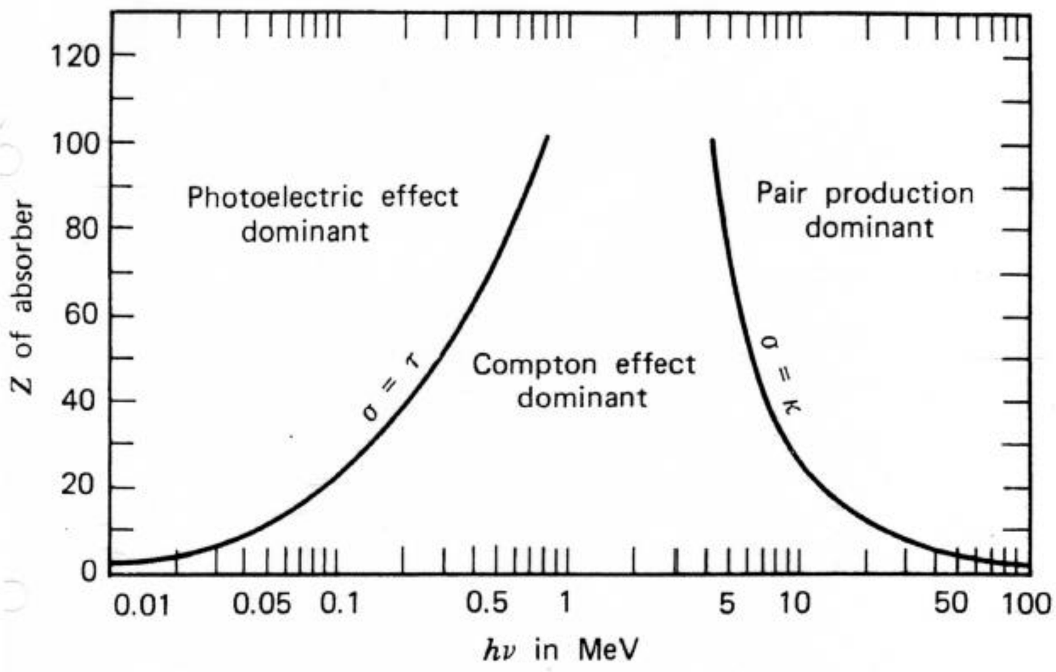

Figure 3.10: Dominance of photon interactions with matter as a function of their energy and the atomic number of the matter they interact with [1].

3.3.2 – Compton Telescopes

The area between 1 and 10 MeV is a difficult one for astronomy. Its high energy nature, which leaves coded masks (see section 3.3.4) obsolete, and corresponds to the minimum in the cross-section for interactions of photons with matter, coupled to the lack of a focusing lenses solutions makes it harder to detect this radiation [8]. These difficulties are somewhat compensated by the directional information Compton and Pair production can give.

In the case of a Compton Telescope information about the incident photon's energy and direction comes from Compton scattering. Since a photon undergoing Compton scattering does not lose all of its energy two detectors, in different planes, working in series are required. As it can be seen in figure 3.11, the photon first interacts in the upper detector D1 by Compton scattering. For this interaction, a low Z material is preferred so that the efficiency towards Compton scattering is high enough and so that only one interaction will occur in it. The emerging photon is then expected to interact via photoelectric effect in the second layer D2 so that the full energy of the incident photon is known. A high Z material is then required to compose this layer. From the Compton mechanics studied in the last chapter one can use the information about the energy to calculate the angle at which the first interaction occurred. This will create a cone like field of view from where the incident photon's initial direction is likely to lay in [7].

This concept offers both a low background noise with temporal analyses between both interactions and a vast energy range making it the most attractive method in this energy range.

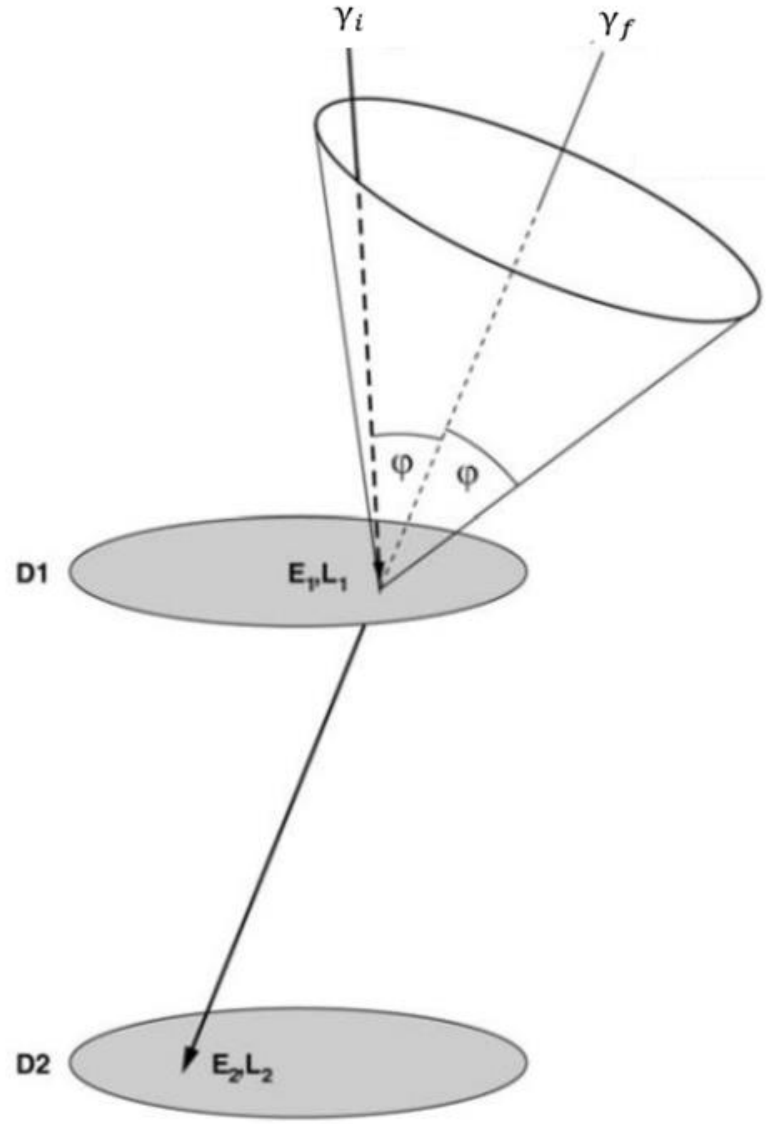

Figure 3.11: Concept of a Compton Telescope [7].

3.3.3 – Pair Production Telescopes

For higher energies (>10 MeV) pair production surpasses Compton scattering as the main interaction of photons with matter. This case is simpler than the last one since the resulting charged particles from pair production are easier to track given their charged nature [7].

Both telescope concepts require anti-coincidence systems made of low absorption coefficient materials in order to provide charged particles background rejection.

3.3.4 – Coded Masks

For energies below 1 MeV, where photoelectric and Compton effects dominate, one solution to improve the sensitivity of instruments found was the use of coded masks.

A coded mask consists in an opaque matrix with holes and is placed above the detector so that it that casts a shadow on it. The shadowed area depends on the source's relative position and has the same shape as the coded mask. Computer algorithms are required to translate the information from the shadow. Figure 3.12 shows this concept.

As one can see an incident flux normal to the mask area will highlight an area in the detector equal to that of the mask. A flux incident at an angle will highlight a different area. An algorithm can be constructed based on the mask shape that will give the source's direction with a precision that depends on the size of the mask elements and on the separation between the mask and the detector. Smaller sizes for the elements and a greater separation enhance the angular resolution.

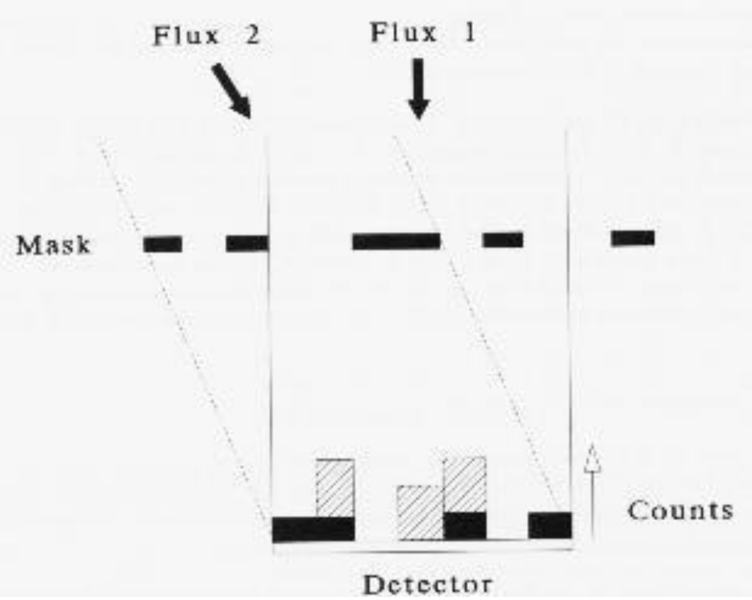

Figure 3.12: Schematic of a coded-mask subject to two different fluxes.

3.3.5 – Laue Lenses

Despite the techniques developed for gamma-ray astronomy sensitivity in the 0.1-100 MeV is still a critical parameter due to the low signal-to-noise relation. In order to address this problem, a lens designed specifically for this energies has been developed. Laue lens consist of a large number of crystals where photons can interact coherently in order to be diffracted as described by Bragg diffraction. The diffraction angle in this case will be very small due to the high energy of the radiation. This leads to an impairment in the energies that can be focus, for example a 511 keV photon would needs at least 10m of focal distance. A great distance between the detector and the lens is then need as projected in the potential mission GRI and DUAL [8]. However, Laue Lenses are currently one of the best options to increase gamma ray telescope's sensitivity up to a MeV.

3.4 – State of the Art

3.4.1 – The past and the present

Gamma-Ray astronomy is a recent branch of astronomy with the first successful detection of high energy gamma-rays from space being made in 1961 by the EXPLORER-11 [9]. From that point several missions were launched with different grades of success. Figure 3.13 shows a detailed view of gamma-ray astronomy history from the EXPLORER-11 and the VELA satellites that followed it and that discovered Gamma Ray Bursts in 1967 [10], up to the BEPPO-SAX launched in 1997 that clarified the cosmological origin of these bursts [9].

As it can be seen the history is quite extensive especially when we add the INTEGRAL satellite launched in 2002 [11], the SWIFT launched in 2004 [12] and FERMI launched in 2008 [13]. These three satellites in addition to CGRO comprise most of the history of recent gamma-ray astronomy. From figure 1.2 in section 1.1 one can see that INTEGRAL, CGRO and FERMI measure most of the gamma spectrum (only the high end is inaccessible). Swift on the other hand was designed to study GRB's and as such it has a narrower window in the gamma range since it focuses mostly on the peak part of the spectrum of such events (a few hundred keV) and on their x-ray, ultraviolet (UV) and optical afterglow [12]. Since the FERMI energies are out of the scope of this work I will analyse only the CGRO and INTEGRAL.

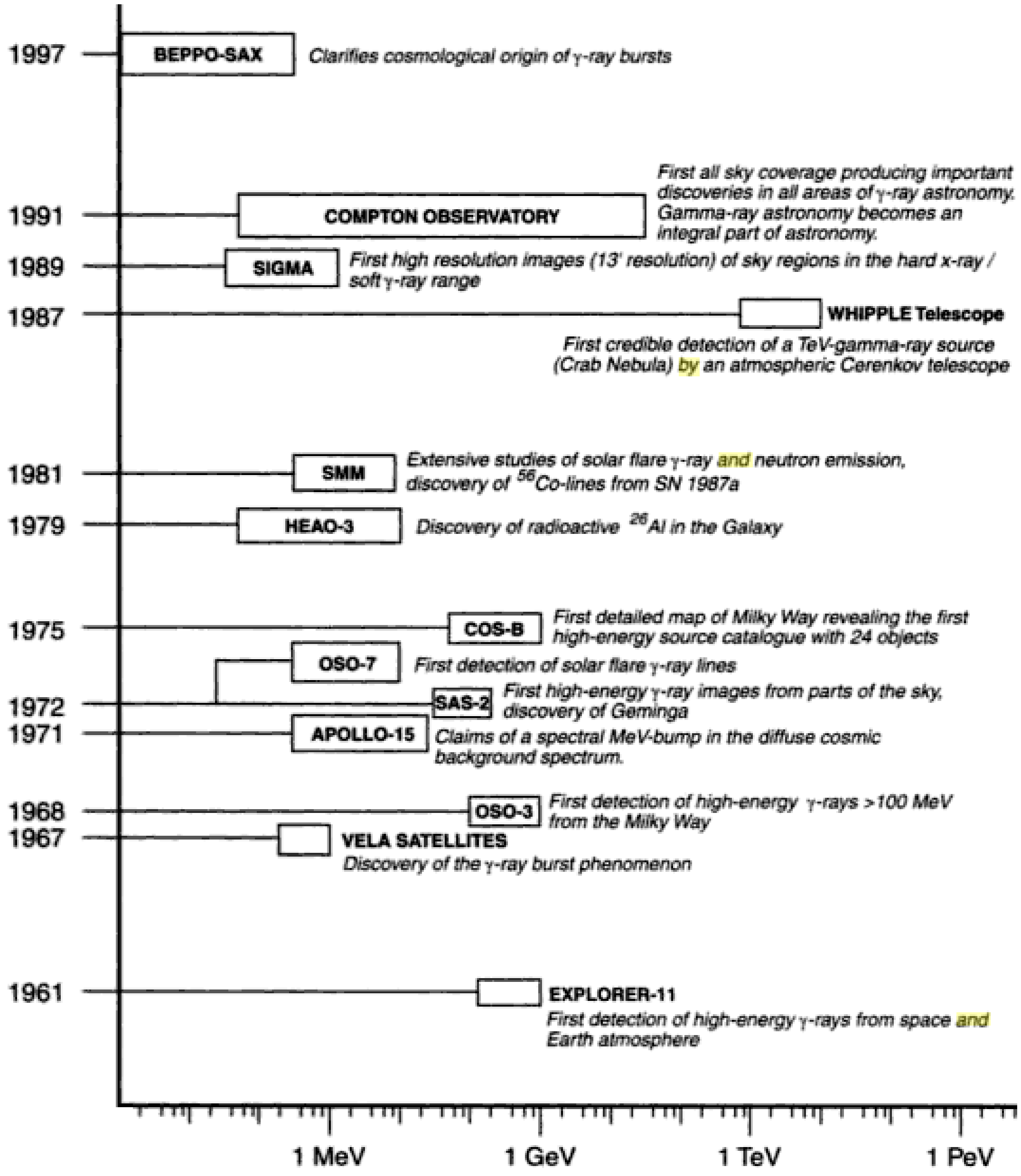

Figure 3.13: Timeline of the development of gamma-ray astronomy up to 1997 [9].

3.4.1.1-CGRO

The CGRO is a NASA mission dedicated to study, as the name indicates, the gamma ray sky. It has 4 instruments, the Burst and Transient Source Experiment (BATSE), the Oriented Scintillation Spectrometer Experiment (OSSE), the imaging COMPTEL and the Energetic Gamma Ray Experiment Telescope (EGRET) destined to cover a wide range of energies from 20 keV up to 30 GeV.

BATSE covers the lowest part of the spectrum from 20 keV to 600 keV. This is a special zone since it coincides with the peak of GRB's. It is with no surprise then that the mapping of GRB's in sky done by this instrument led to the first proof that this events have a cosmological origin [14]. The instrument consists in eight detector modules similar to each other. Each modules is composed by two NaI(TI) scintillation detectors, one optimized for sensitivity and directional response and the other for energy coverage and resolution [14].

OSSE consists in four NaI(TI) scintillator detectors that scan the 0.05-10 MeV region. These are surrounded by tungsten collimators in order to enhance the field of view (FOV). OSSE responded to GRB triggers from BATSE since it was sensitive to the energy regions at which this occur and to solar flares enhancing its science capabilities [15].

As for COMPTEL its energy sensitivity ranges from 0.8 to 30 MeV. since polarimetric measurements can be made with it, a more detailed analysis must be done. As it can be seen in figure 3.14 this instrument has two layers. The upper one uses a liquid scintillator, NE 213A, for each of its eight modules while the lower one uses NaI crystals. As one may recall section 3.3.3 this geometry makes up the one of a Compton telescope with a separation of 1.5m. Each detector is also entirely surrounded by thin anti-coincidence shields of plastic scintillators [16]. Despite the low modulation factor Q value for the instrument, a 14 day observation would allow a minimum detectable polarization of 29.5% and 58.6% in the energy ranges from 750 to 1125 keV and 1500 keV respectively [3].

As for the last instrument, EGRET consists in a spark chamber for direction measurement and a NaI(TI) calorimeter. It works at energies above 20 MeV all the way up to 30 GeV making it beyond the scope of this work [16].

3.4.1.2-INTEGRAL

INTEGRAL, ESA's INTErnational Gamma-Ray Astrophysics Laboratory was designed to study energies between 15 keV and 10 MeV. X-ray and optical instruments were also present in order to make simultaneous observations across de electromagnetic spectrum. One of the INTEGRAL innovations was the use of semiconductors as detectors, a feature not found in the CGRO. In fact two of the main instruments, SPI and IBIS were made of Germanium and Cadmium Telluride respectively (the names might be remembered from figure 1.2, section 1.1. This brings the count of detection instruments to four. Since only two of those work in the region of interest for this work only those will be considered [18].

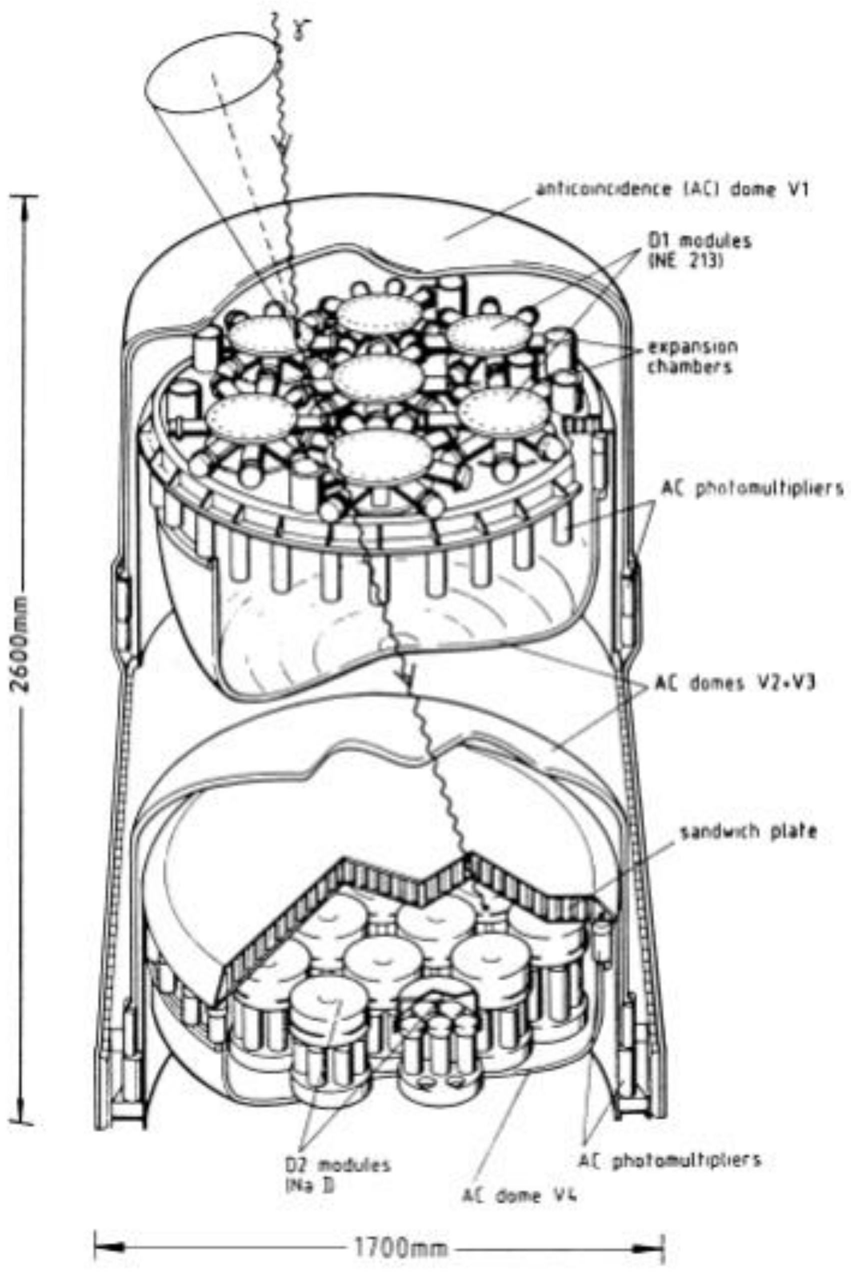

Figure 3.14: Schematics for the COMPTEL instrument aboard the CGRO [3].

SPI uses an array of 19 hexagonal high purity germanium detectors cooled to 85 K. The cooling system as it was expected increases the payload weight by a lot but is compensated by the better resolution that Germanium can offer. In addition to it a coded mask and a veto system working in anti-coincidence are also present offering a better angular resolution and decreased background [19].

The second gamma-ray instrument is the imager on-board INTEGRAL (IBIS). Its upper layer of 16 384 CdTe pixels measuring 4x4x2 mm each and the bottom one of 4096 caesium iodide (CsI) pixels each with 9x9x30 mm provide sharper imagers than any other previous gamma instrument. Since the upper layer has small thickness it detects mostly low energy gamma rays while the bottom one takes care of the higher energy ones. This is another case of a Compton telescope [20]. The pixelated nature of both instruments makes them potential gamma-ray polarimeters especially for low energies where a Q factor as high as 0.3 can be obtained [3].

3.4.2 – AstroMeV, the future

It has been a while since a gamma-ray telescope has been launched. As INTEGRAL end of operations date approaches, the launch of a new mission becomes more appealing. As mentioned in chapter 1 an extensive study has been done by the AstroMeV Consortium in order to prepare such mission. The instruments in development are expected to surpass the latest missions not only in sensitivity but also in polarimetric performance. It is in order to study the polarimetric performance of the instruments and optimize it that this work is done.

References

[1] Glenn F. Knoll. Radiation Detection and Measurement 3rd Edition

[2] ''Techniques for Nuclear and Particle Physics Experiments - A How-to Approach'' Second Edition Revised - W. R. Leo

[3] F. Lei, A. J. Dean, and G. L. Hills, “Compton Polarimetry in Gamma-Ray Astronomy”, *Space Science Review*, Vol. 82, p. 309, (1997)

[4] Martin C. Weisskopf, Ronald F. Elsner, Stephen L. O’Dell, “On understanding the figures of merit for detection and measurement of X-ray polarization”, SPIE conference 7732 (paper 13)

[5] http://wanda.fiu.edu/teaching/courses/Modern_lab_manual/_images/PMT.png

[6] Einstein 1905 O Padrão da Grandeza, Johsn S. Rigden

[7] Khalil, M. Study of Stripped Spectro-Imaging Detectors for a Future Space MeV Telescope

[8] Seminaire de Prospective Scientifique 2014 Appel a Idees, CNES

[9] The Universe in Gamma-Rays, Volker Schonfelder, Springer.

[10] Klebesadel, R. W., Strong, I. B., & Olson, R. A., Astrophys. J., vol. 182, p.L85

[11] http://sci.esa.int/integral/31149-summary/

[12] http://swift.gsfc.nasa.gov/about_swift/

[13] http://fermi.gsfc.nasa.gov/

[14] http://heasarc.gsfc.nasa.gov/docs/cgro/batse/BATSE-desc.html

[15] http://heasarc.gsfc.nasa.gov/docs/cgro/osse/OSSE-desc.html

[16] http://heasarc.gsfc.nasa.gov/docs/cgro/comptel/compteldesc.html

[17] http://heasarc.gsfc.nasa.gov/docs/cgro/egret/egret_doc.html

[18] http://sci.esa.int/integral/47360-fact-sheet/

[19] http://sci.esa.int/integral/31175-instruments/?fbodylongid=719

[20] http://sci.esa.int/integral/31175-instruments/?fbodylongid=720

Chapter 4

Compton Polarimetry

Now that the mechanisms that originate polarized gamma-rays and the ways to detect them have been discussed I will discuss the developed techniques to measure the degree and the direction of polarization. In this work the analysis of the Compton scattering photon's distribution asymmetry is used to measure the polarization. Notice however that photoelectric and pair production polarimetric techniques exist but are beyond the scope of this work.

In section 2.2.4 the Compton scattering mechanics was presented. From equation 2.28 it has been found that an asymmetry will arise in the azimuthal distribution of Compton photons generated by a polarized beam. It is this asymmetry that is analysed and that allows to measure the polarization a beam. The figure below shows the expected shape of the azimuthal angular distribution of a polarized beam of photons after being Compton scattered.

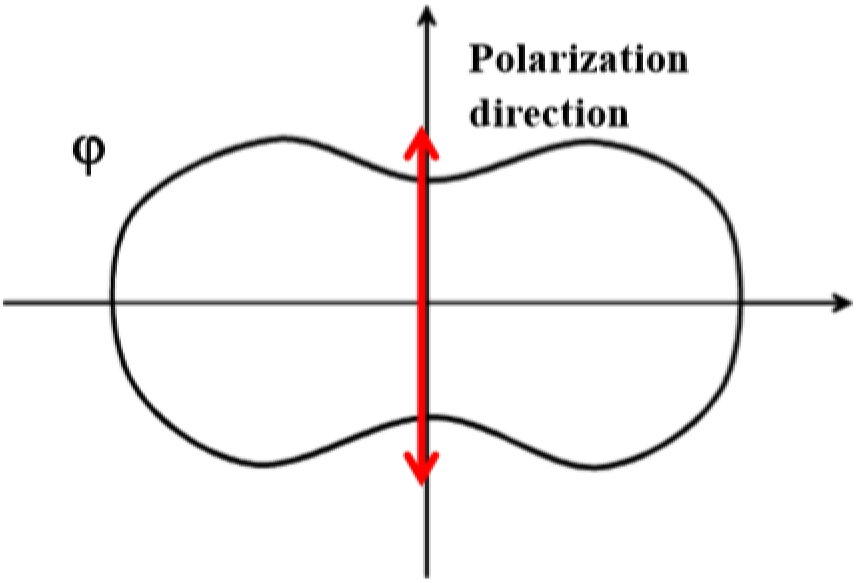

Figure 4.1: Azimuthal angular distribution of a polarized beam of photons after being Compton scattered.

From it we can see that the polarization direction is coincident with the direction through which less photons are Compton scattered. A 90° degree symmetry is also evident. In order to perform polarimetric measurements this distribution must be measured. The measurement can be made with either a rotational or a non-rotational polarimeter [1].

4.1 – Rotational Polarimeters

In the case of a rotational polarimeter two detectors are required, a “scatterer” and a “collector”. The first detector, as name indicates, is used to scatter the incident photons of the polarized beam. The second detector should be placed in the same plane, normal to the incident beam, as the first detector with the function to collect the scattered photons. This geometry can be seen in figure 4.2. Now, rotating the collector around the incident beam’s axis one can obtain the number of photons, N, scattered as a function of the scattering angle η [3]. If the beam is 100% polarized the Q factor of the instrument can be obtained using equation 3.6.

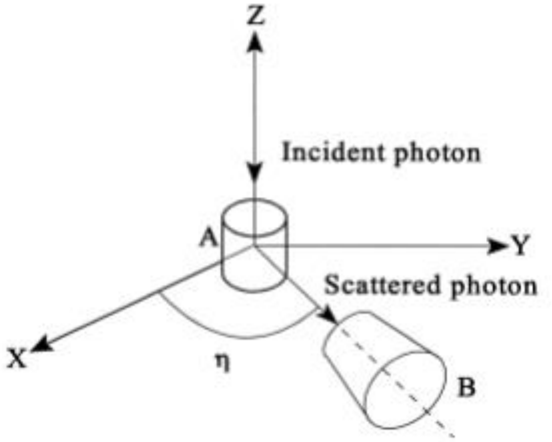

Figure 4.2 Principle of operation of a Compton polarimeter [3].

N will vary as a function of η following a cos(2η) distribution. The same is true for Q. In this distribution it is the peak value that is of interest and will depend on the physical dimensions of both detectors, the presence of passive material, low energy threshold and background level [3]. The peak value for a 100% polarized beam, Q_{100}, will work as a scaling factor to calculate other degrees of polarization using the following expression:

$$\Pi = \frac{1}{Q_{100}} \frac{N_{\perp} - N_{\parallel}}{N_{\perp} + N_{\parallel}} \qquad (4.1)$$

Here $N_{\perp}$ and $N_{\parallel}$ correspond to the maximum and minimum of N(η) respectively.

4.2 – Non-rotational Polarimeters

The rotational polarimeters present a great problem to space missions. Its rotating nature adds volume and mass to a mission that is in need for both as well as complexity. To avoid this problem a series of collectors can be distributed around the scatterer which allows for simultaneous acquisition for several scattering angles without the need to rotate. This brings advantages not only as hardware is concerned but also time-wise since the simultaneous nature of the measurements for all angles will lead to a decrease in the acquisition time by a factor equal to the number of angles the rotational polarimeter has to measure. Examples of non-rotational space polarimeters such as COMPTEL and IBIS have been described in chapter 3. Both cases were not designed or optimized for polarimetry but their pixelated nature gives them their polarimetric capability.

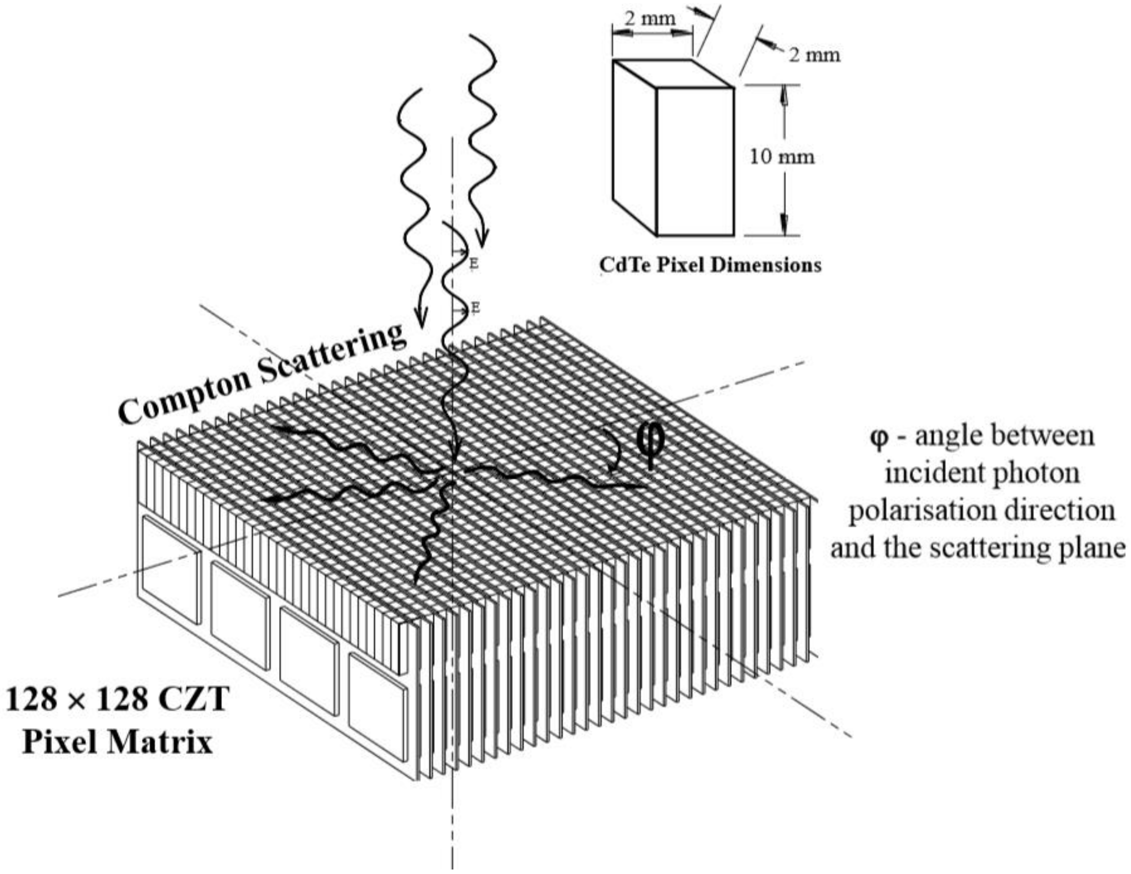

Figure 4.3: Compton scattering in a pixelated CZT detector [4].

In figure 4.3 the schematics for a pixelated polarimeter is presented. Its pixelated nature gives positional information on the scattered photons given that a single pixel is radiated making it possible to perform polarimetric measurement. This is not without some adversity, the same analysis as the one for rotational polarimeters is not valid in this case where each element is unique in its response. In the next two sections analysis methods and systematic effects removal will be discussed. This discussion is based almost entirely on [3] so no references will be made in this regard.

4.3 – Data analysis for non-rotational polarimeters

There are two techniques that evolved in polarimetry for the analysis of polarimetric data of non-rotational instruments. Both divide the detection area in sections and identify the difference in the number of interactions in each section to reach a value for polarization. To better visualize this and to adapt to the present work I will use the following schematics:

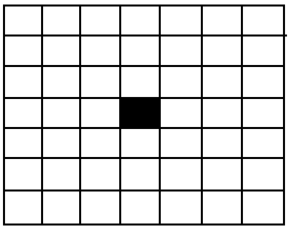

Figure 4.4: Schematics for the 7x7 pixelated detection area.

In the figure each square represents a pixel of the detector. The dark pixel should correspond to the irradiated one and as such I will assume that its counts are equal to zero so that it is not taken into account.

4.3.1- The Moving Mask Technique (MMT)

In the MMT the detection area is divided into four sections as seen in the left side of figure 4.5 and is rotated in small steps of 2° or 5° as it can be seen in the right side of the same image.

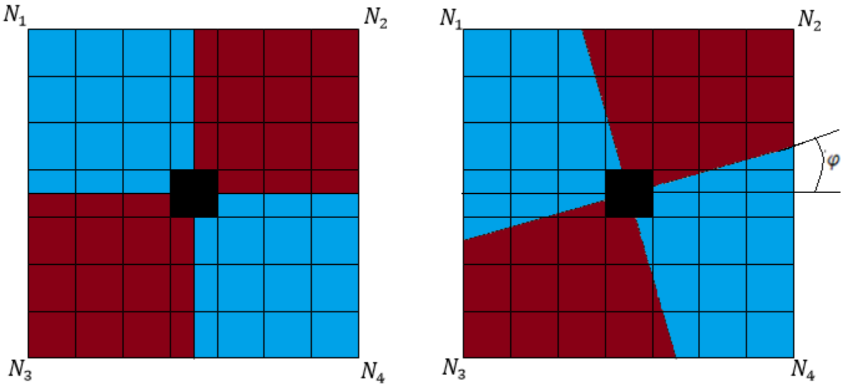

Figure 4.5: Illustration of the four quadrants in the MMT in the initial state and when rotated by an angle φ. Each quadrant is identified as N_2 and N_3 with the colours blue, and N_1 and N_4 with the colour red.

At each step the Q factor is calculated with following expression:

$$Q(\varphi) = \frac{[N_1(\varphi)+N_3(\varphi)]-[N_2(\varphi)+N_4(\varphi)]}{N_1(\varphi)+N_3(\varphi)+N_2(\varphi)+N_4(\varphi)} \qquad (4.2)$$

The values obtained can then be fitted into $\cos(2\varphi)$ function where the maximum corresponds to the degree of polarization and the angle at which the function is minimum gives the polarization vector.

This technique's results match the analytical predictions exactly. There will be a problem related to the non-independency of the various samplings however. Since a single event will be sampled several times each value will not be independent. To take this into account a reduced mask that uses only a small window of 15° or 24° for example. Each step must then match the mask aperture so that single events aren't sampled more than one time reducing the smearing effect. This procedure is shown in figure 4.6.

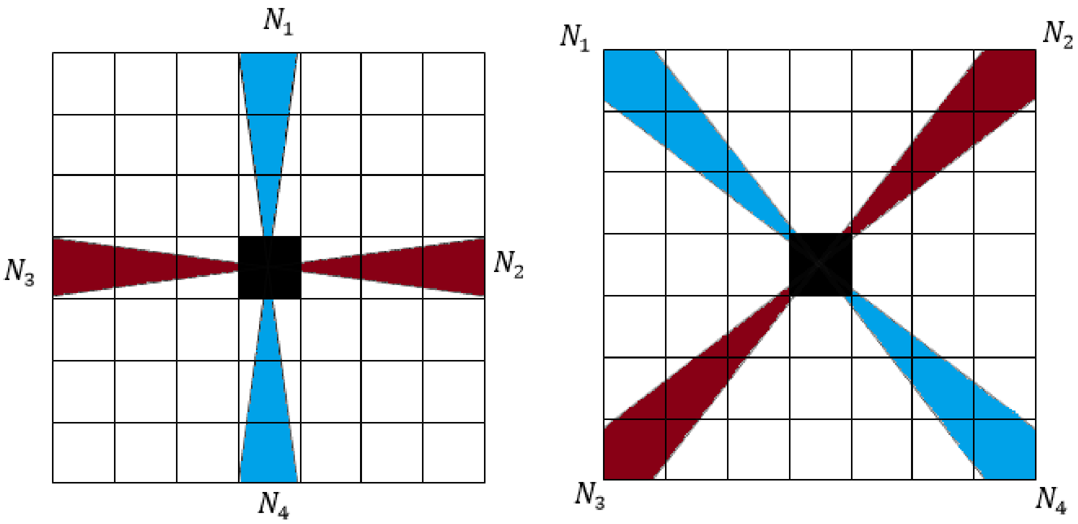

Figure 4.6: Illustration of the MMT using a small window. The angles used are exaggerated for better illustration of the principle but there's no loss of generality transitioning to bin of 24° or 15°.

4.3.2- The Radial Bin Technique (RBT)

The RBT differs from the MMT as there is no rotation of the mask. Instead the plane is divided into radial bin of the same size (usually of 15° or 24°) where each event is placed. N(φ) can be obtained with these bin allowing Q to be calculated. A problem will arise in this case, as the bin size is increased Q decreases. This is the same problem as resolution in a screen, as the pixel size grows smaller the resolution is enhanced and details become each time more apparent. However as bin sizes decreases the statistics for each bin will also decrease. A consensus must then be made between a higher Q factor and a smaller bin size and better statistics and a bigger bin. Values between 10° and 30° are considered suitable. Both techniques are valid for polarimetric analysis.

In this work several masks were tested changing the aperture and the step sizes. The mask chosen follows the RBT dividing the matrix in 24 bins of 15° aperture each. The number of photons that interact in pixels that are included in more than one bin is divided according to the fraction of the pixel that is contained in each bin.

For each bin each pixel in the first quadrant (correspondent to the N2 quadrant in figure 4.5) was analyzed to see if it was completely included, completely excluded or trespassed by one or both the bin's limiting lines. This analysis excluded pixels outside this quadrant since its bins do not contain pixels that do not belong in it. The bins in the other quadrants were then analyzed by rotating the matrix 90° at a time and repeating the same procedure.

If the pixel is completely included in the bin then its total counts are added to that bin. If the opposite case happens then the pixel is excluded from the bin and no counts are added. In the last case only a fraction is added. This fraction depends on the pixel area that is inside the bin.

To calculate this fraction a few considerations were made. First, a pixel can only be intersected twice by one line. This can be seen in figure 4.7 since the lines dividing each bin start at the origin and end in the borders of the matrix. Second, the first intersection will occur only in the bottom or left border of the pixel and only one of these borders can be intersected in a pixel, never both. Third the second intersection will occur in the top or right borders. Once again they cannot be both intersected. The second and third considerations are a direct consequence of the treatment being all made in the first quadrant. Once again this can be seen in figure 4.7.

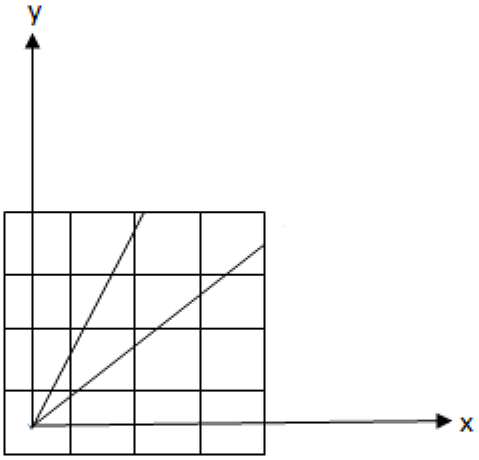

Figure 4.7: Referential for the area calculations. The origin corresponds to the center of the central pixel in the matrix.

With this in mind the intersection positions can be found with the bin's limiting lines equation and the border conditions for each pixel. The first intersection provides the x coordinate where the line enters the pixel area, x_1, and the second provides the same coordinate but where the line exits the pixel, x_2. Transforming x_1 and x_2 as well as the b in the line's equation into the pixel referential where the origin (0,0) corresponds to the lower left vertex allows us to calculate the normalized area of the pixel that is contained in the bin.

If the line exits the pixel through the right border of the pixel, (see the top right pixel in figure 4.7) the normalized area, A, will simply be the integral of the line between $x'_1$and x'_2 (coordinates in the pixel referential) in case of the line being the top limit of the bin or 1 minus this same integral in the case of it being lower limit.

$$\begin{cases} A = \int_{x'_1}^{x'_2}(mx + b'\ )dx, & \textit{in the top limit} \\ A = 1 - \int_{x'_1}^{x'_2}(mx + b'\ )dx\,, & \textit{in the lower limit} \end{cases} \tag{4.3}$$

Where m is the slope of the line. Since the pixel area was normalized the value calculated is already the fraction of the area contained in the bin. We can then add to the bin the number of counts in the pixel times A. If it exits from the top border then x'_2 will be different than 1 and we must add the area of the remaining rectangle to the right. Since the sides of the pixel are 1 then this area is simply 1-x'_2.

In the case that both lines intersect the pixel one must calculate the area for each limit using the equation for the other and subtract both results from one.

Repeating this procedure to each bin one obtains the N(φ) distribution and consequently Q(φ).

4.4 – Systematic effects removal

Now that the basis for polarimetric measurements and analysis has been discussed, a focus must be made on effects that introduce systematic errors to the data. These include non-uniform response of each module (in our case each pixel), off-axis incidence of radiation, background noise and the pixelization effect. The removal of such effects considers a one pixel irradiation but since in the present work a full detector irradiation has been done new corrections were required.

4.4.1- Non-Uniform Response

When a rotating polarimeter is considered one does not have to worry about the effects of different response each component has since the same one is used to measure N(φ). When a non-rotating polarimeter is used however several components will be used. In our case these components correspond to different pixels that due the nature of their fabrication and use will respond differently to the same radiation. In the case of a pixelated detector this can be seen by a variation in the number of counts pixels will have regarding each other when subject to the same radiation in the same amount of time. This will result in the distortion of the $Q(\varphi)$ distribution and can mask a polarimetric signature or even create a false positive.

The removal of this effect is relatively simple. In order to do so irradiation with a non-polarized beam of each pixel individually in the exact same conditions allows the construction of a response matrix of the pixels. This can also be done direction-wise measuring a quantity, $N_{non}(\varphi)$, that corresponds to the number of counts in a given direction when non-polarized gamma-rays are used. The calibrated number of events $N_{true}(\varphi)$ can then be found using the non-polarized response in that direction $N_{non}(\varphi)$, the polarized response measured $N_{pol}(\varphi)$ and the maximum number of counts obtained N_{max}, which ever direction that maximum corresponds to:

$$N_{true}(\varphi) = \frac{N_{pol}(\varphi)}{N_{non}(\varphi)} N_{max} \tag{4.3}$$

The value of N_{max} divided by $N_{non}(\varphi)$ is the calibration factor and compensates directions with weaker responses.

4.4.2- Off-Axis Incidence

A problem that will occur in space missions is that the detection plane will not be normal to the incident beam direction. If the inclination of gamma-rays is higher than 5°, an asymmetry in the photon's distribution will arise even if the observed emission is not polarized. This asymmetry can affect polarimetric analysis of a gamma-ray celestial source. To correct this, the position of each point in the detector must be transformed into the corresponding one in a displacement plane normal to the incident radiation. Let X,Y,Z be the position of a module in the detector coordinates, and let X', Y' and Z' be their coordinates in the new displacement plane, where Z' has the same direction as the incident radiation, the relation between these quantities can then be obtained by:

$$\begin{cases} X' = [Xcos(\alpha) + Ysin(\alpha)]\cos(\beta) - Zsin(\beta) \\ Y' = Ycos(\alpha) - Xsin(\alpha) \\ Z' = [Xcos(\alpha) + Ysin(\alpha)]sin\beta + Zcos(\beta) \end{cases} \tag{4.4}$$

Where α and β are the azimuthal and zenith angles of the incident direction in relation to the detector surface respectively.

After this correction the non-uniformity correction and the analysis techniques can be employed to obtain the expected result.

4.4.3- Background Noise

Background noise only affects polarimetric measurements as far as the minimum detectable polarization is concerned. This parameter was already explained in section 3.1.6. If well known, the background noise can be greatly reduced. Since in high-energy astronomical measurements, the background is the dominant signal, several techniques have been developed to try to minimize it. These include passive or active shielding of the instruments like collimators or anti-coincidence systems for example as well as trajectory reconstruction of each particle

4.4.4- Pixellation

The tessellation of pixels is another problem that is encountered in pixelated detectors. Their finite size and disposition in the detection surface will deform the $\cos(2\varphi)$ shape of the Q function. An easy way to see this is by taking the 8 pixels around the central one. If they form a ring from which Q is calculated there will be some distortion since the average distance from each pixel to the central one will not be the same. In fact for the diagonal ones this distance will be greater by a factor of $\sqrt{2}$ hence they are expected to have fewer counts than the pixels immediately adjacent to the one in the centre. In the first order ring there will be a large deformation in the $\cos(2\varphi)$ distribution in either squared or triangular pixels, hexagonal ones are the exception due to their increased symmetry. When moving away to higher order rings this deformation will diminish since each pixel will occupy decreasingly smaller angles. It is then usual to decouple these first 8 pixels in order to enhance the resolution.

4.4.5- Full surface irradiation

Due to logistic limitations that will be explored in the next chapter, the present work required full surface irradiation instead of a single pixel irradiation. In this case I implemented two types of corrections. The first one regards the non-uniform response of each pixel and the second one the number of times a particular combination of two pixels can appear in comparison with other combinations. Let us consider a 4x4 matrix such as the one seen in the left side of figure 4.7. This 4x4 matrix corresponds to the one that is used in the experiment at hand.

Notice that this is the first time that irradiation of the full surface is used and where each pixel is used as a scatterer and as a collector. This is an upgrade from previous experiments that focused only one pixel or that, despite focusing a larger area, only used pixels that were not irradiated as collectors. This will be particularly important in a future space mission where the fluxes are low and an increase in sensitive area is important.

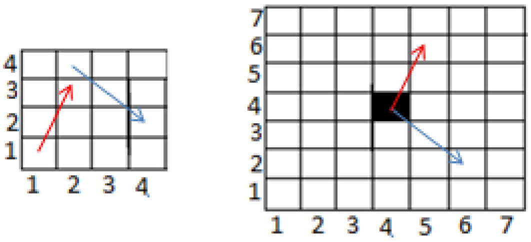

Figure 4.8: Events in a 4x4 matrix reduced to a central pixel in a 7x7 matrix. The black pixel corresponds to the initial interaction and the red and blue lines represent the initial and final pixel of double interactions.

In figure two, reduction to a center pixel of the double events is illustrated. One of this events, represented by the red line, has its first interaction in pixel (1,1) and the second interaction in pixel (2,3) the second one, represented by the blue line, interacts in pixel (2,4) first and in pixel (4,2) second. Given that we irradiate both (1,1) and (2,4) pixels individually in the same conditions, the number of first interactions should differ by a factor that depends on their response. As it was seen earlier in this chapter in section 4.4.1 this can be corrected by multiplying the number of counts obtained by the factor that relates both pixels efficiencies. When the whole matrix is used the reference pixel will be the one with the greatest efficiency. Now considering that the second interaction will interact in any of the other pixels with the same probability (this is not true though) and even after the previous correction, there will still be a difference in the number of counts. This happens once more because each pixel that can host the second interaction has a response that differs from the others. A new correction equal to the previous one, regarding non-uniformity response, must then be applied to our result. Given a response matrix Nc_{ij}, that can be calculated by measuring the number of counts each pixel will have, when subject to radiation individually in the same conditions, then, the true number of counts a particular combination of pixels ij, i’j’ will have can be corrected with the following expression:

$$N_{ij\to i'j'true} = N_{ij\to i'j'}\frac{\left[\max\left(Nc_{ij}\right)\right]^2}{Nc_{i'j'}*Nc_{ij}} \qquad (4.5)$$

Where $\max\left(Nc_{ij}\right)$ is the maximum in the response matrix, $Nc_{i'j'}$ and Nc_{ij} are the values in the response matrix for the two pixels involved and $N_{ij\to i'j'}$ is the number of double interactions that started in pixel ij and ended in i’j’. If for each combination, the initial pixel is now transformed to pixel (4,4) in a 7x7 matrix, the analysis methods studied in section 4.3 can be applied.

There is however another correction that must be made. If one considers again the 4x4 matrix one can see that there are 12 possibilities that the second interaction will occur in the pixel immediately adjacent to the right of the incident pixel and only 1 possibility for the incident photon to travel 3 pixels in a diagonal and still be detected in the matrix. This means that even if the pixels all responded the same way and that all pixel combinations had the same probability the 7x7 counts matrix still would not be uniform but would have more 12 times mores counts in pixel (5,4) than in pixel (7,7) for example. To correct this behavior, the counts matrix can simply be multiplied, element by element, by another matrix whose elements are the maximum number of combination possible amongst all combination possibilities, divided by the number of possibilities a particular combination has. The resulting matrix is as follows:

$$\text{CorrMatrix} = \begin{bmatrix} 12{,}00 & 6{,}00 & 4{,}00 & 3{,}00 & 4{,}00 & 6{,}00 & 12{,}00 \\ 6{,}00 & 3{,}00 & 2{,}00 & 1{,}50 & 2{,}00 & 3{,}00 & 6{,}00 \\ 4{,}00 & 2{,}00 & 1{,}33 & 1{,}00 & 1{,}33 & 2{,}00 & 4{,}00 \\ 3{,}00 & 1{,}50 & 1{,}00 & 0{,}00 & 1{,}00 & 1{,}50 & 3{,}00 \\ 4{,}00 & 2{,}00 & 1{,}33 & 1{,}00 & 1{,}33 & 2{,}00 & 4{,}00 \\ 6{,}00 & 3{,}00 & 2{,}00 & 1{,}50 & 2{,}00 & 3{,}00 & 6{,}00 \\ 12{,}00 & 6{,}00 & 4{,}00 & 3{,}00 & 4{,}00 & 6{,}00 & 12{,}00 \end{bmatrix}$$

The true number of counts in the counts matrix N will then be:

$$N_{true} = N.*\,CorrMatrix \qquad (4.6)$$

.* is the sign for element by element matrix multiplication used in MatLAb. This correction fails for low statistics since it increases significantly the noise/background in the pixels further from the center. Since this experiment fits this low statistics description the correction was not used. Notice however that the polarization measured will always be lower if this is not applied since there are pixels whose full contribution is not considered.

When performing the analysis of the polarimetric measurements in a full irradiated detector one must then use equation 4.5 to correct for non-uniformities and 4.6 to correct for the number of possible combinations.

References

[1] F. Lei, A. J. Dean, and G. L. Hills, “Compton Polarimetry in Gamma-Ray Astronomy”, *Space Science Review*, Vol. 82, p. 309, (1997)

[2] Glenn F. Knoll. Radiation Detection and Measurement 3rd Edition

[3] ''Techniques for Nuclear and Particle Physics Experiments - A How-to Approach'' Second Edition Revised - W. R. Leo

[4] Curado et al, A 3D CZT hard x-ray polarimeter for a balloon-borne payload, Proceedings of the SPIE, Volume 8443, 84434O, 2012

Chapter 5

Experimental Setup

In order to attest the polarimetric performance of a detector one must first be able to produce a polarized beam.

Previous polarimetric experiments were performed at the European Synchrotron Radiation Facility (ESFR) under a polarized gamma-ray beam [1] [2] [3], but despite the unique conditions that this method offers it has one major problem, the beam time at synchrotron accelerators is limited to a few days. For this reason groups interested in further developing their polarimetric techniques in their home laboratories developed non-accelerator polarimetry methods.

From the mechanisms that produce polarized gamma-rays seen in chapter 2, Compton scattering is the one that is most easily achieved in a laboratory. This mechanism allows high degrees of polarization though it never reaches 100%. Since the only source that emits gamma radiation in the 100 keV – 1 MeV range that was available for this study, ^{22}Na, emits 511 keV photons, the maximum polarization possible should be around 66.6% from the scattering of photons by an angle of 90° (value obtained with equation 2.27). The geometry of the experience will resemble the one in [4] and is shown in figure 5.1. Notice that the rays aren't parallel to each other when they emerge from the target. This is due to the low distances that are used. Increased distances would only allow photons parallel to each other to intersect the detector but since the sources available have low activities a compromise was made to have better efficiency.

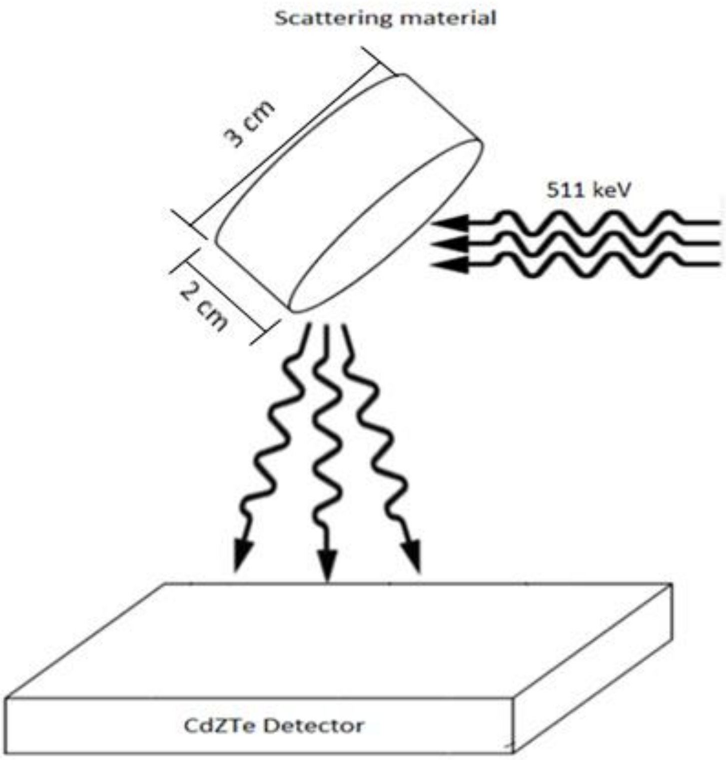

Figure 5.1: Beam polarization simplified geometry. In reality photons leaving the source are not parallel to each other.

It can be seen that there are three main elements composing the experiment, the source, the scattering material inclined by 45° with respect to the incident photons and the detector, and two main phases, the scattering of the incident photons on the scattering material and their detection in the detector volume.

To better understand the results that should be expected and to optimize the experimental parameters two simulations were made one for each phase. For now I will only discuss the simulations for the scattering phase since it’s important for the optimization of the experimental setup. The second phase simulations are presented in the next chapter.

5.1–Scattering Material Analysis

Among the three elements that compose the experiment two are fixed: the detector, a pixelated CdTe semiconductor with pixel dimensions of $2x2x5mm^3$ and a total area proportional to the number of pixels used; the 22Na sources with a combined activity of 18.3 µCi. Regarding the third object, the scattering material, three considerations must be made.

First the material should have high Compton efficiency. This alone suggests a large volume material with a low atomic number Z since otherwise the cross-section for photoelectric effect is considerably increased.

Second the material should be transparent to double interactions in it since this leads to depolarization, which further limits the choice of material to a low Z one.

Finally the material should be shaped in a way that the photons that leave it in the direction of the detector should have a small angle dispersion in order to not pollute the polarization. Unlike the two previous points, here we are led to conclude that a small volume material is more suitable for the experiment. This on the other hand diminishes the materials efficiency which makes the consideration of a higher Z material more attractive.

In [4] a 1cm thick plastic scintillator was used. Since no source activity information was provided in the referred paper that might indicate that a high activity source was employed and that efficiency wasn't a priority for the authors.

Taking into account the previous premises three materials were tested: a plastic scintillator (EJ-200), aluminium and stainless steel. All the scattering material pieces were cylindrically shaped, with 1.5 cm radius and 2 cm thickness.

5.1.1-Implementation

In order to choose the optimal scattering material for the experiment, I developed a custom made Monte-Carlo code that simulated the interaction of photons in the incident beam with the different materials in the programming language C. The “mtwist.h” and “mpi.h” libraries were used to generate pseudo-random numbers and to distribute computation between processors respectively.

Photons were treated in three stages. In the first one its position inside a collimated 7886beam with a radius of 0.5 cm was defined, in the second their course through the scattering material is followed. In the last one, when the photon finally leaves the material, its final position, energy and direction are known making it possible to verify if it intersects the detector. If this intersection occurs the final energy and direction are registered. A flow chart of the process is shown in figure 5.2

Phase one is trivial and only requires that a random distance, r, from the center of the beam and a random angle, Ω, with respect to the y axis to be generated with an uniform distribution:

$$\begin{cases} r = 0.5 * rand \\ \Omega = 2\pi * rand \end{cases} \tag{5.1}$$

Where rand is a random number between 0 and 1.

5.1.1.1 – Photon’s Path in a Scattering Material

To accomplish phase 2, the photon’s path along the target material must be followed. To do so one needs to obtain two parameters between each collision, the distance traveled between the two, λ, and the distance the photon has to travel to reach the target material's surface, d. If the path between collisions is smaller than the distance to the surface, the photon will leave the scattering volume and will proceed to phase three. If this does not happen however, a collision will occur and the mechanics of the photon’s interaction will dictate its’ the final state. Since there is no pair production at this energies only photoelectric effect and Compton scattering can occur. The first one results in a total strip of the particle’s energy terminating its treatment while the second will leave it with energy and direction that can be calculated probabilistically through the differential cross-section formula for Compton scattering found in 2.26 for a non-polarized beam and 2.28 for a polarized one.

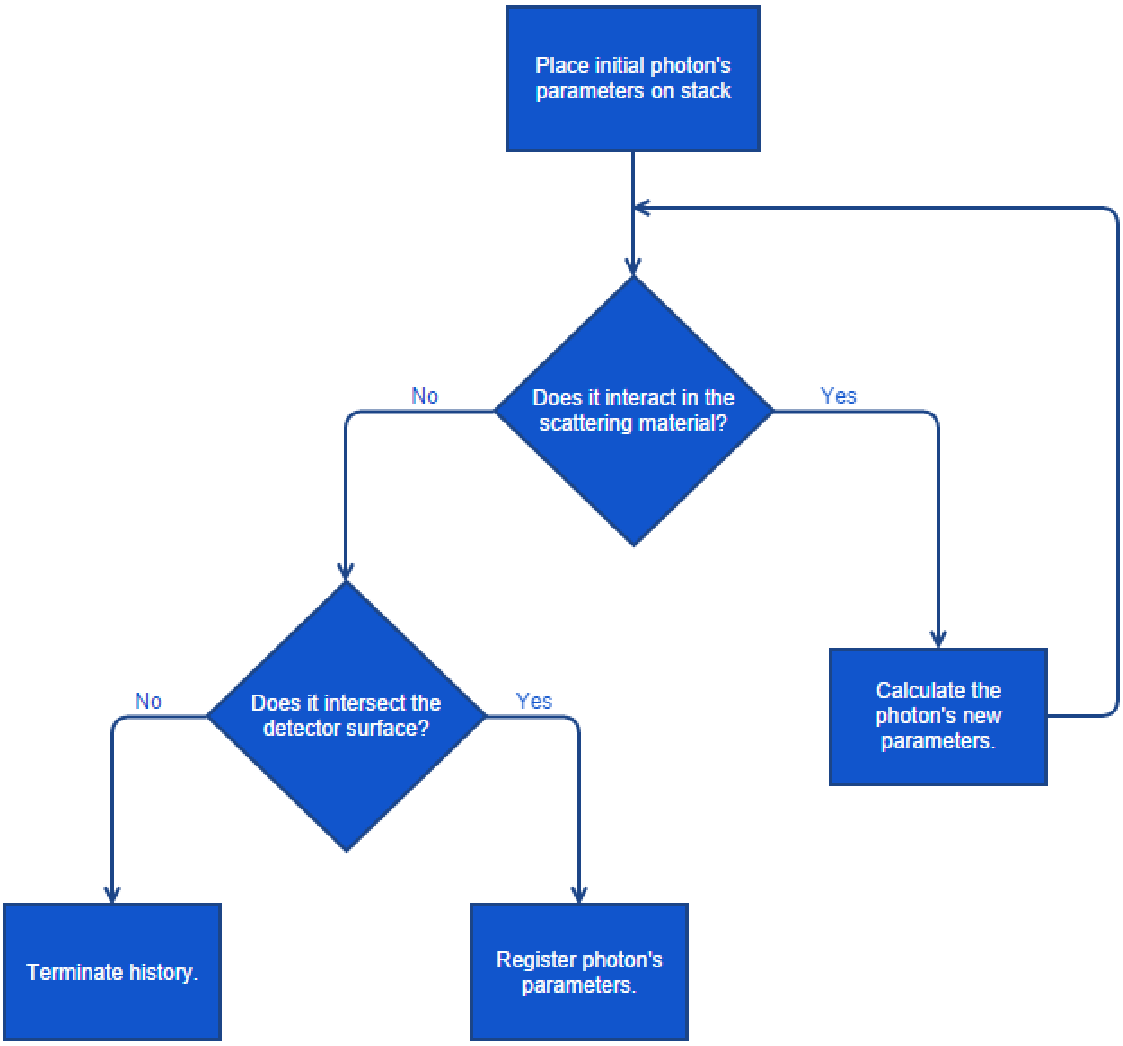

Figure 5.2: Flowchart of the simulation about the polarization of a beam by Compton scattering in a scattering material.

λ can easily be obtained with:

$$\lambda = -\frac{1}{\mu}\log(\mathrm{rand}) \tag{5.2}$$

Where μ is the total attenuation coefficient.

The calculation of d is a little more complex. This is done in the material's reference frame since it makes calculations easier. Let φ be the polar angle of the photon in respect to the x axis in the plane defined by the x and z axis and θ the azimuthal angle in respect to the same axis but in the plane defined by the x and y axis as shown in figure 5.3, then the photon's direction **D** in the target's reference frame is given by:

$$\boldsymbol{D} = \cos\varphi\,\hat{\mathbf{x}} + \sin\varphi\cos\theta\hat{\mathbf{y}} + sin\varphi sin\theta\hat{\mathbf{z}} \tag{5.3}$$

And the parametric equations that rule its motion are:

$$\begin{cases} x = x_0 + tcos\,\varphi \\ y = y_0 + t\,sin\varphi\,cos\,\theta \\ z = z_0 + tsin\varphi\sin\theta \end{cases} \tag{5.4}$$

Knowing that the bases of the cylinder can be found in the planes defined by x=0 and x=h, where h is the thickness of the scattering material, the system solution can now be found:

$$x = 0 \rightarrow t = -\frac{x_0}{cos\,\varphi},\ y = \ y_0 - x_0 tan\varphi cos\theta,\ \ z = \ z_0 - x_0 tan\varphi sin\theta \tag{5.5}$$

$$x = h \rightarrow t = \frac{h - x_0}{cos\,\varphi},\ \ y = \ y_0 + (h - x_0)tan\varphi cos\theta,\ \ z = \ z_0 + (h - x_0)\ tan\varphi sin\theta \tag{5.6}$$

Since the bases have a second boundary condition in:

$$y^2 + z^2 \leq r^2 \tag{5.7}$$

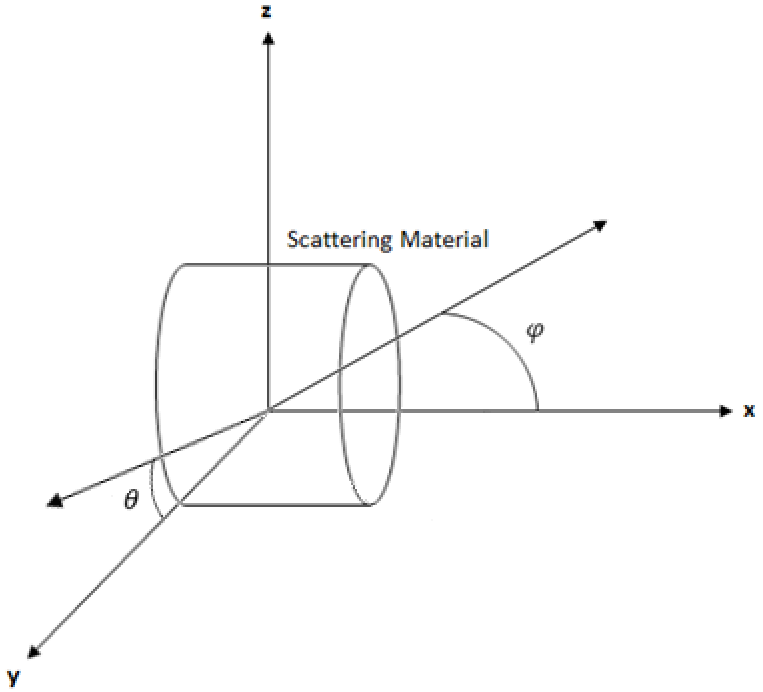

Figure 5.3: Scattering material's reference frame.

By substituting y and z with the coordinates where the photon intersects the plane, one can verify if the photon leaves the material through this volume. If it does the distance between the photon and the bases can be calculated with:

$$d = \sqrt{(x - x_0)^2 + (y - y_0)^2 + (z - z_0)^2} = \begin{cases} x_0^2(1 + \tan^2\varphi), & \text{if x = 0} \\ \left(h - x_0\right)^2 * (1 + \tan^2\varphi), & \text{if x = 2} \end{cases} \tag{5.8}$$

If equation 5.7 is not valid then the intersection must occur in the third surface where:

$$y^2 + z^2 = r^2 \tag{5.9}$$

Substituting 5.9 with the photon’s trajectory equations we obtain:

$$t^2\,(\cos^2\varphi) + 2t\big(y_0 \;\; sin\varphi\sin\theta\, z_0 \;\; sin\varphi\sin\theta\big) + y_0^2 + z_0^2 - r^2 = 0 \tag{5.10}$$

Which is a quadratic equation. Its’ solution is easy to obtain and can be used to calculate the distance to the last surface which is simply the value of t.

With d and λ known it is possible to check if the photon will remain in the detector volume with the condition d> λ.

5.1.1.2 – Intersection with the detector

To find if a photon intersects the detector after leaving the scattering material one has only to find its position in the plane defined by the surface of the detector. Since the photon’s path is completely defined by equations 5.4 one can obtain its’ x and y coordinates when z coincides with the detector’s surface plane.

Let l_x, l_y, l_z be the dimensions of the detector then, the intersection condition, when the centers of both the detector and the scattering material are aligned, will be:

$$\begin{cases} -\frac{l_x}{2} \le x \le \frac{l_x}{2} \\ -\frac{l_y}{2} \le y \le \frac{l_y}{2} \end{cases} \tag{5.11}$$

5.1.2- Results

For this study different number of pixels was used resulting in different areas for the detector surface. The distances used were, 0 cm between the beam and the target since the air’s cross-section is low, and 10 cm between the target’s center and the detector surface. These distances were chosen despite the system being optimized for much larger distances that would force the rays, incident in each object, to be parallel. This is a compromise due to the source’s low activity and the experiment’s low efficiency. The results obtained can be seen in tables 5.1 and 5.2.

Material	Plastic Scintillator	Aluminum	Stainless steel
Compton efficiency in the target (%)	1.49	3.50	13.64
Multiple Interactions (%)	0.066	0.34	0.34

Table 5.1: Results of the polarization of a beam scattered in different materials. The multiple interactions % refers to the incident photons that interacted more than once in the scattering volume.

Material	Plastic Scintillator			Aluminium			Stainless Steel		
Detector Area (# of pixels)	1x1	4x4	11x11	1x1	4x4	11x11	1x1	4x4	11x11
% of photons that intersects the detector (10^{-2})	0.0054	0.13	1.1	0.016	0.32	2.6	0.067	1.1	9.0
% of photons with multiple interactions that intersect the detector (10^{-2})	0.0004	0.006	0.054	0.0014	0.030	0.26	0.19	0.25	1.9
Average Energy (keV)	256.56	255.18	255.25	254.24	253.33	253.36	251.91	251.85	251.83
Average Polarization (%)	66.29	65.87	65.43	66.05	65.68	65.17	65.60	65.25	64.89

Table 5.2: Efficiency, average energy and average polarization of photon beams generated by different scattering materials.

These results have shown that the efficiency of this setup is very low with only 0.09% of the photons intersecting the detector at best. The efficiency increases with the detector area and with the atomic number of the scattering material as expected. One can also observe that the average energy decreases as the atomic number increases. This can be explained by the increase in multiple interactions that reach the detector since these lose more energy than particles that are scattered only once by the same total angle. A decrease in the polarization is also observed with the increase in atomic number as well as with the area of the detector which was expected due to the nature of Compton scattering. An interesting case is the one of the plastic scintillator. In it we see that the decrease in detector area leads to an average polarization that is almost equal to the one when there is no dispersion from the 90° interaction. This is due to the almost null existence of double interactions and to the small area of the 1x1 matrix.

For reasons that shall be discussed later on this chapter, the area of the detector is limited to a 4x4 matrix and as such the results for this area are the ones of interest. With this in mind it, and considering only the efficiency, stainless steel seems to be the best material. There is a problem however, with the increase in atomic number, from the plastic scintillator to aluminium and to stainless steel, the percentage of photons that suffer multiple interactions in the scattering material and still reaches the detector also increases. Despite the average energy and polarization not changing much, aluminium was chosen in order to find a middle ground between efficiency and the energy band since broader energy bands would also increase the noise/background contributions.

5.2–POLCA II

Now that the polarization beam concept has been analysed it is time to focus on the detector and all the components that it requires. A representation of all the subsystems can be seen in figure 5.4. Originally these subsystems were not made to operate together. In fact, while the detector and the front-end electronics are the ones used in [2] and [3], the TAKES unit was the one used in [1]. Ultimately there are some incompatibilities between the systems such as the number of channels read by the TAKES uniform being inferior by a factor of 8 in relation to the number of pixels whose information goes through the front-end electronics.

Each part of the system will now be presented with some more detail before discussing the adaptations that were done.

5.2.1 - CZT detector and the Front-End Electronics

The detector is composed of a 16x16 CZT pixel arrays fabricated by IMARAD. Each pixel dimensions of area of 2 mmx2mm and 5mm thickness with an interpixel gap of 0.5mm. The anode part is then connected to the front-end electronics through 3 connectors J1, J2 and J3 with pin gaps of 0.5mm to coincide with the pixel gap. Since the front-end electronics only reads 128 pixels and there are 256 distributed between the 3 connectors only two of these were actually connected. The choice was made so that an 11x11 matrix could be constructed. The destination of these connectors were 8, 16 channel, eV Application Specific Integrated Circuits (ASICs) each processing analogically 16 CZT pixels [2]. The pixels that each ASIC reads re displayed in figure 5.5.

Each ASIC can be connected with TAKES via a 37 pin cable. Before connection however an inversion has been done. The association between the output in the ASICs channels and the input in the TAKES unit can be seen in figure 5.6.

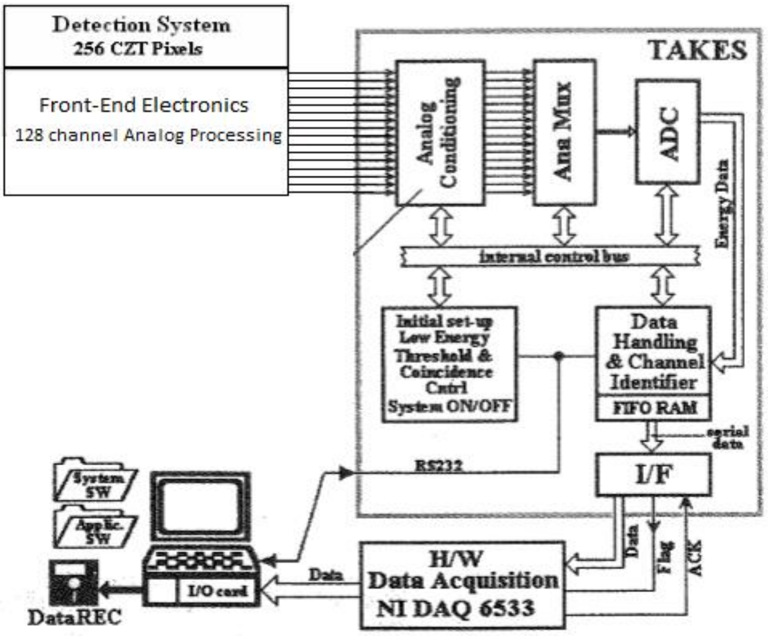

Figure 5.4: Schematics for the CZT detector and all its' components [1] [2]. In it is possible to see the 3 main components, the 256 CZT pixel detector connected to the front-end electronics, the TAKES unit that treats the signals generated in the detector and finally the Data Acquisition Control and Quick Look S/W that finalizes the signal treatment and displays the information.

	85	86	87	88	89	90	91	92	93	94	95
100	101	102	103	104	105	106	107	108	109	110	111
116	117	118	119	120	121	122	123	124	125	126	127
132	133	134	135	136	137	138	139	140	141	142	143
148	149	150	151	152	153	154	155	156	157	158	159
164	165	166	167	168	169	170	171	172	173	174	175
180	181	182	183	184	185	186	187	188	189	190	191
	197	198	199	200	201	202	203	204	205	206	207
	213	214	215	216	217	218	219	220	221	222	223
	229	230	231	232	233	234	235	236	237	238	239
244	245	246	247	248	249	250	251	252	253	254	255

Figure 5.5: Pixel association with the 8 ASIC channels. Pixel numbers start at 85 because not all the matrix is being used.

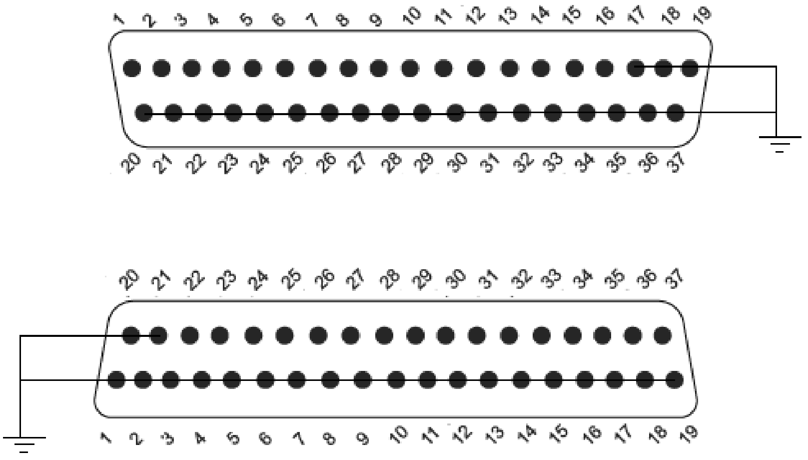

Figure 5.6: The top figure shows the output channels of the ASIC channels. Pins from 1 to 16 correspond to pixels in the detector that depend on the ASIC channel. The other 11 pins are connected to the ground. The bottom figure shows the input of each channel in the TAKES unit. After the inversion pins 1 through 21 are connected to ground while the others connect pixels to the TAKES. The association between both is linear, pin 1 in the ASIC connects to pin 37 in TAKES, pin 2 to 36 and so on.

5.2.2-TAKES

The TAKES unit available for this work was designed for the detector used in [1] that only had 16 pixels instead of the POLCA II used here. As such there is great difference since its design only allows the reading of one ASIC channel at a time.

TAKES allows an energy threshold to be set and performs coincidence logic by opening a pre-determined time window (set to $2\mu s$ in the experiments) and coding interactions that arrive from different pixels in it as multiple events. Other features include analog-to-digital conversion and coding of events as a 20 bit words. These 20 bits include 10 for the energy of the event, 1 for the overflow possibility, 1 for the multiple event condition and 4 to the pixel channel as shown in figure 5.7 [1].

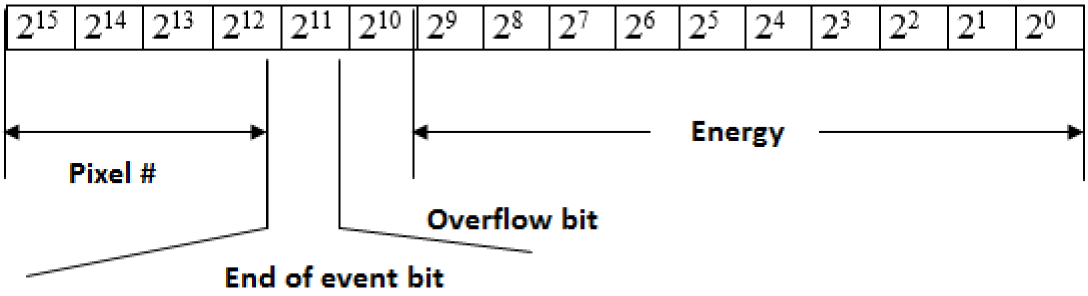

Figure 5.7: Meaning of the 16 bit words. The end of event bit is only one for the last interaction in a multiple event [1]. The TAKES outputs data in a serial form.

The information correspond to each pixel goes through different channel in the TAKES electronics. Each of these channels has an amplifier with an adjustable gain between 0.5 and 1.5. The variation in the gain between each one and the fact that the amplifiers were inaccessible caused some problems in the energy calibration as it will be discussed in the next chapter.

5.2.3-Data Acquisition Control and Quick Look S/W

At this point the system is connected to a PC with a quick-look and storage S/W developed in LabView. Its primary functions are to control, store and reproduce the data the data sent from TAKES.

5.2.3.1- Acquisition Control

The control function ranges from simple tasks such as setting a time or even a count limit to more complex ones like the de-codification and filtering of the serial information received from TAKES. In fact, since the address associated by TAKES to any input does not correspond to the real pixel number, it is up to the software to translate this information. The interface associated with this function can be seen in figure 5.8 and includes the option to designate the number of the ASIC used (this is one of the adaptations discussed in the next section), the utilization or not of the Lookup table that converts the pixel number outputted by the TAKES unit, a time/count limit for the acquisition, the number of connected pixels and the total number of pixels in the detector. All these selections, except the limit one, will determine the pixel number conversion.

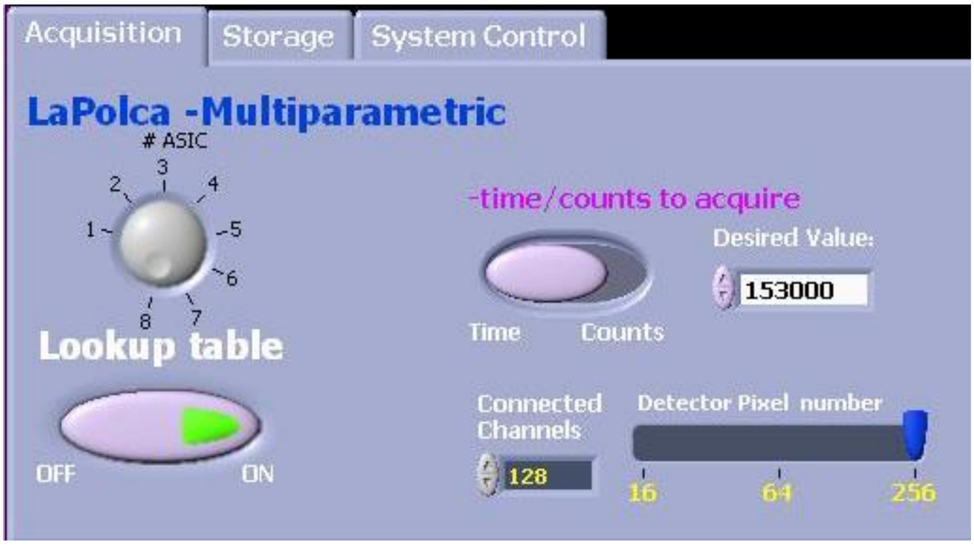

Desired Value: 153000

Connected Channels 128

Figure 5.8: Acquisition interface. In this tab of the software selection options regarding the ASIC channel used (top left nob), the use of a lookup table for pixel number conversion (bottom left switch), limitation of the acquisition duration regarding either time or the number of counts (top right) and the number of pixels connected and existent in the detector.

5.2.3.2- Storage

As far as the storing function is concerned only a few considerations must be done. The first one is that each word has the same shape as the one shown in figure 5.7 but with 8 bits for the pixel number. Words associated with each event will be placed in a queue and then written in a file sequentially into 1024 words lines. This can be done in either ASCII or binary according to the selection made in the interface. The interface also allows choosing a file name, suffix and comments as show in figure 5.9.

In the case of multiple events the storage is more complex. In this case only the last interaction to be written has the value 1 in the end-of-event bit. This means that the interaction, whose word is left to this one, has been caused by the same photon. However one cannot be certain about which one of them was the first and the second interaction since the electronics cannot process it. In polarimetry this is not a problem since there is 180° symmetry in the double interaction maps. In the considered energy range this can be solved nevertheless by the nature of Compton scattering. Simple calculations shows that for energies below ~260 keV the first interaction should deposit less energy in the detector volume [4]. To be even more accurate one can assume that the second interaction is by photoelectric effect and that the whole remaining energy is deposited. This means that from the energies of the two interactions it can be known which one occurred first, the lower energy one. The 180° symmetry also allows to choose randomly which one was the first interaction. In rarer cases there can also be a triple interaction event but this will not be considered due to its low probability.

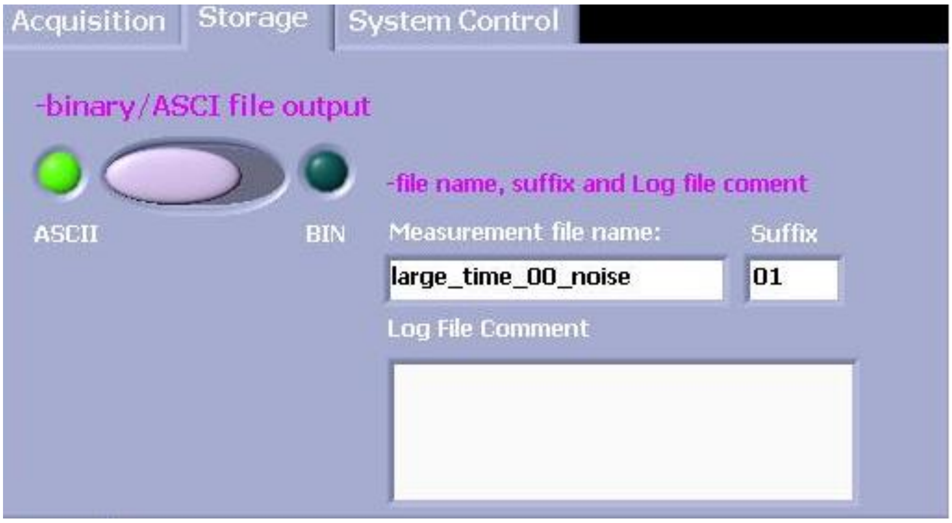

Measurement file name: large_time_00_noise

Suffix: 01

Figure 5.9: Storage interface of the LabView S/W. It includes a switch in top left side that dictates the data type of the stored information and three text boxes where the name of the file, suffix and comments can be inserted.

5.2.3.3- Data Reproduction

In the last tab the interface shows most information from the interactions that occur in the detector in real time. Figure 5.10 shows the full interface.

In the top left there is a panel that concerns the system control. It allows switching between two modes, the “Test” and “Measure” whose only difference is the storage of the information. The panel also has two buttons to Start and Stop the acquisition, a bar that goes from 0 to 100 according to the information rate that is reaching the software, colour coding for this same information, a count that shows the number of words so far, the elapsed time of the acquisition, the number of counts/s and the mean pixel counts/s.

Below this panel there is one entitled “Pixel Map”, it shows the full pixel matrix through an intensity map that regards the number of counts in each pixel. There is also an option to make this map with logarithm form. Selecting a pixel with the green dot reveals information about in the adjacent panel. Information about its number, number of counts/s can be visualized here along with others that are no so important.

In the top right side of the interface we have the energy spectrum of the selected pixel. Energy channels go from 0 to 1023 since the coding of the energy only has 10 bits. There is also a logarithm option and information regarding a region of interest (ROI) that can be selected with the blue and yellow lines. This information includes the total number of counts, the weighted centroid, the centroid count, the variation of channels and the number of counts in the peak.

5.2.4- System Adaptations

Due to the limitations in electronics, specifically because the TAKES unit reads only an eighth of the detector pixels, some adaptations were done to the system. These changes can be separated in two groups, physical modifications concerning the hardware and software updates.

5.2.4.1- Physical Modifications

The main modification to the system concerned the connection between the FE electronics and the TAKES unit. Due to the TAKES design only an ASIC channel could be connected at a given time. This would leave the coincidence logic system obsolete since it would only work between pixels of the same ASIC. An alternative could be the collimation of the beam emergent from the scattering material onto a single pixel and read the other ones for equal amounts of time. This collimation would mean that interactions in pixels that were not the focused one could only come from the scattering of photons in it. However due to the energies that were used and the available equipment this was not a possibility. Since the geometry of the pixels in each ASIC channel is not a good one for polarimetry the active matrix was reconstructed. The method used consisted in selecting pins at the end of the ASIC output cable. Each of these pins is connected to a single pixel. Selecting pins from different ASIC channels and connecting then to each of the TAKES 16 channels permitted a 4x4 squared matrix to be constructed. Taking into account that the number of ASICs and electronic noise should be kept as low as possible the best region found region was the one delimitated by pixels 183, 186, 231 and 234.

Another important issue was the use of 10kΩ resistances between the ASICS and the TAKES. This was value for the resistance was high enough so that the energy range used did not saturate the system but was low enough so that the lower energies could still be read.

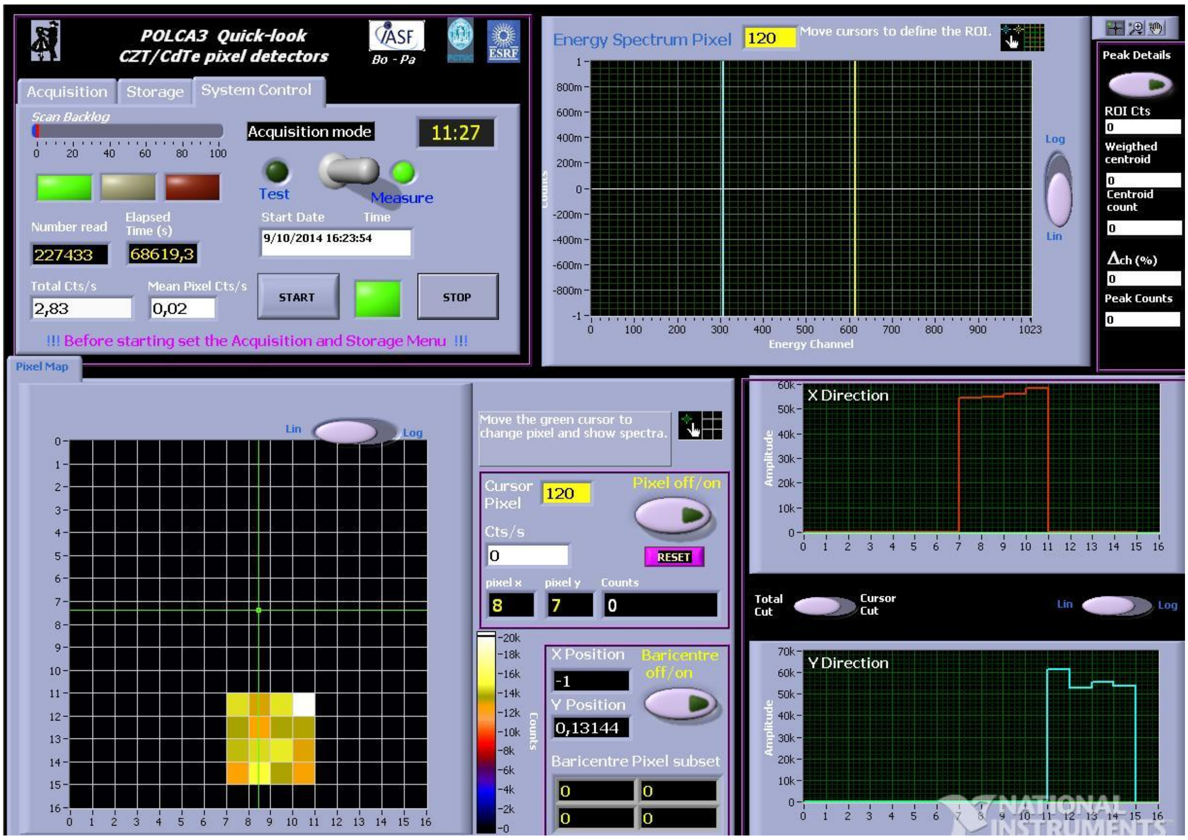

Acquisition mode: 11:27

Start Date Time: 9/10/2014 16:23:54

Number read: 227433

Elapsed Time (s): 68619,3

Total Cts/s: 2,83

Mean Pixel Cts/s: 0,02

Energy Spectrum Pixel: 120

ROI Cts: 0

Weigthed centroid: 0

Centroid count: 0

Δch (%): 0

Peak Counts: 0

Cursor Pixel: 120

Cts/s: 0

pixel x: 8

pixel y: 7

Counts: 0

X Position: -1

Y Position: 0,13144

Baricentre Pixel subset: 0 0 0 0

Figure 5.10: Full interface of the LabView S/W.

5.2.4.2- Software Modifications

The 16 channel TAKES unit had a hazardous effect not only in electronics but also in the software component. In fact the software available was the one developed for the TAKES 128 channel counterpart making it obsolete when converting pixel number information since it always reads the same 16 pixels associated with channel 8. This occurred because the conversion was made through the loading of a text file, with the pixel numbers ordered in a way that corresponded to the output of the 128 channel TAKES units, into an array. Since this unit only has 4 bits available for the coding of the pixel number this meant that it was blind to the ASIC change and that it always returned values from 0 to 15. To solve this problem the array with the pixel order had its elements interchanged so that the first 16 elements corresponded to the connected ASIC. In a later stage, when the matrix read was hand-picked to form a 4x4 square, the pixel number in the file were simply changed to correspond to those chosen. Figure 5.11 shows algorithm of the process.

Another problematic feature came with the energy threshold. Since the amplifiers in the TAKES unit were not calibrated with each pixel, and since changing the ASIC would ruin any previous calibration done, ultimately the threshold was setup on different levels for each pixel. Since these amplifiers were out of reach a software tool was implemented. This tool did not take into account the energy calibration corrections but permitted that energies below a certain level were set to zero independently of the pixel.

```
-Load array
      Array = [- - - - - -|- - - - - - -|- - - - - -|- - - - - -|- - - - - -|- - - - - -|- - - - - -|- - - - - -|
                 ASIC #8      ASIC #7      ASIC #6     ASIC #5     ASIC #4     ASIC #3     ASIC #2     ASIC #1
-Choose ASIC #
      ASIC=8-ASIC#

-For i=1:16
      Array[i]↔Array[16*ASIC+i]
```

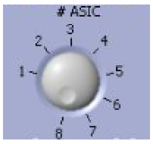

Figure 5.11: Algorithm used to change the ASIC channel to read.

The last update done was the introduction of a number of peak counts display. The calculation of this number consisted in choosing a ROI close to the peak's maximum, the software would then look at the adjacent energy levels and the ones after that until to levels had half the number of counts than the maximum. A standard deviation would then be calculated as well as the number of counts in the channels that were inside a 3 standard deviation window. This allowed performing the uniformity tests without taking into account the electronics noise.

The analysis of the simulations and the adaptations of the system permitted to prefect the experimental setup. There was a problem however with the connection of systems that were not designed to work together. This introduced some noise in the detector that was not removed successfully since the shielding of the components was not prepared for this conditions. The analysis also revealed that each measurement requires a large acquisition time.

In the next chapter the polarimetry measurements are discussed. This includes the simulations and the experimental work that included the uniformity tests and the calibration of the system will be discussed as well as the results featured in them. Lastly the results for the polarized beam as well as some unexpected sources of error and their solution will be analyzed.

References

[1] G. Ventura, E. Caroli, N. Auricchio, A. Donati, G. Landini, F. Schiavone, R. M. Curado da Silva, POLCA: experimental set-up, calibration procedures and results, Internal Report IASF/BO n. 352/2002 (September 2002)

[2] G. Ventura, E. Caroli, N. Auricchio, A. Donati, G. Landini, F. Schiavone, R. M. Curado da Silva, POLCA2 (POLarimetry with CZT Arrays): experimental set-up, calibration procedures and results, CZT-IASF-BO-004.

[3] E. Caroli, A. Donati, G. Landini, F. Shiavone, J. B. Stephen, G. Ventura, R. M. Curado da Silva, S. Sordo, N. Auricchio, A. Pisa, V. Honkimaki, LAPOLCA: USER MANUAL FOR ESRF 2008 TESTS, CZT-IASF-BO-007

[4] R.A. Kroeger et al., "Spectroscopy, Imaging and Compton-scatter Polarimetry with a Germanium Strip Detector", IEEE Transactions on Nuclear Science 07/1996

[5] Curado et al, A 3D CZT hard x-ray polarimeter for a balloon-borne payload, Proceedings of the SPIE, Volume 8443, 84434O, 2012

Chapter 6

Polarimetry Results

Now that the system was set up we are in conditions to perform polarimetric measurements. Before the experimental work however, simulations were done with the GEANT4 library. The results from these simulations were used to improve the analysis techniques as well as a reference for the experimental results.

6.1 – Polarimetry with GEANT4

To further study the expected results, simulations of a polarized beam incident in a CdTe detector were made with the GEANT4 library (version 4.9.4) using a modified PolarizedCompton() function that corrected previous problems. The detector considered was a 7x7 pixelated CdTe matrix with pixel dimensions as those mentioned in 5.1. The 7x7 matrix results from a technique employed on 4x4 matrix, when each first photon's interaction in any of the detector pixels is assumed to occur in a central pixel of a 7x7 matrix. When irradiating with a polarized beam the full surface of a 4x4 matrix, in order to analyze the full double events occurring in the matrix, it is better to reduce each double event (photons that first undergo a Compton interaction with the material and then are absorbed with a second interaction) first interaction to a virtual central pixel than irradiate only one central pixel of a 4x4 matrix, since it would generate a poor double event distribution around the irradiated pixel.

Simulations were made irradiating the central pixel of the matrix with a beam of 10^6 photons with 260 keV for different degrees and angles of polarization. Results for the same angle are analyzed simultaneous. This choice of energy came from the expected beam energy that leaves the scattering material and reaches the detector. The response of the detector to a non-polarized beam was made first to check for a residual N(θ) distribution subtracting it later to the distributions of polarized beams. Since the library only allows 0 and 100% polarized beams the result of a polarized beam and an unpolarized one were superposed to simulate intermediate degrees of polarization. On the other hand the polarization vector can be defined allowing different polarization angles.

6.1.1-Unpolarized Beam

The next two figures show the double interaction matrix and the N(θ) distribution. In the double interaction matrix one can observe a uniform distribution with very small variations. In the other the fluctuations from bin to bin can be observed with more detail (these bins are the 24 15° regions of the matrix that are used in the mask). In figure 6.2 one can see that there is a small fluctuation between bins (each dot corresponds to one) from the expected value 0.0833. The modulation is then different from zero due to the squared tessellation of the matrix and the fluctuations from uniformity must be subtracted in the distributions of polarized beams.

The uncertainty associated with each value is obtained using the standard deviation resulting from Poisson statistics.

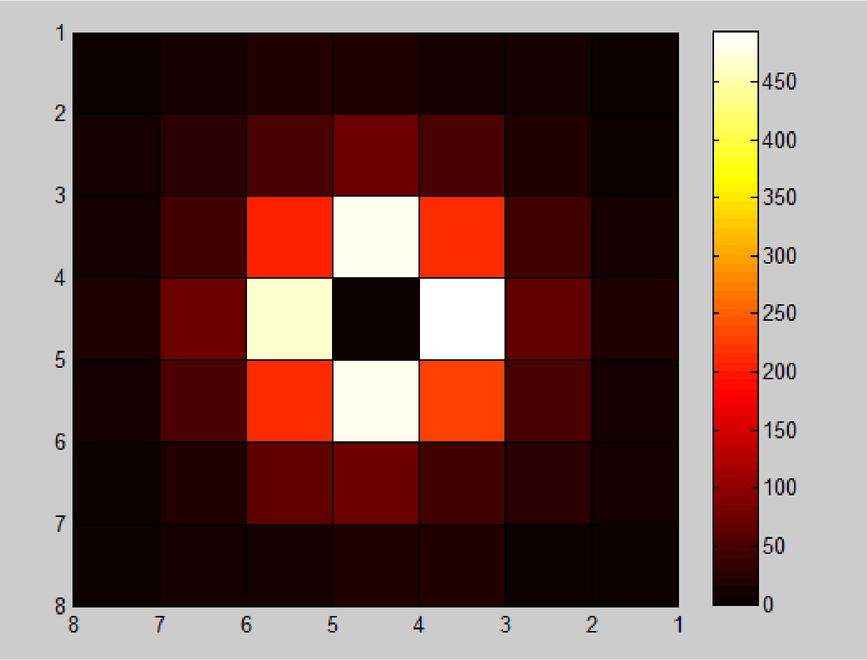

Figure 6.1: Double interaction matrix for an unpolarized beam. The number of interactions increases from black to white.

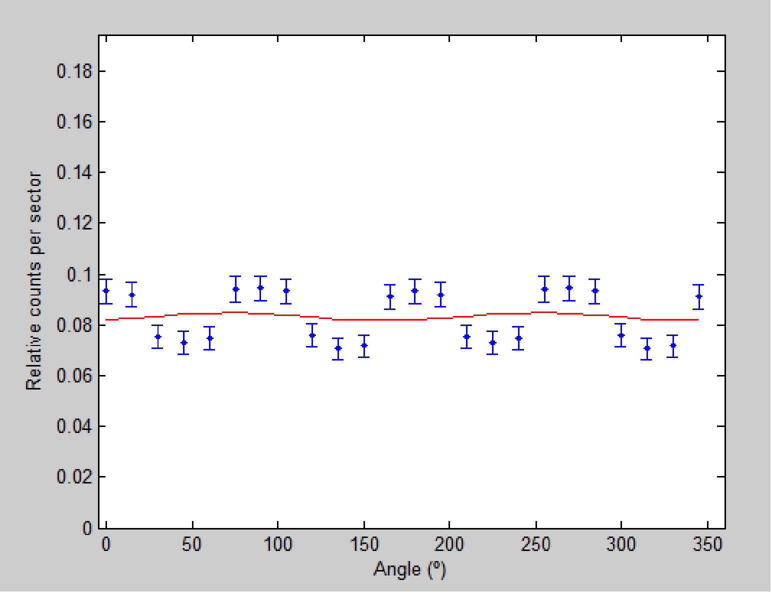

Figure 6.2: N(θ) distribution. The red line is the fitted function. The fit is obtained with the MATLAB "fit" function. This function uses the least squares method to fit the data to a model function, in this case a $Acos(2\theta+\varphi)+C$ where A, φ and C are the coefficients to be calculated and θ is the azimuthal angle. Notice that a $Acos(4\theta+\varphi)+C$ would fit better due to the 90º symmetry of the matrix.

6.1.2- Angle of Polarization at 0 Degrees

The results obtained for a beam with its polarization angle at 0° degrees with respect to the horizontal axis are presented in table 6.1. Figure 6.3, 6.5 and 6.6 show the double interaction map, the N(θ) and the Q(θ) distribution for a 100% polarized beam with its angle of polarization at 0°. The double interaction matrixes and the N(θ) distribution obtained for other degrees of polarization at this and other angles can be found in Annex B.

The double interaction matrix, unlike the one for an unpolarized beam, clearly shows an asymmetry in the direction of the scattered photons. For the horizontal and vertical axis this asymmetry is more prominent with the latter having a higher intensity. This asymmetry is the one expected from a polarized beam and allows us to measure the polarization of a beam.

Figure 6.4 shows the relative number of photons that were scattered to each bin. Here the difference is not residual as in the previous case but follows a well-defined cos(2θ) function. This can also be seen in figure 6.5 that follows a function with the same shape. The minimum in both figures corresponds to the polarization angle, φ=0.7±0.6 and the maximum value in figure 6.5, 0.439±0.005, is the modulation factor for a 100% polarized beam, Q_{100}. This value is in good agreement with the ones obtained in other studies [1]. The error in this case is the one calculated by the MATLAB "fit" function and has a 2σ confidence level.

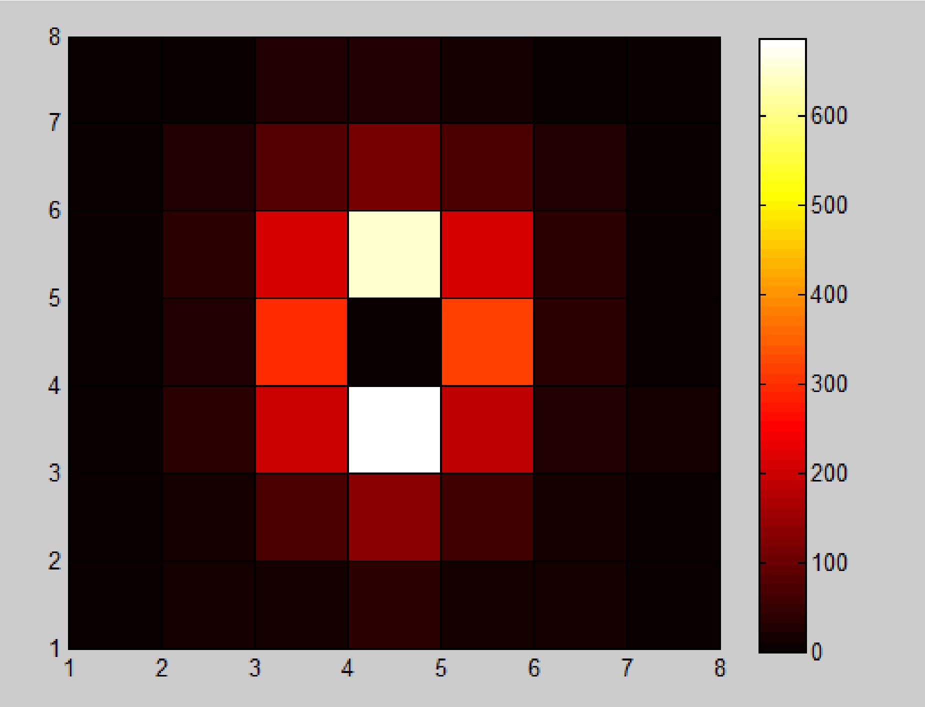

Figure 6.3: Double interaction matrix for a 100% polarized beam with its angle of polarization at 0°. The number of interactions increases from black to white.

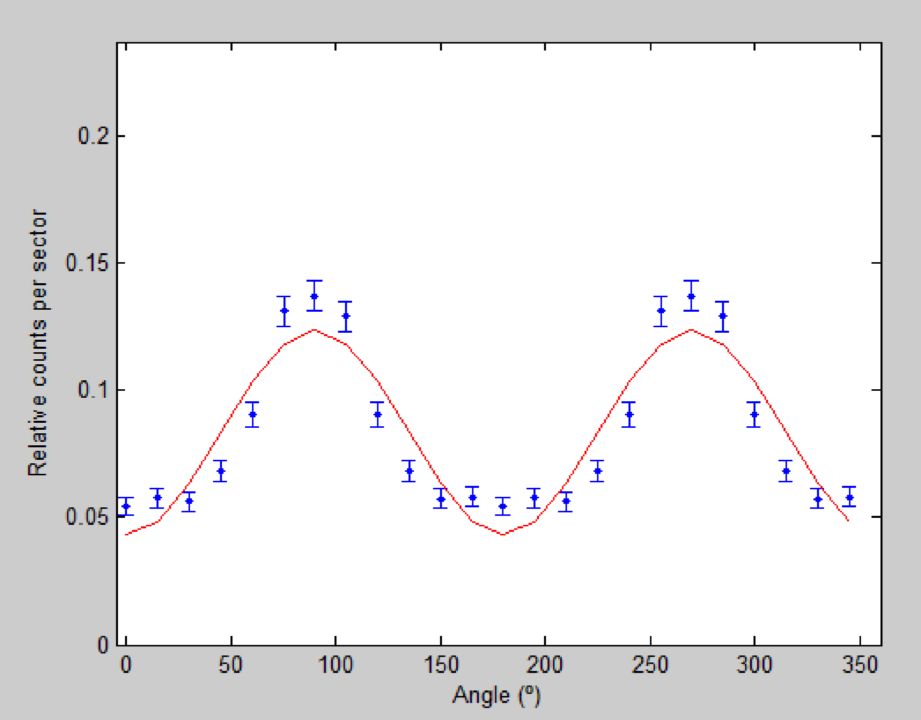

Figure 6.4: N(θ) distribution for a 100% polarized beam with its angle of polarization at 0°. The red line is the fitted function. The equation of this function its presence is merely representative.

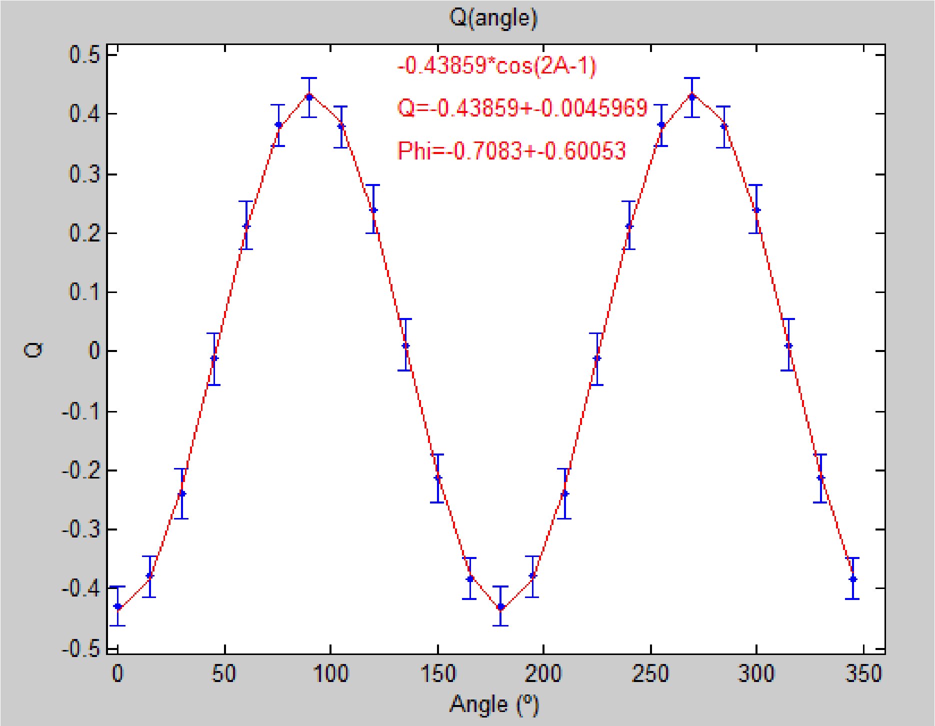

Figure 6.5: Q(θ) distribution for a 100% polarized beam with its angle of polarization at 0° fitted to a cos(2θ) form. The red line is the fitted function.

The degree of polarization measured for other beams was also in the parameters expected, following a linear correlation as it can be seen in figure 6.6, with the highest difference between the measured and the expected one being under 3.28%. The measured angles for each degree was also according to the expected one, 0°, with the maximum difference found being equal to 4.3°, well under the bin size (15°). The main factors that lead to the discrepancies are the shape of the pixels and the mask used in the analysis.

Expected Degree (%)	Measured Q	Measured Angle (°)	Measured Degree of Polarization (%)
100	0.439±0.005	0.7±0.6	100.00
80	0.359±0.004	0.4±0.7	81.78±1.30
60	0.271±0.005	-1.0±1.0	61.53±1.34
40	0.190±0.006	-2.9±1.9	43.28±1.45
20	0.108±0.004	4.3±2.1	24.60±0.95

Table 6.1: Results for the simulations with polarization at a 0 degree angle with the horizontal axis.

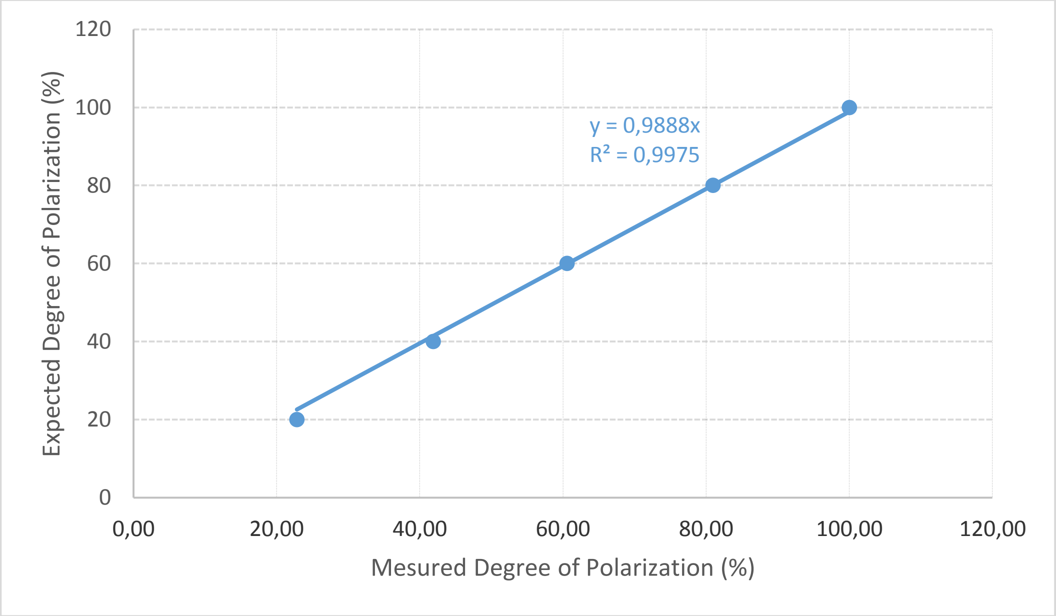

Figure 6.6: Measured vs Expected degree of polarization of a simulation with a beam at 0 degree angle with the horizontal axis.

6.1.3- Angle of Polarization at 45 degrees

The results of the simulations of polarized beams with their angle of polarization at 45° are presented in table 6.2. The value calculated of Q_{100} was 0.466±0.062 higher than that of the previous case. This difference is due to the finite size of the bins and was discussed was in chapter 4 when the different analysis techniques were analyzed. The measure degrees of polarization once again followed a linear shape (see figure 6.8) as expected with the maximum difference 7.21%. This is something easily explainable as it was said in the previous case.

The measured angle of polarization was between 39.5±8.4° and 44.6±7.6° still within the expected angles. Figure 6.7 shows the linearity expected. This also within the values expected from the use of the current mask.

Expected Degree (%)	Measured Q	Measured Angle (°)	Measured Degree (%)
100	0.466±0.062	44.6±7.6	100.00
80	0.381±0.050	41.9±7.6	81.76±1.28
60	0.294±0.039	41.6±7.7	63.09±1.85
40	0.206±0.037	41.54±9.6	44.21±1.12
20	0.107±0.016	39.5±8.4	22.96±1.60

Table 6.2: Results for the simulations with polarization at a 45 degree angle with the horizontal axis.

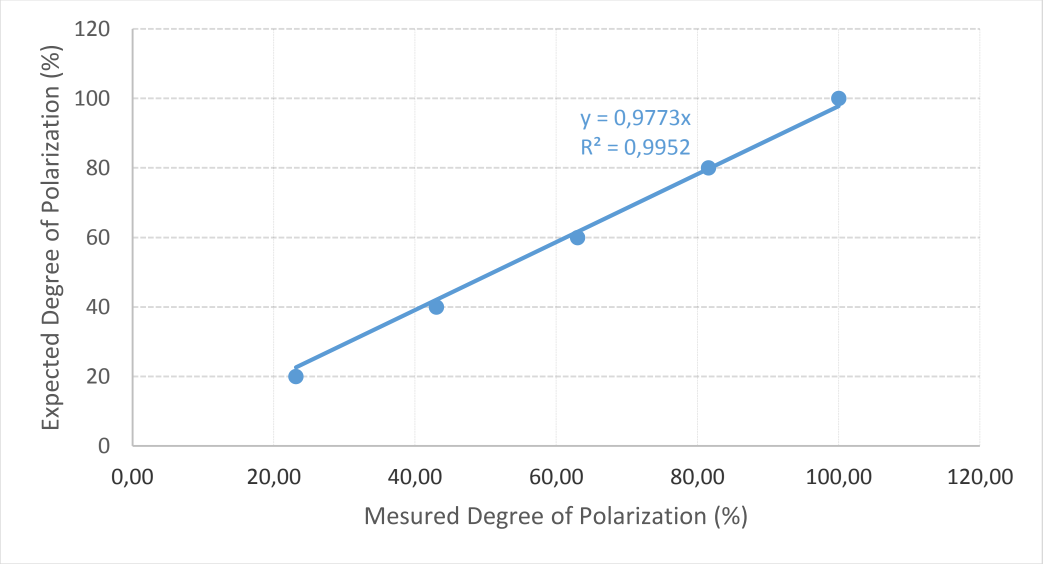

Figure 6.7: Measured vs Expected degree of polarization of a simulation with a beam at a 45 degree angle with the horizontal axis.

6.1.4-Angle of polarization at 90 degrees

The results of the simulations of polarized beams with their angle of polarization at 90° are presented in table 6.3. The calculated value for the Q_{100} was 0. 0.421±0.004, once again in good agreement with what was expected. Notice that this value is very close to the one obtained in the 100% polarized beam at 0°. This is due to the symmetry there is between the two cases. Both polarization angles see the matrix tessellation in the same way hence the similar result. The measured degrees of polarization once again followed a linear shape (see figure 6.8) as expected with a maximum difference 1.62%.

The values obtained for the angle of polarization are very good differing from the expected value by less than 0.5°.

Expected Degree (%)	Measured Q	Measured Angle (°)	Measured Degree (%)
100	0.421±0.004	89.7±0.5	100.00
80	0.336±0.003	89.9±0.5	79.81±1.19
60	0.252±0.003	89.8±0.7	59.86±0.91
40	0.168±0.004	89.84±0.5	39.90±1.02
20	0.0774±0.003	89.6±2.4	18.38±0.73

Table 6.3: Results for the simulations with polarization at a 90 degree angle with the horizontal axis.

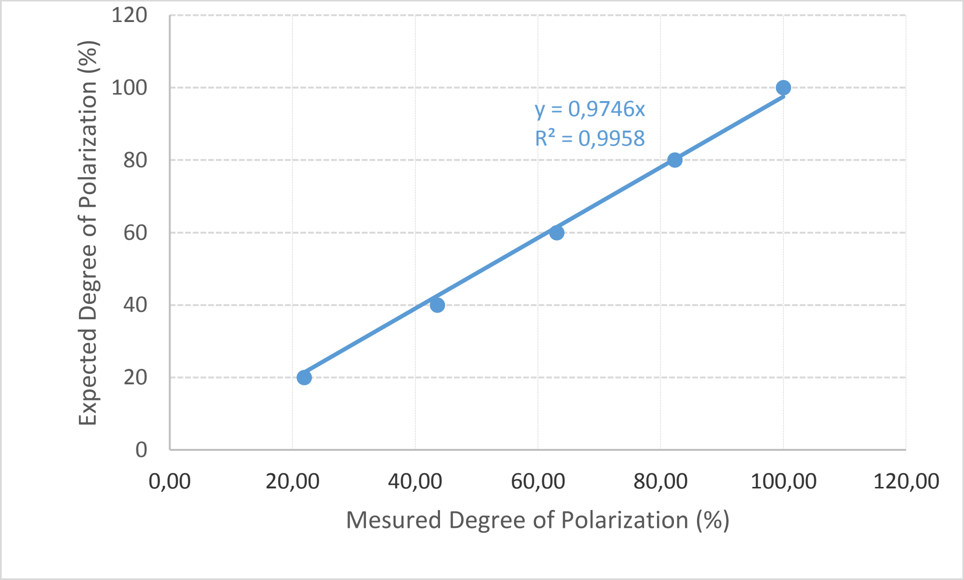

Figure 6.8: Measured vs Expected degree of polarization of a simulation with a beam at a 90 degree angle with the horizontal axis.

6.1.5- Angle of Polarization at 135 degrees

Lastly the results of the simulations of polarized beams with their angle of polarization at 135 are presented in table 6.4. The calculated value of Q_{100} was 0.447±0.054, once again in good agreement with what was expected. This value is intermediate when compared to the other three calculated. The similarity that was found between the beams with polarization at 0 and 90° is not found between this beam and the one with polarization at 45°. This is caused by the low number of photons that had double interactions in the detector. The measured degrees of polarization once again followed a linear shape (see figure 6.9) as expected with a maximum difference between the measured values and the expected of 3.62%.

The values obtained for the angle of polarization are very good with all the values differing from the expected by less than 3°.

Expected Degree (%)	Measured Q	Measured Angle (°)	Measured Degree (%)
100	0.447±0.054	135.32±6.96	100.00
80	0.368±0.045	135.5±7.0	82.33±14.15
60	0.282±0.034	135.8±7.0	63.09±10.78
40	0.195±0.024	135.8±7.1	43.62±7.52
20	0.098±0.012	137.74±6.9	21.92±3.77

Table 6.4: Results for the simulations with polarization at a 135 degree angle with the horizontal axis.

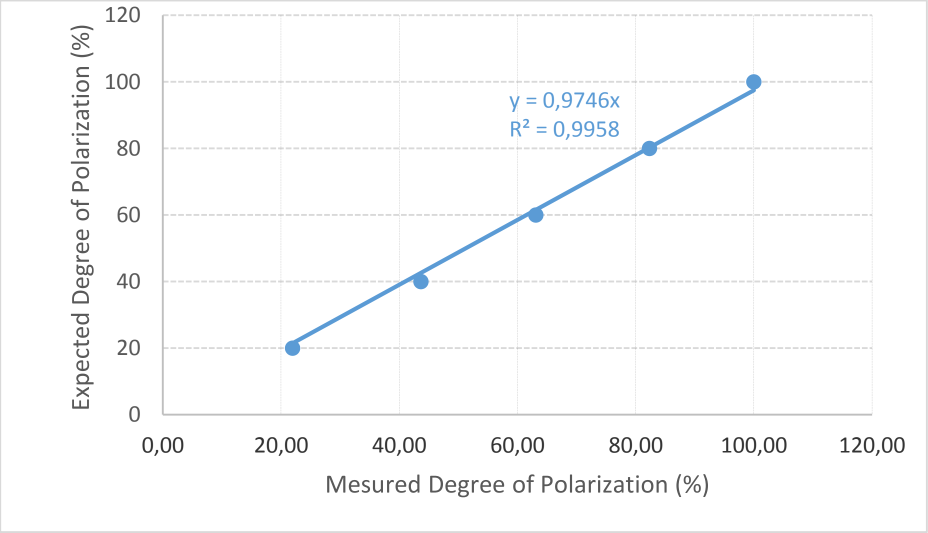

Figure 6.9: Measured vs Expected degree of polarization of a simulation with a beam at a 135 degree angle with the horizontal axis.

This simulations showed that the method for calculating the modulation factor and the angle of polarization are ready to be used in the experimental work far from the ideal situation that the simulations presented. It can be seen that the Q_{100} is in average 0.443±0.031. This value should be over the experimental one since the pixel pitch and hence the pixel geometry is different and because experiment provides complications such as background and dispersion in energies and incident angles. In terms of the angle there is no reason that would lead one to conclude that it will not be measured with an accuracy close to this one.

As it was discussed in chapter 4 one of the major sources for errors is the non-uniformity of the matrix pixels. This will lead to double-interaction matrixes that exhibit a polarized form even for the cases where this is not true and will distort polarizations measurements in both magnitude and angle of polarization.

6.2–Uniformity Tests

To correct the non-uniformity a simple test was made to each pixel. Each pixel was irradiated, one at a time, for 100 seconds, with a collimated, highly active, 122 keV Co-57 source. This source was chosen for its high activity, 10 mCi, for the high photoelectric and low Compton cross-section with the detector and because it was easier to collimate than the 511 keV. This was done with a setup as the one shown in figure 6.10. In it one can see that the source, enclosed in the lead container with a 0.5 mm hole to collimate radiation, is set on a static table. The detector on the other hand is placed right below it in a micrometric moving platform. This table allows to move the detector at will in the horizontal plane be it in any of the two axis or rotationally wise. With it, the collimated beam was centered with an initial pixel by watching the intensity map in the LabView software.

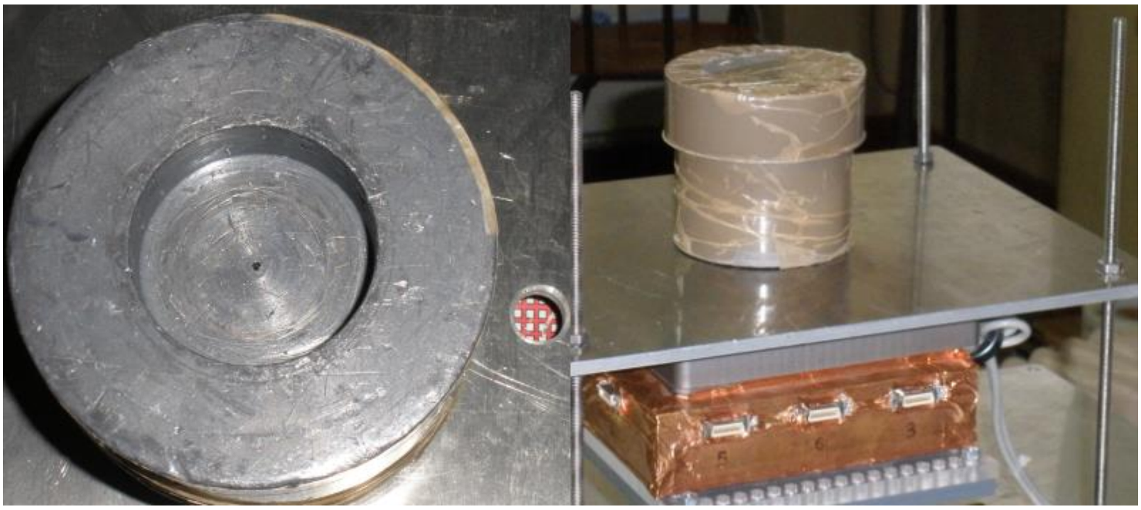

Figure 6.10 a) and b): In the left image one can see the lead collimator with a 0.5 mm aperture and a 3 cm thickness where the 122 keV source was placed. The circle to its right is an opening in the support table where the collimator is placed. In the right image the collimator is already placed in the table. It remains in the same position while the detector is moved from pixel to pixel.

Given the energy of the radiation and the collimator material it was possible to see the centered pixel highlighted while the others remained dark letting it be known that the source was incident in a pixel alone. Notice that even though the adjacent pixels were dark they still had over a thousand counts. Since the pixel sizes and pitch between them were known to move to the pixel next to it was only necessary to move the micrometric table by 2.5mm in one of the axis. This process is shown in figure 6.11.

Results obtained using this method are present in figure 6.12. Black pixels are the ones that were excluded from this test. This exclusion occurred because the pixels were dead (142, 155, 157, 159, 175, 191, 207, 223 and 255), because they were not connected to the system (84, 196, 212 and 228) or because their typical number of counts was around half the other pixels (ASIC 7). All other pixels were considered active and the number of counts was registered. These pixels exhibit a normal behavior comparable with the ones made in previous tests [1], [2] and [3].

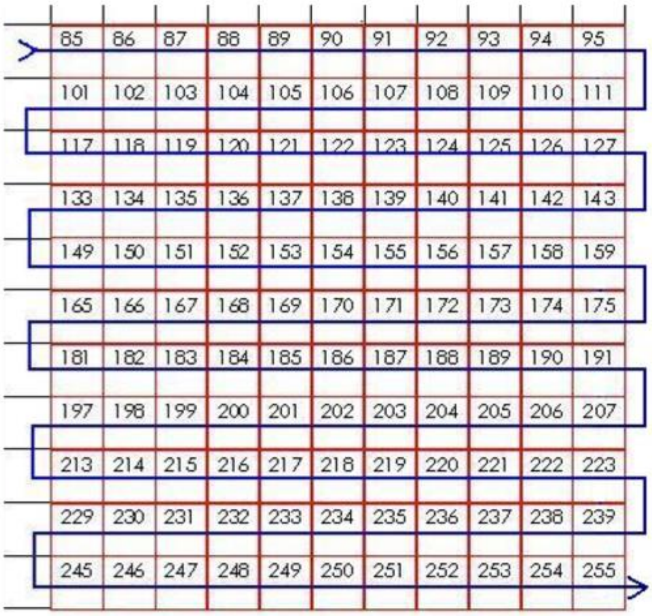

Figure 6.11: A possible path for the uniformity tests. This was not the one used since many of the channels had pixels with a lot of background that did not allow an easy reading of the irradiated pixel. In this case pixel measurements started in pixel 217 and followed no specific order.

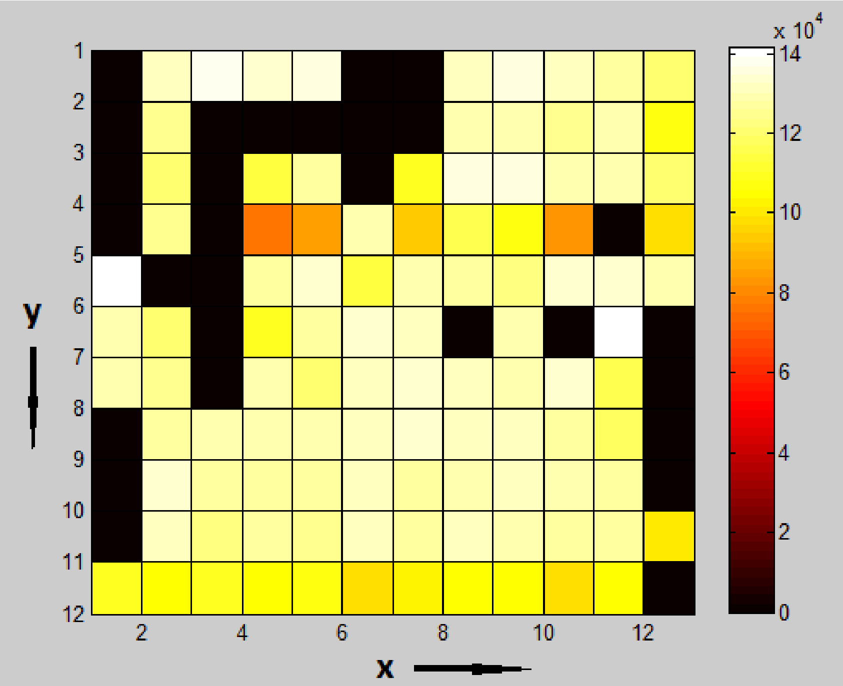

Figure 6.12: Intensity map from the uniformity tests on the full active detector surface.

This was not without exception though. In the pixels of ASICs 3 and 4 there was a higher variation than in the rest of the matrix. This was due to the presence of highly noisy pixels. With these pixels the number of events that reached the electronics system spiked and reached a point where two events would be superposed. This resulted in the appearance of a broad region with energies superior to the peak. Since these energies derived from the addition of low energy noise with peak count or even from the addition from two peak counts, the number of counts in the peak lowered and the resulting variation appeared.

Another difference that can be observed is the lower number of counts in the edges of the detector. This result is quite fascinating and can also be found in the results from previous tests. To explain this we need to look at the phenomena known as charge sharing. Charge sharing comes from the expansion of the charge cloud created by the ionizing particles during the charged collection process due to electrostatic repulsion and charge diffusion [4][5]. The charge from an interaction can then be collected by several pixels especially if these are small and/or thick [4]. If the collected charge is higher than the threshold then this will lead to worst \energy resolution and to an increased number of counts in each pixel. Applying this phenomenon to this case one can see that pixel in the edges have less adjacent pixels to share charge with. Therefore this effect will be inferior in these pixels what explains the slightly lower number of counts.

From the intensity map and from the noise observed in each pixel it was chosen the 4x4 matrix delimited by pixels 183 and 234.

Because of the change in the correspondence pixel → TAKES channel that occurred due to the construction of the new matrix new uniformity tests were made to correct any differences that would result from it. The results can be found in figure 6.13. Notice that the uniformity stays relatively the same. The number of counts in each measurement diminished because while the acquisition time remained the same the source had lost some of its activity naturally due to the radioactive process.

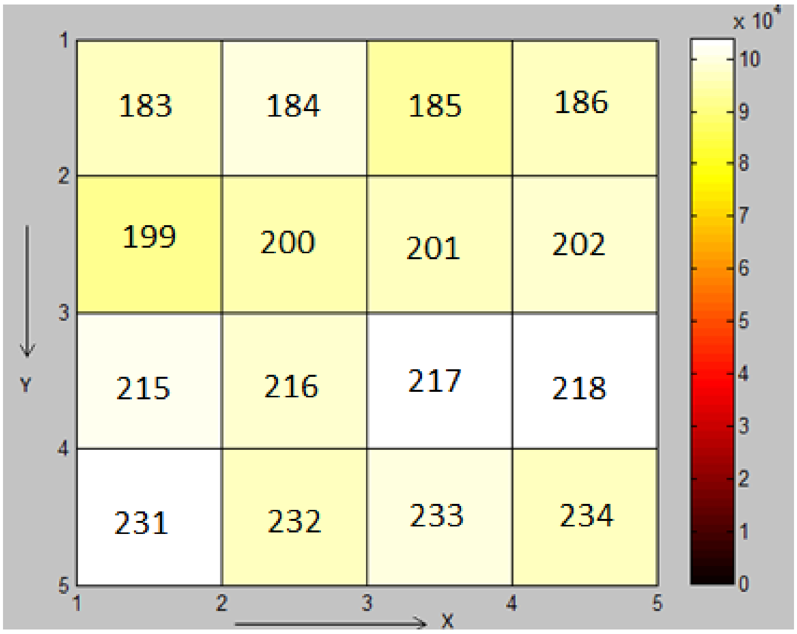

Figure 6.13: Intensity map from the uniformity tests on the 4x4 matrix. The numbers in each square correspond to the pixel number

6.3–Energy Calibration

Another issue was the energy calibration. Beside the typical offsets caused by the different response of each pixel to radiation, a major problem in our system is that each pixel's information goes through different electronic channels with different amplifications. This will result in a high fluctuation in the energy channels, for each pixel, when the same radiation is used.

As we have seen in chapter 3 the charge collected by a detector when an interaction of a particle occurs in its volume is directly proportional to the energy deposited. This relation can be found by irradiating the detector volume with several known mono-energetic sources in order to associate energy channels with the energy deposited by the interactions. A plot of the energy channel obtained vs the energy of the source can then be fitted to a line so that the relation can be defined.

Due to the low number of sources available the calibration done here only had 3 points. The energies used were 122 keV from Co-57, 511 keV from Na-22 and the 59.5 line from Am-241 (values taken from [6]). Ideally an energy value halfway between 122 and 511 keV should also be used but unfortunately this was not possible. The channels, each energy corresponded to, in each pixel, were obtained by irradiating every pixel until it had at least 10^3 peak counts. Results can be found in table 6.5 along with the slope m and the b intercept values obtained for each pixel. An example of a plot for this calibration is shown in figure 6.14. The closeness of the two lower energies introduce some bias towards the result.

#pixel	Channel #			Calibration line	
	59.5 keV	122 keV	511 keV	m	b
183	99.7	161.9	540.9	10.246	-43.27
184	65.4	126.7	494.4	10.545	-10.507
185	105.2	163.2	518.1	10.944	-56.091
186	63.2	124.8	507.5	10.163	-4.778
199	83.8	138.1	466.2	11.824	-40.374
200	71.6	121.2	412.2	13.295	-37.275
201	61.4	122.1	487.7	10.608	-65.079
202	69	125.3	466.1	11.385	-19.799
215	66.2	131.7	540.7	0.9514	-33.956
216	96.8	161.2	566	0.9618	-33.344
217	83.9	152.9	564.1	0.9422	-20.714
218	68.1	119.9	433.9	12.359	-25.365
231	49.3	103.1	428.4	11.927	-0.068
232	84.6	147	527.6	10.202	-27.345
233	90	147	473.4	11.825	-49.176
234	86.6	145.6	484.5	11.392	-41.323

Table 6.5: Results for the energy calibration of each pixel. The slope and the intercept were calculated with a linear fit.

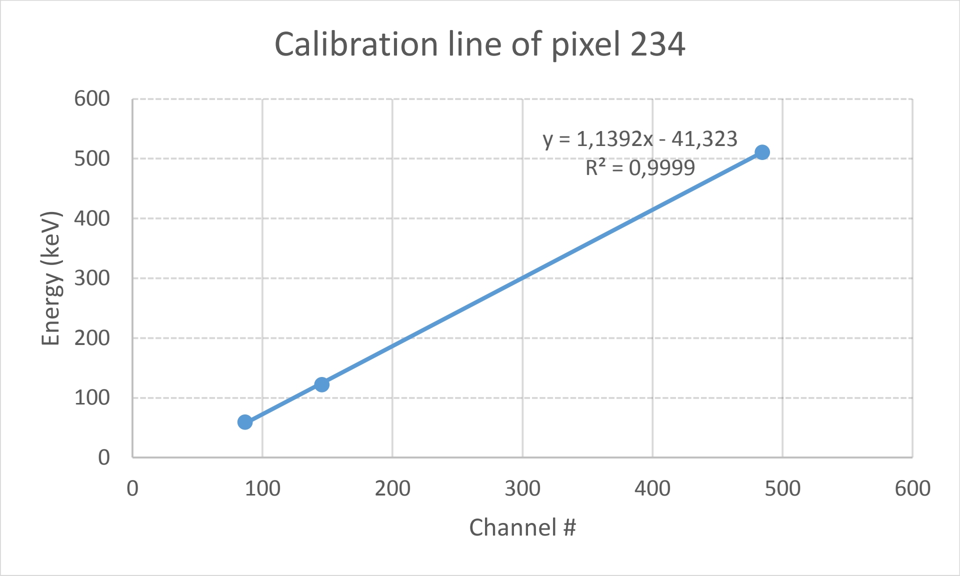

Figure 6.14: Calibration plot of pixel 234.

6.4–Experimental work

Initially, due to the lack of lead, the experiment was done with little collimation. In fact the only collimation came from the cylindrical container built in the laboratory by cutting lead stripes and enveloping them in a cylindrical shape. Figure 6.15 shows the assembly. A problem with this kind of setup is that there are photons that travel directly to the detector. To solve it a technique that consisted in applying energy filters to the data in the analysis was used. This filters limited the energies to between 70 and 90 keV for the first interaction (values decided according to the angles allowed for double interactions in the detector volume) and between 235 keV and 275 keV for the total deposited energy (full energy of the incident photons after they are Compton scattered in the aluminum target). The small window was also chosen in order to diminish the background contribution. The energy filters here mentioned are the ones used for the rest of the work.

With this assemble three different measurements were done. One with the detector as shown in the image above and two others with it rotated by an angle of 45° and 90°. Analysis of the data revealed that the angle of polarization in relation to the detector was not altered when the detector was rotated. This meant that the observed polarization was actually caused by a systematic error. Since the angle of polarization did not depend on the orientation of the detector, and after testing the electronics, we were led to conclude that the problem came from the detector. Simulations with the GEANT4 library showed that the volume of the detector that was not used would scatter direct photons into the active pixels creating a tendency at a 45° angle, the same as the one in the experiment. Another thing that was noticed was that the arm and the aluminum supports also contributed in a significant way to the number of photons that interacted in the detector through Compton scattering in them.

With this problems in mind and with more lead accessible the shielding of the experiment was possible. Figure 6.16 shows the new montage.

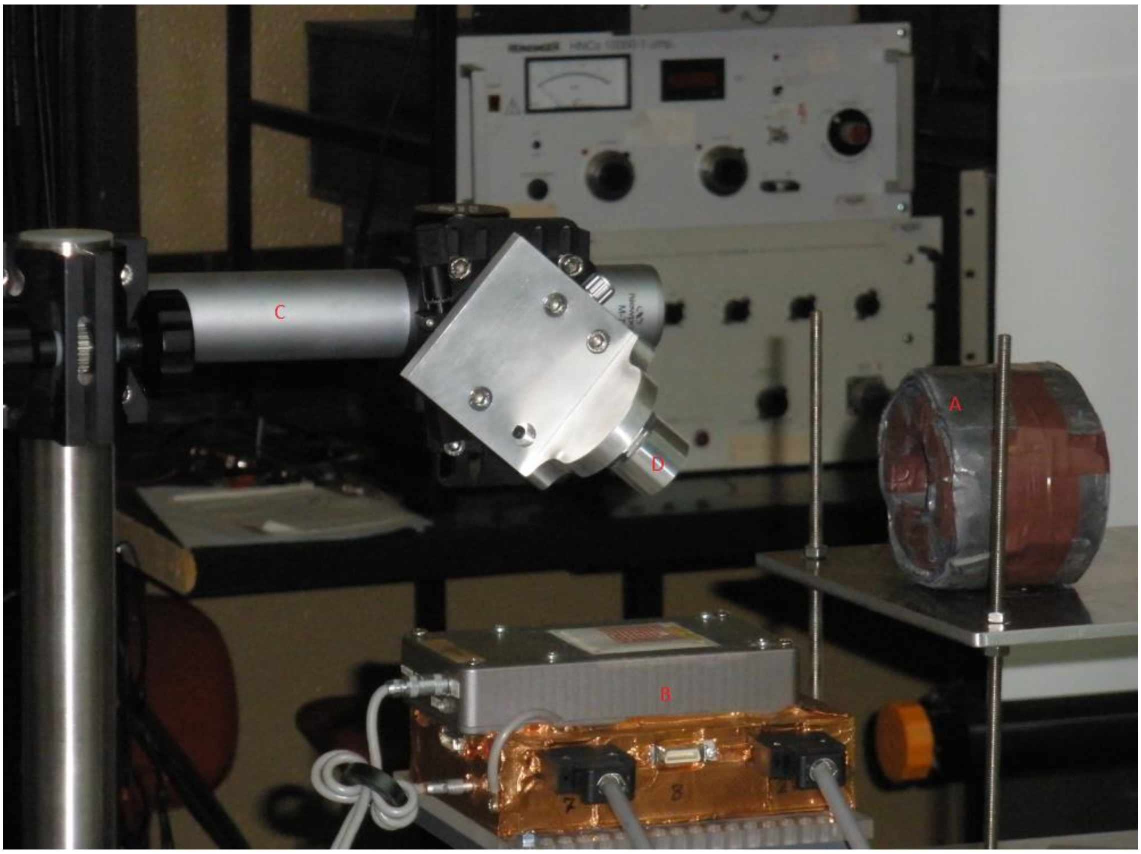

Figure 6.15: Assemble of the experiment. In we can see the collimator (object A), the detector (object B), the supports for the scattering material (object C) and the scattering material (object D) notice that the supports and the scattering material are made of the same element.

With this setup it is already possible to perform polarimetric measurements with the detector. However before presenting the results obtained there is a point that has to be discussed. The noise produced signals at the same rate as the experiment. This could be avoided if it was concentrated in a part of the spectrum that did not interfere with the experiment's spectrum by removing it with the energy filters. However, in this case, as it can be seen in figure 6.17, the spectrum occupies the same energy ranges as the first and second interactions that we seek. This meant that some number of double interactions were caused by two successive noise signals or a combination of a noise and a photon signal. Figure 6.18 shows the double interaction matrix generated by a 200000s acquisition with no source in the vicinity of the detector.

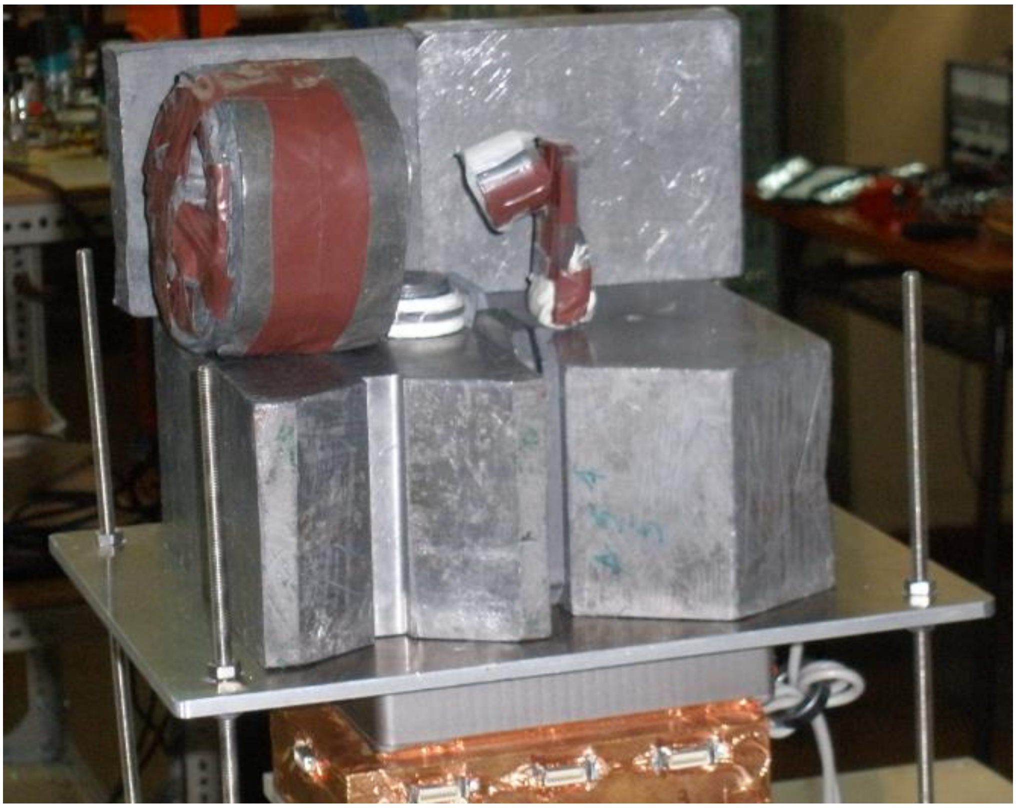

Figure 6.16: Shielded version of the experiment. Notice that the aluminum supports are no longer included and that the support is now made with blocks of lead. The spacing between the lead has the dimensions of the 4x4 matrix used, 1.5 cm.

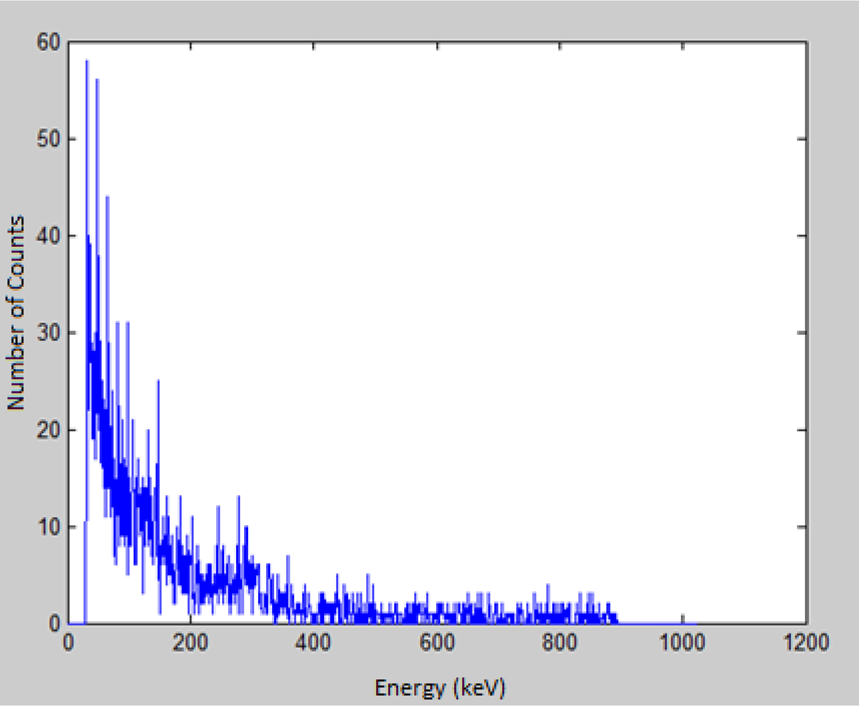

Figure 6.17: Spectrum of the noise in the pixel 201 for a 200000s acquisition. Only signals that were counted as coincidences are considered.

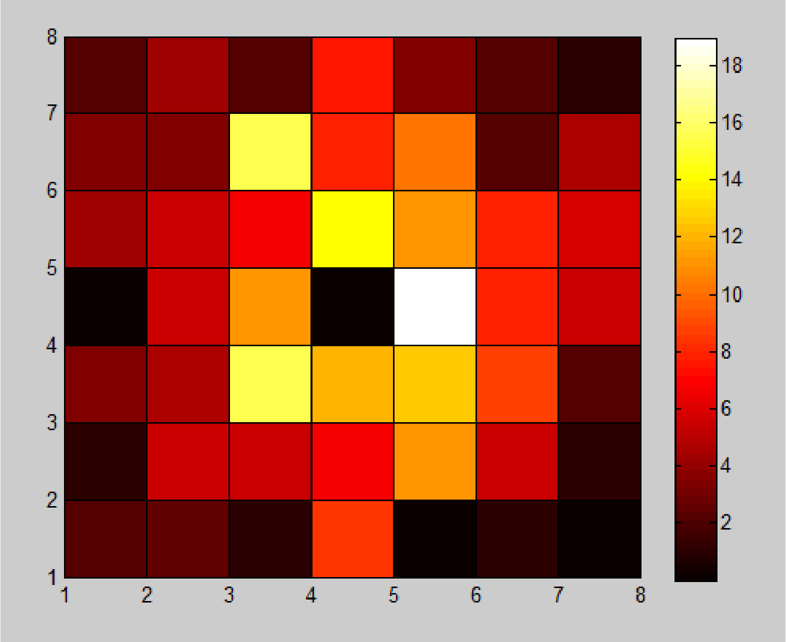

Figure 6.18: Double interaction matrix generated by a 200000s acquisition with no source.

Despite the low number of double interactions, it will interfere with the results obtained since the difference between the experiment's number of double interactions and this one is under one order of magnitude as it will be seen when I present the results.

6.4.1 – Unpolarized beam

In the same way that it was done in the simulations, first the polarimetric response of the detector to an unpolarized beam was obtained. Since there was no unpolarized source of ~255.5 keV available this test was done with the 511 keV ^{22}Na source. Since the beam is unpolarized, the residual Q factor that is measured will be a consequence of the tessellation of the pixels and as such it should not be very dependent on the energy. Figures 6.19 and 6.20 show the results obtained.

The resulting Q modulation peak is 0.0295±0.0011 a value that can already be confused with some polarization since the previous measured Q_{100} for a matrix of this type was of 0.40±0.12 [1]. Since no 100% polarized source was available this is going to be the Q_{100} value used to calculate the degree of polarization.

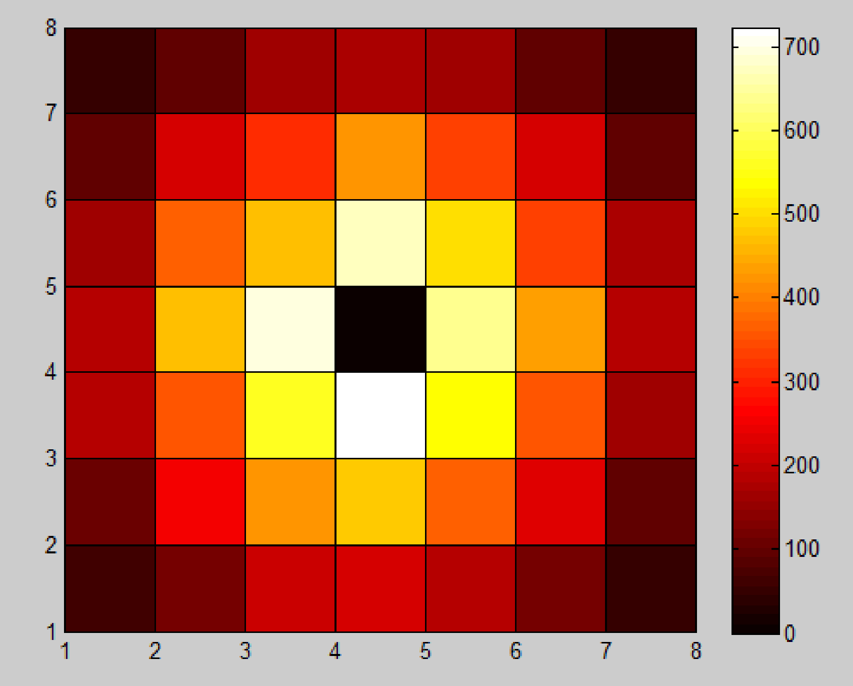

Figure 6.19: Double interaction matrix for an unpolarized 511 keV beam. The number of interactions increases from black to white.

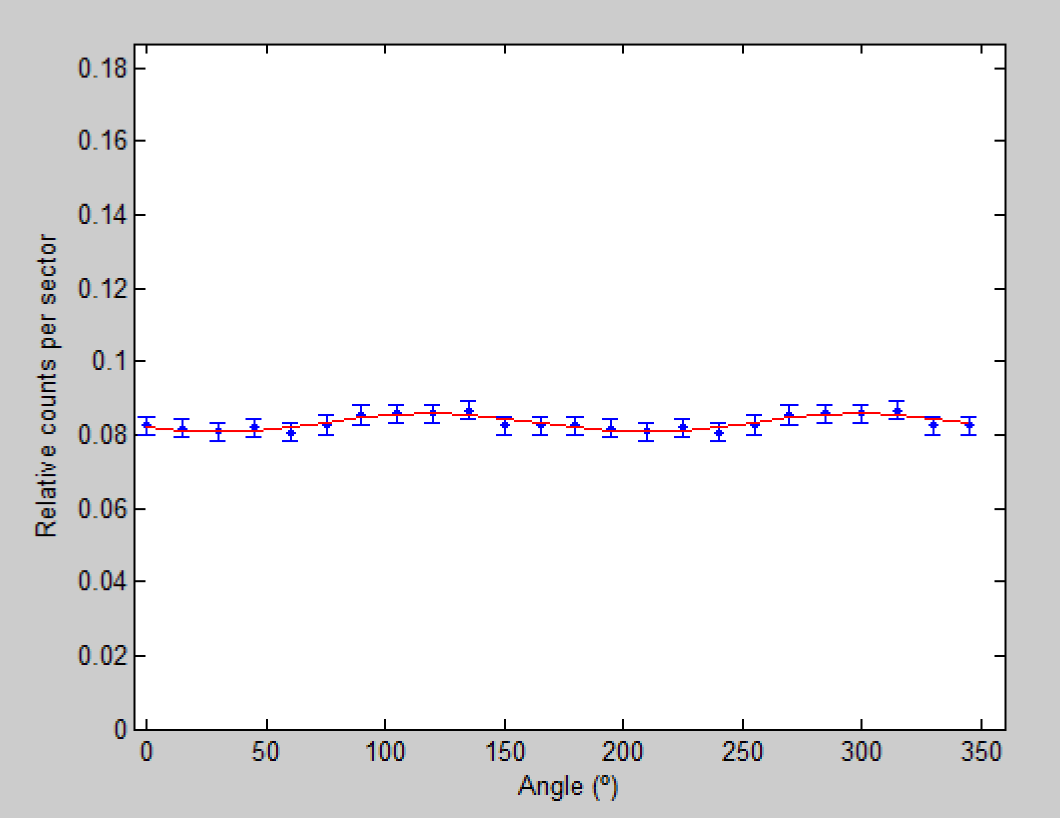

Figure 6.20: N(θ) distribution for the unpolarized 511 keV beam with its angle of polarization at 0°. The red line is the fitted function.

6.4.2- Experimental Polarimetry

With the experimental setup showed in figure 6.16 three measurements were made with the detector's x axis at 0°, 45° and 90° with respect to the angle of polarization. The acquisition time was 153000, 200000 and 235000s respectively. This increase was done because it is expected that the measurement is improved with the acquisition time. The double interaction matrixes are presented in figures 6.21, 6.22 and 6.23.

The modulation factor Q in this cases was very small, 0.0125±0.0222, 0.0374±0.0091 and 0.0537±0.0105 for the detector at 0°, 45° and 90° respectively. This corresponds to degrees of polarization under ~3% which cannot be correct since the expected value in the ideal conditions predicts a degree of polarization higher than 60%. The polarization angle was also wrong with great discrepancies, 0.62±101.415°, 8.7±13.9° and 113.92±11.17° respectively.

Looking at the double interaction matrix one conclusion can be made. If one looks only to the inner pixels, i.e., to the 8 pixels adjacent to the central one the polarization angle is evident. However in the other pixels this is not discernable at all. This occurs because the background in those pixels is much more significant since the number of interactions detected is very small.

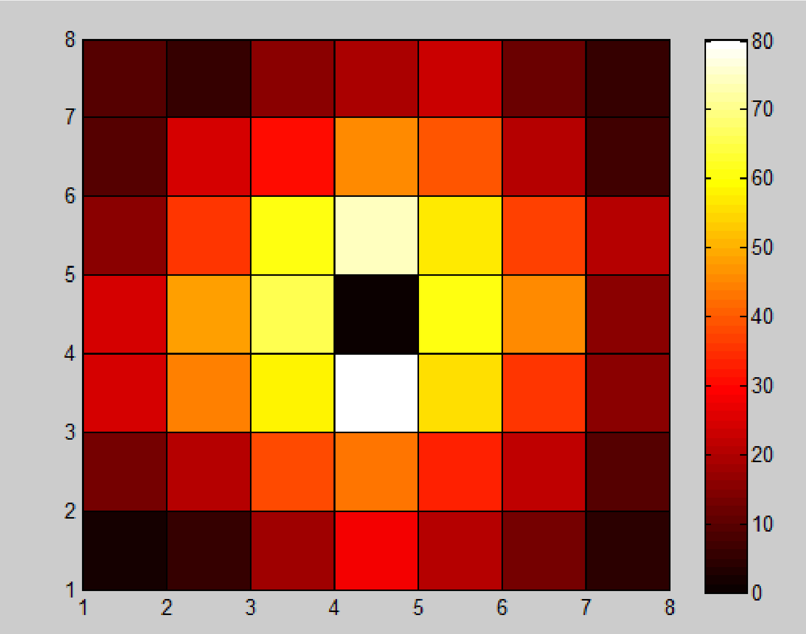

Figure 6.21: Double interaction matrix for a setup where the polarization beam expected to be at 0°.

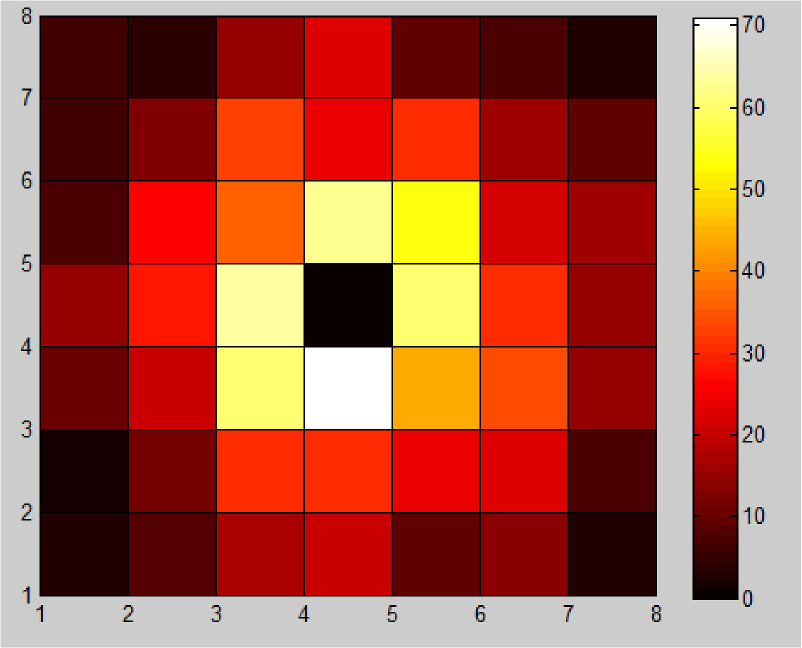

Figure 6.23: Double interaction matrix for a setup where the polarization beam expected to be at 45°.

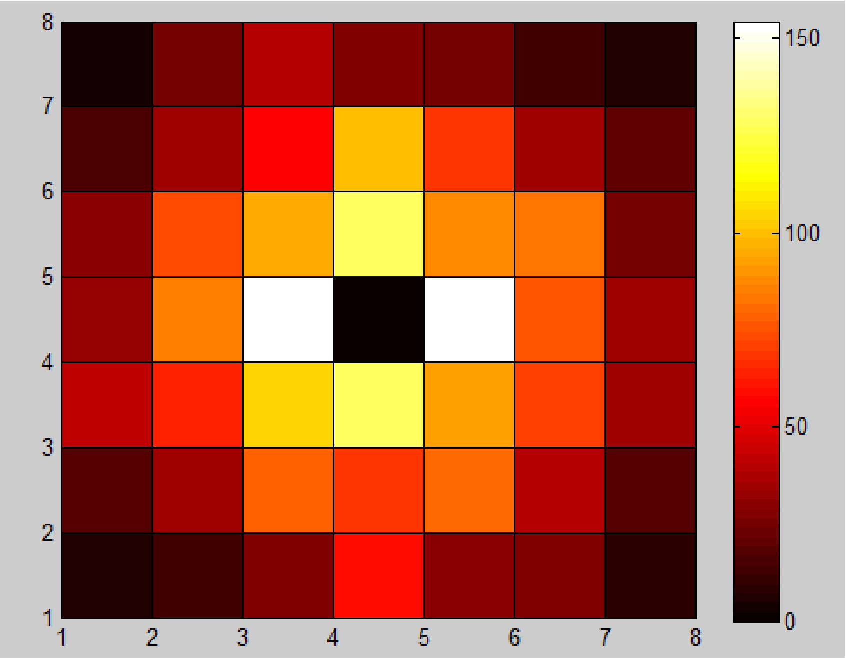

Figure 6.25: Double interaction matrix for a setup where the polarization beam expected to be at 90°.

Due to the low confidence in the number of interactions in pixels that were not adjacent to the central one a new approach was required.

Unlike in tests that have good statistics, where the adjacent pixels are suppressed to improve angular resolution, here all but the adjacent ones were suppressed. Since the mask that was used in the data analysis only used a fraction of the number of counts in each pixel, proportional to the area of the pixel that was in each bin, the degrade in resolution should be lower.

Another improvement done, that did not improve the measurements without this consideration, was the subtraction of the noise matrix to the ones obtained in the measurements. Since the acquisition time for the measurements with the detector at 0° and 90° was different than that for the noise measure a conversion factor, equal to the time of acquisition of the polarization measure divided by the acquisition time of the noise measure, was multiplied to the double interaction matrix.

6.4.3 – Final Results

With these new considerations the modulation for the unpolarized beam must be calculated again. Figure 6.27 shows the new results.

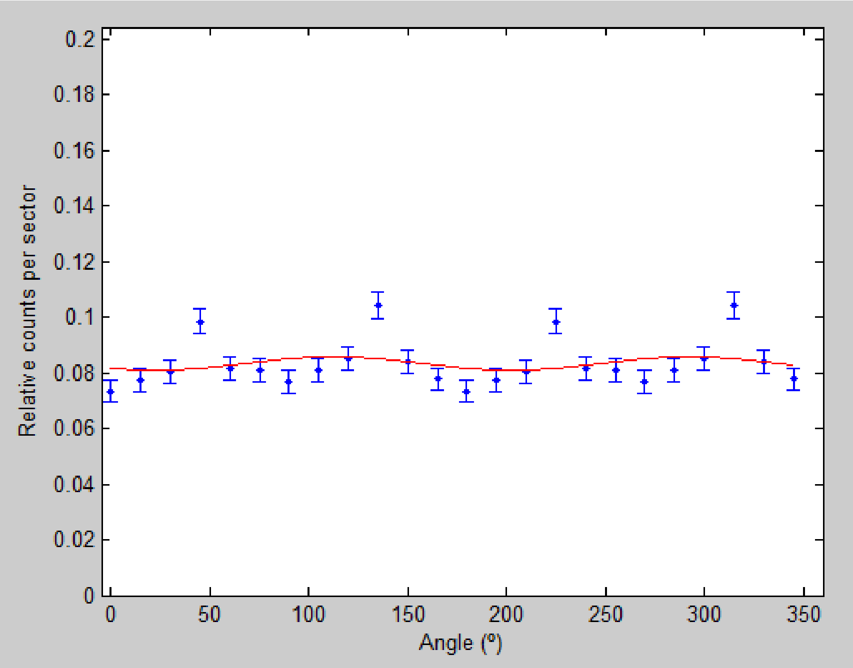

Figure 6.27: N(θ) distribution for the unpolarized 511 keV beam with its angle of polarization at 0°. The red line is the fitted function.

Notice that the modulation changed. This is expected since the outer pixels are no longer contributing. In fact when the same treatment is applied to the simulations the value of Q_{100} decreases to 0.36. When calculating the degree of polarization this must be taken into account then. As such I will use the value of Q=0.36 from now on.

With the residual Q distribution measured it is now time to test the new considerations. The next 3 images show the modulation for each measurement made.

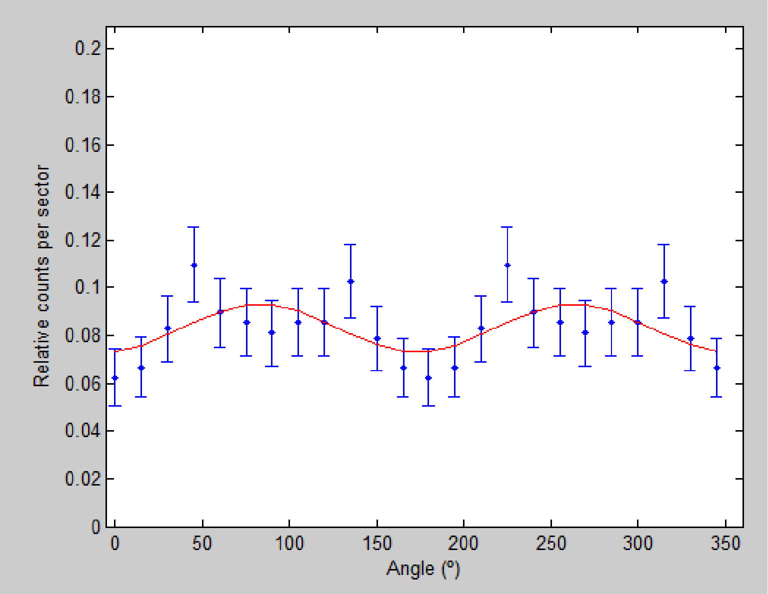

Figure 6.28: N(θ) distribution for a setup where the polarization beam expected to be at 0°.The red line is the fitted function

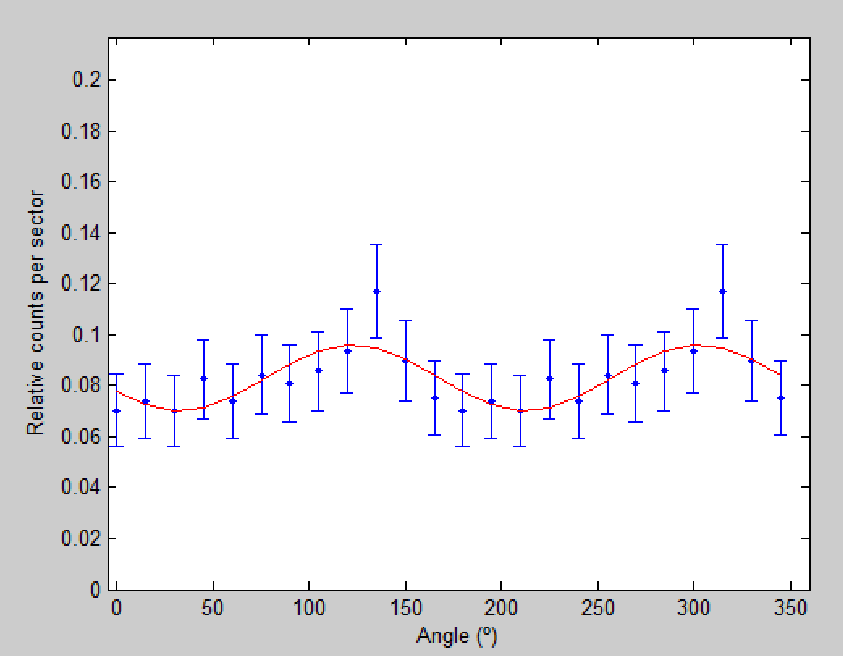

Figure 6.29: N(θ) distribution for a setup where the polarization beam expected to be at 45°.The red line is the fitted function

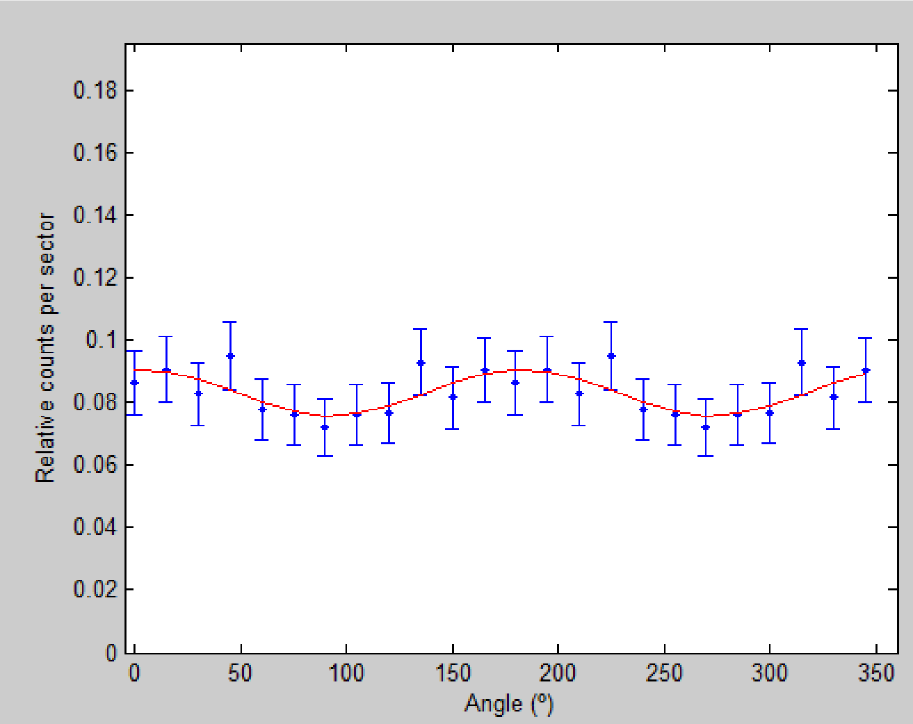

Figure 6.30: N(θ) distribution for a setup where the polarization beam expected to be at 90°.The red line is the fitted function.

This time N(θ) modulation shows a wider amplitude between its minimum and maximum. Table 6.6 shows the measured polarization angle when the detector axis was at 0°, 45° and 90°, the respective modulation factor and estimated polarization degree. In the table it can be seen that measured polarization angle is fairly consistent with the rotations performed on the system. Measured angles when the system is at 0° and 90° (note that does not mean that the polarization direction is also at these angles) where observed at about 90° apart within the measurement errors. At 45° the measured value is slightly lower than expected, however this was expected taking into account the low number of pixels of the matrix, its square shape that around 45° is not so easy to deal in polarimetric analysis, and also the fact that mask bin aperture was 15° wide.

Polarization Angle (°)	Measured Angle (°)	Modulation Factor Q	Degree of polarization (%)
0	12.0±5.8	0.117±0.018	32.5±5.00
45	33.3±9.53	0.118±0.019	32.78±5.28
90	97.5±4.3	0.116±0.009	32.22±2.50

Table 6.6: Measured polarization angle, modulation factor and estimated polarization degree.

This difference between experimental and simulated results has origin in three factors.

The first one is the system noise. As it was seen the subtraction the double interaction matrix for the noise helped improve the results; however this method is not perfect, a noise component will always be present. The noise also forced us to use a narrower window of energies which diminished the number of counts from the incident beam that became comparable with noise number of counts for pixels laying further from the center of the virtual 7×7 matrix.

Secondly, in the simulations it was considered that, the incoming beam, that entered the scattering material, was collimated. In reality this was not true due to logistic restrains. In fact the 4 cm distance between the source and the target and the ~1.5 cm radius of both allowed angles between the incident direction and two orthogonal axis to it to be as large as ~37° to be possible (see figure 6.31). A beam of photons originating at either the top or bottom of the source and interacting in the bottom or top of the scattering material will have 41.33% polarization. If one considers all the possible angles then the average polarization will be lower than the predicted 66% but not by a great amount. Considering now that the dispersion is in the azimuthal angle then according to the mechanics of Compton scattering the degree of polarization of the beam should not change. However, the angle of polarization of the beam that reaches the detector will. If we transform the magnitude of the polarization vector into the axis correspondent to the polarization angle expected and to the perpendicular one then the average polarization will be diminished by a factor of 0.93.

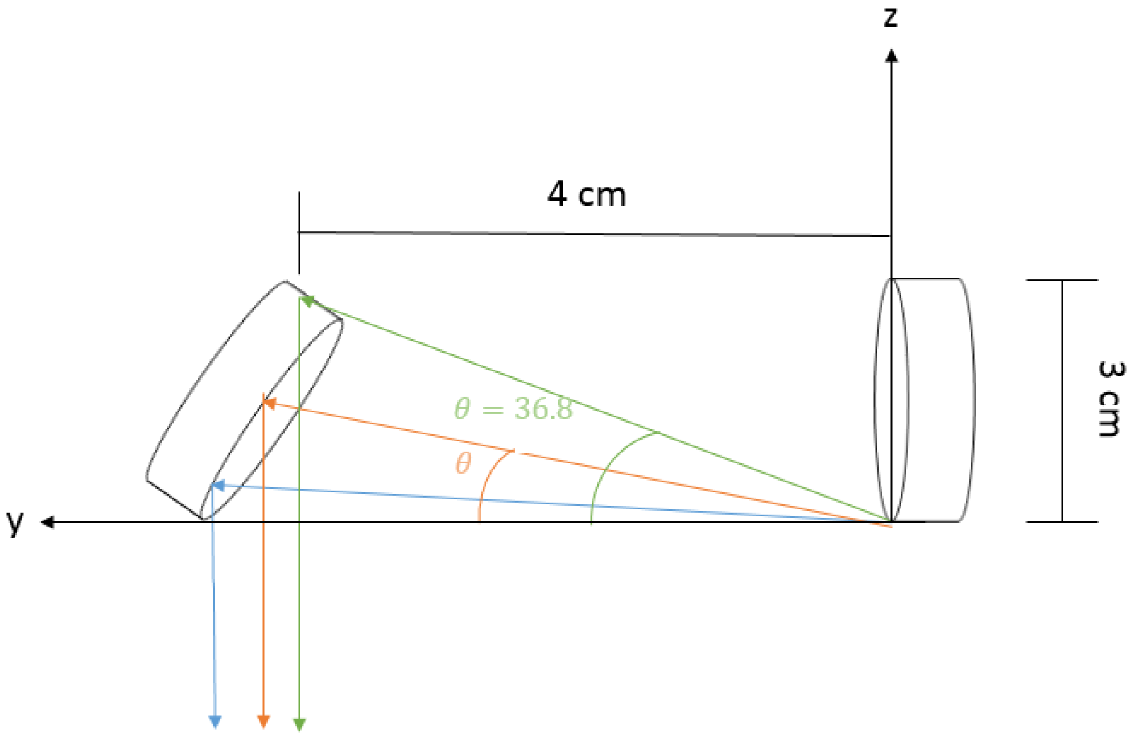

Figure 6.31: Different trajectories for photons leaving the source and interacting in the scattering material.

This dispersion in the angle of scattering also results in a broader band of energies that reaches the detector. Even though that energy filters were applied there are still photons with different parameters than those expected that are detected. This is due to the Compton mechanics allowing a continuum of energies and scattering angles that can be unexpected in an experiment. For example in the setup shown in figure 6.15 it was verified that the removal of the aluminum supports changed the number of interactions in the detector. The same is true for lead but with less probability, and even with the detector volume that is not used. These unaccounted photons can also introduce significant error that is difficult to predict and remove. Another point that must be taken into account in this regard is in the scattering material chosen, aluminum, 10% of the photons interact more than one time further reducing the polarization and broadening the range of energies.

Lastly it was considered that the beams arriving to the detector were parallel. However given the setup with a 10 cm average distance between the scattering material and the detector, and the 1.5 cm side dimensions of the detector one can calculate that angles as wide as 8.53° can occur. In this case photons crossing the irradiated pixels will not be scattered uniformly as it can be seen in figure 6.32.

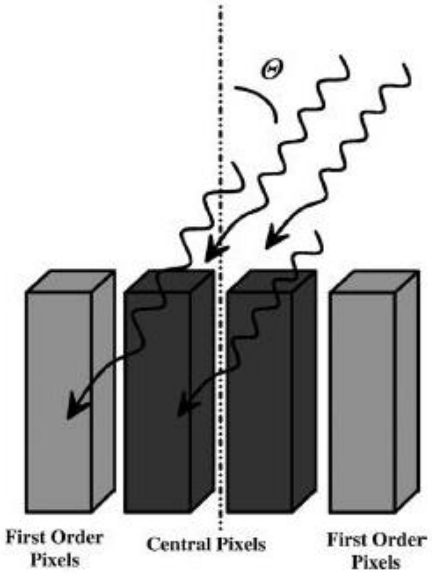

Figure 6.32: Schematic view of central pixels irradiated by a polarized inclined beam at angle θ with respect to the detector optical axis. In this case photons crossing the irradiated pixels surface will not be scattered uniformly inside this pixels. Preferentially they will be scattered closer or inside the first order pixels laying in the horizontal projections of the photon propagation direction [6].

Previous studies, [6] and [7], where the same detector was irradiated by inclined beams up to 10° off the orthogonal surface of the detector showed that for angles up to about 2° had negligible influence in modulation Q factor calculation. However from 2° up to 10°, the incoming photons crossing the irradiated pixels surface will not be scattered uniformly inside these pixels. Preferentially, they will be scattered closer or inside the adjacent pixels laying in the horizontal projection of the photon propagation, originating charge electron-hole track whose charge will be more likely shared by two pixels and therefore events that will be excluded by energy selection methods. Furthermore, Compton photons will more likely scattered in the projection of the photon propagation direction worsening the double events distribution definition in the detector matrix. . The referred studies indicate that for energies between 200 keV and 300 keV the modulation factor can be leveled by Q > 0.05. Given that wider angles are a rarer occurrence whiles angle in between are fairly common it can be predicted that the value of Q will diminish substantially up to 0.05, which corresponds to a decrease in the measured polarization of about ~15% with respect to perfect parallel beam. Therefore, the true beam polarization seen by the detector is the result of the initial scattered beam with a polarization slightly higher than ~50%, due to non-collimated radioactive source beam, decreased by these ~15% due to beam inclination, which should provide a final beam polarization degree of the order of 35%. The measured polarization ~32% and the respective error are consistent with this estimation. Furthermore, as pointed in the first place, system noise also plays a role in the decrease of measured polarization degree.

References

[1]] G. Ventura, E. Caroli, N. Auricchio, A. Donati, G. Landini, F. Schiavone, R. M. Curado da Silva, POLCA2 (POLarimetry with CZT Arrays): experimental set-up, calibration procedures and results, CZT-IASF-BO-004.

[2] G. Ventura, E. Caroli, N. Auricchio, A. Donati, G. Landini, F. Schiavone, R. M. Curado da Silva, POLCA (POLarimetry : experimental set-up, calibration procedures and results, Internal Report IASF/BO n. 452/2002 (2007)

[3] E. Caroli, A. Donati, G. Landini, F. Shiavone, J. B. Stephen, G. Ventura, R. M. Curado da Silva, S. Sordo, N. Auricchio, A. Pisa, V. Honkimaki, LAPOLCA: USER MANUAL FOR ESRF 2008 TESTS, CZT-IASF-BO-007

[4] Semiconductor Pixel detectors and their applications in life sciences, J Jakůbek
2009 *JINST* **4** P03013

[5] “Charge sharing in common-grid pixelated CdZnTe detectors”, Jae Cheon Kim et al, Nuclear Instruments and Methods in Physics Research A 654 (2011) 233–243

[6] Curado et al, “Polarimetry Study With a CdZnTe Focal Plane Detector”, IEEE TRANSACTIONS ON NUCLEAR SCIENCE, VOL. 58, NO. 4, AUGUST 2011

[7] R. M. Curado da Silva, E. Caroli, J. B. Stephen and P. Siffert, “CIPHER, A polarimeter telescope concept for hard X-ray astronomy”, Experimental Astronomy, volume 15, 2003

Chapter 7

Conclusion and Future Work

With this work the necessary arrangements to further research polarimetry with a CdTe semiconductor were made. This was the first time that full irradiation of the detector was used to test its polarimetric performances and as such a few problems were found. Despite these difficulties, the polarization angle and degree were well measured and comparable with simulation results. Regarding the angle of polarization measurements for three different orientations of the detector (0°, 45° and 90°) the measured angles were in agreement (12.0°, 33.3° and 97.5°) with the rotations performed on the system. The discrepancies are well within the bin size of the mask developed for the data analysis. A polarization degree of about 32% was estimated when compared with simulation calculations. This polarization degree is consistent with the fact of that the Compton beam polarization process was performed by a partially collimated source beam, that the polarized beam was not perfectly orthogonal to the detector surface and not monochromatic and that a non-negligible system noise was present.

These results show that a future polarimeter with a planar configuration (simple or multi-layer) is potentially suited to perform polarimetric measurements for high energy astrophysics, in particular to detected polarized celestial emission sources below 30% with an angular resolution around 5°.

The simulations with the GEANT4 library further proved that CdTe is well suited for polarimetric measurements. In fact the modulation factor for a 100% polarized beam measured was ~0.44, a large improvement over the INTEGRAL satellite’s instruments (~0.30) considering the small dimensions of the matrix used. Besides this the simulations made to test different materials to polarize the beam showed that aluminum has an advantage over small and higher Z materials due to its combination of high Compton cross-section and low multiple interaction probability.

This work was one of the first steps for the characterization of polarimeters in the laboratory, an alternative to accelerator polarized beams. These successful results will allow in the future to measure further beam profiles, with different degrees and angles, and different detector configurations. Other planned tests include the use of multi-planar and 3D position sensitive detectors in order to improve the sensitivity and the polarimetric capabilities of a future gamma-ray mission, such as AstroMeV mission proposal.

Annex A – Mass Attenuation Coefficients

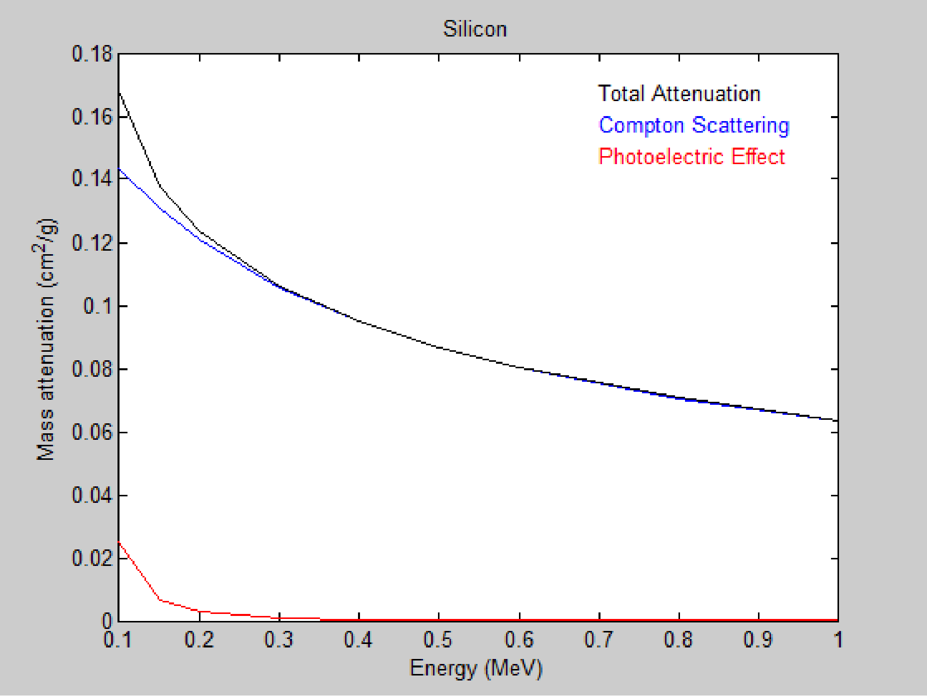

Figure A.1: Mass attenuation coefficient for the Photoelectric effect and Compton scattering in Silicon for the 0.1-1MeV range.

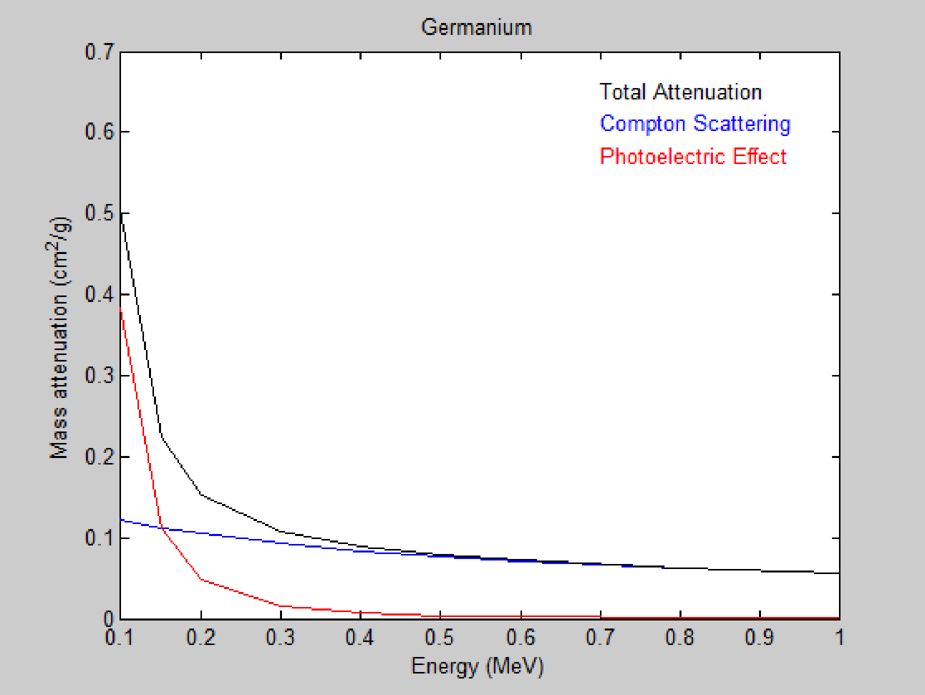

Figure A.2: Mass attenuation coefficient for the Photoelectric effect and Compton scattering in Germanium for the 0.1-1MeV range.

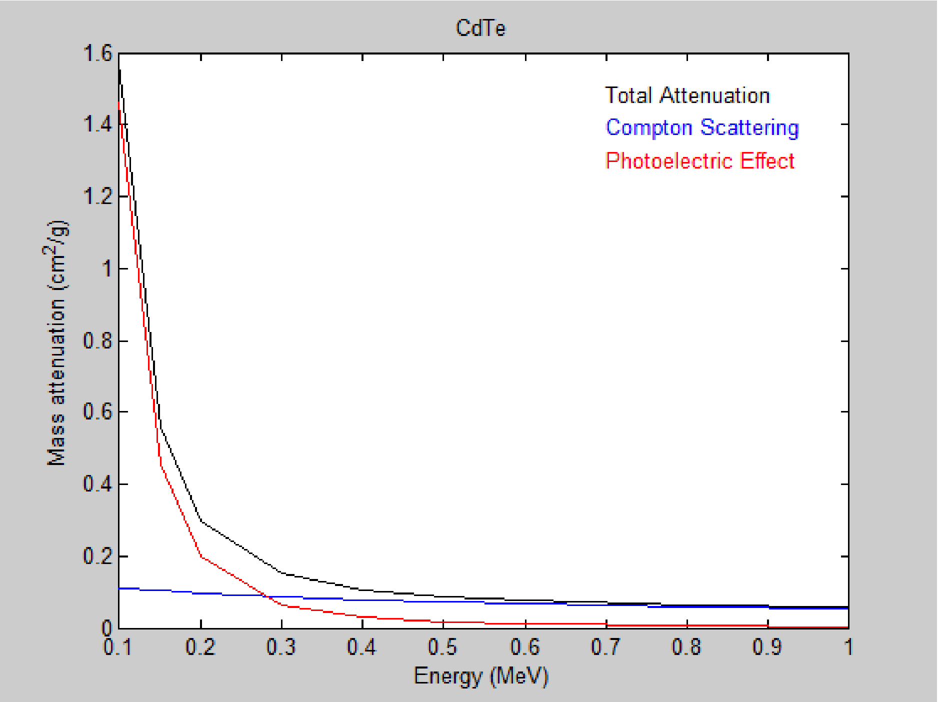

Figure A.3: Mass attenuation coefficient for the Photoelectric effect and Compton scattering in CdTe for the 0.1-1MeV range.

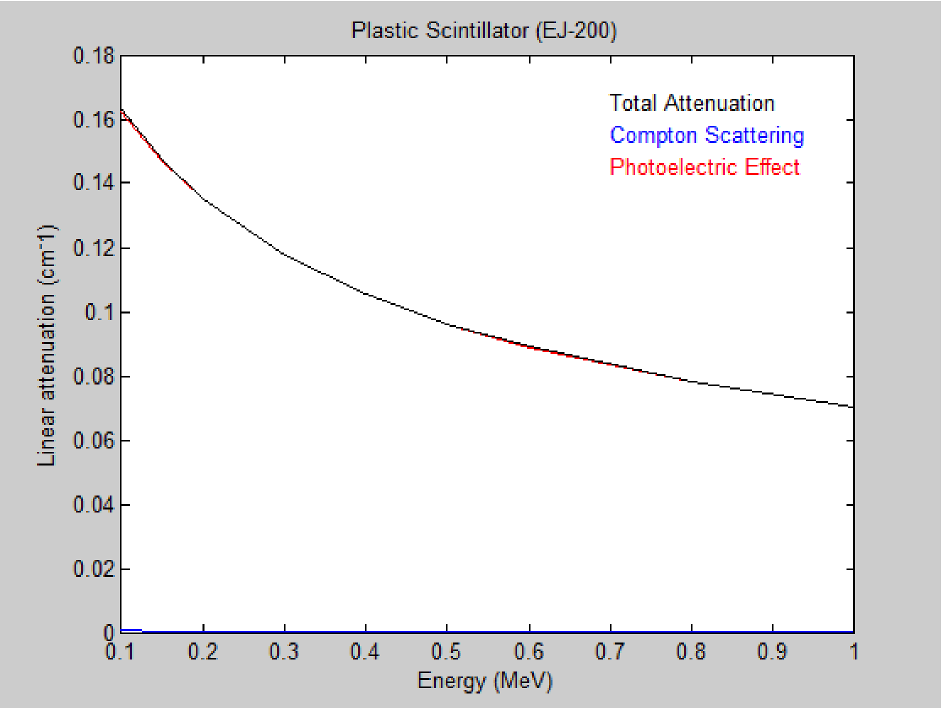

Figure A.4: Mass attenuation coefficient for the Photoelectric effect and Compton scattering in a Plastic Scintillator for the 0.1-1MeV range.

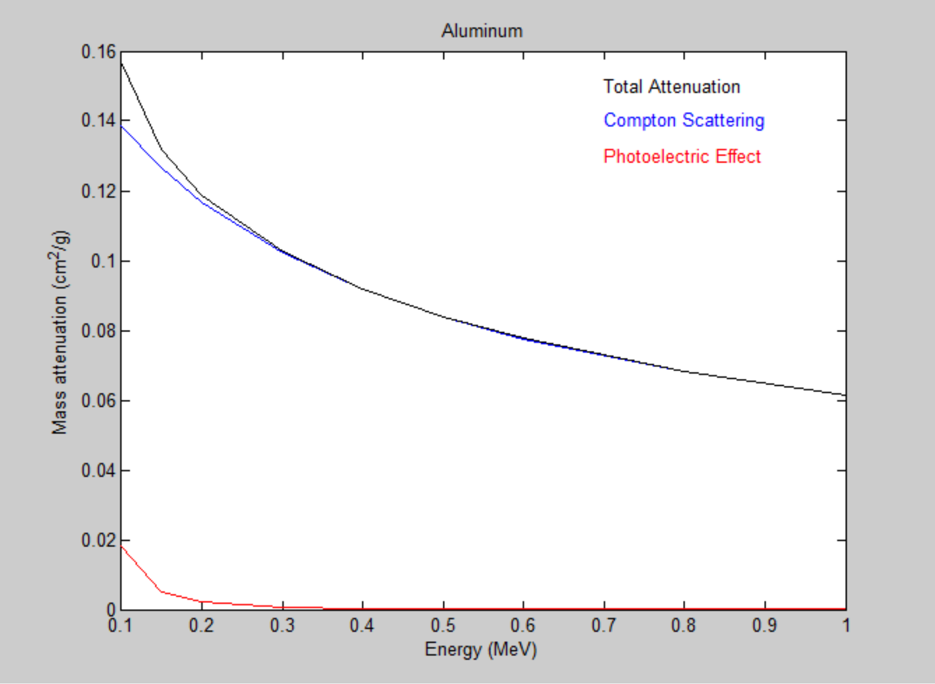

Figure A.5: Mass attenuation coefficient for the Photoelectric effect and Compton scattering in Aluminum for the 0.1-1MeV range.

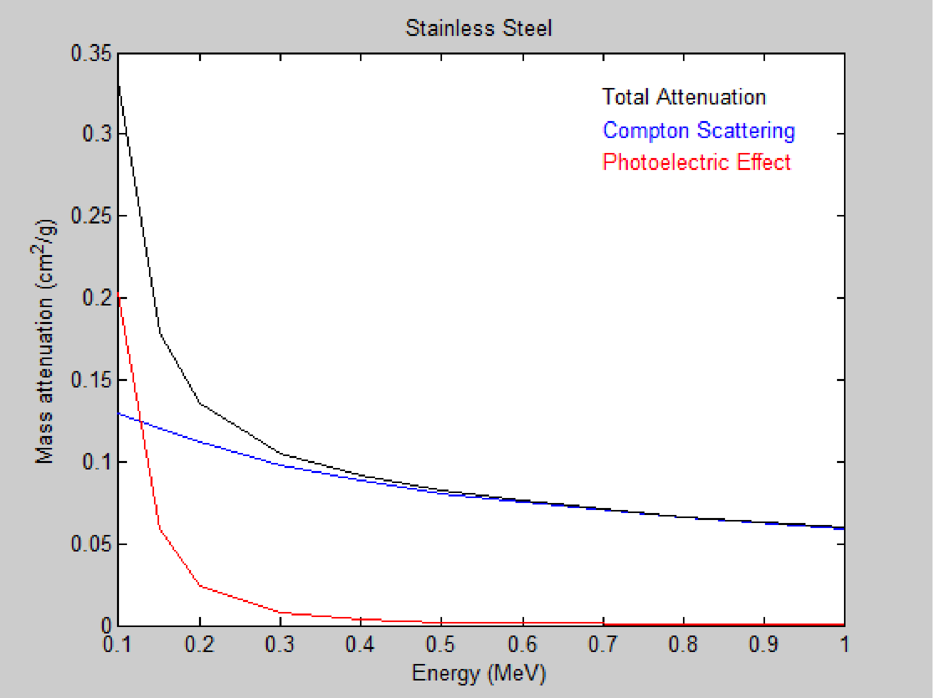

Figure A.6: Mass attenuation coefficient for the Photoelectric effect and Compton scattering for a league of stainless steel for the 0.1-1MeV range.

Annex B – Results for the simulations with GEANT4

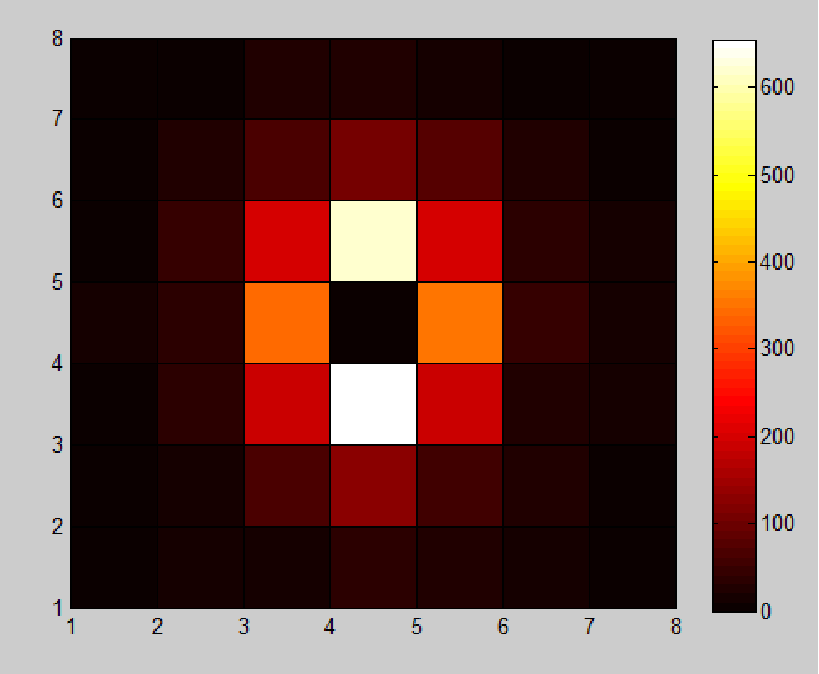

Figure B.1: Double interactions matrix (a) and Q distribution fitted to a cos(2θ) function for a 80% polarized beam with its polarization vector at 0°

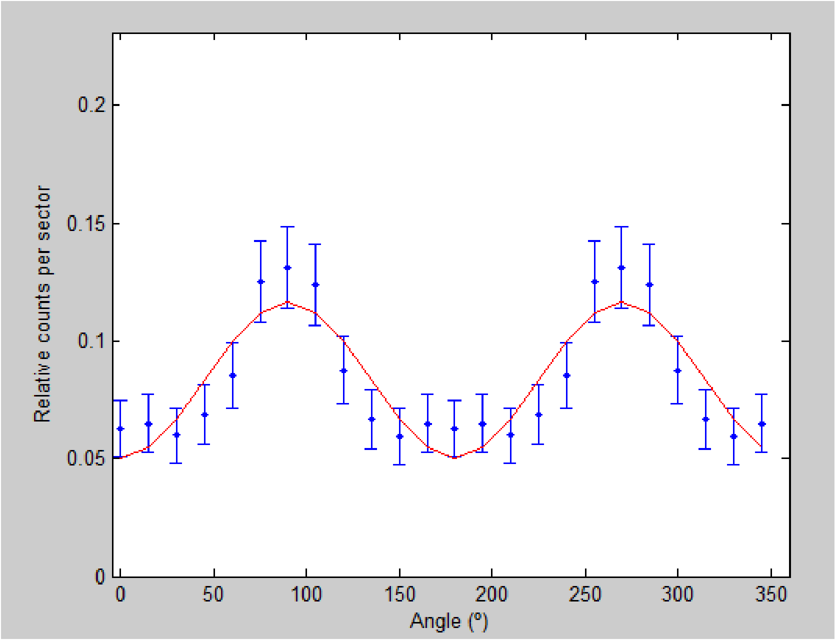

.

Figure B.2: N distribution fitted to a cos(2θ) function for a 80% polarized beam with its polarization vector at 0°.

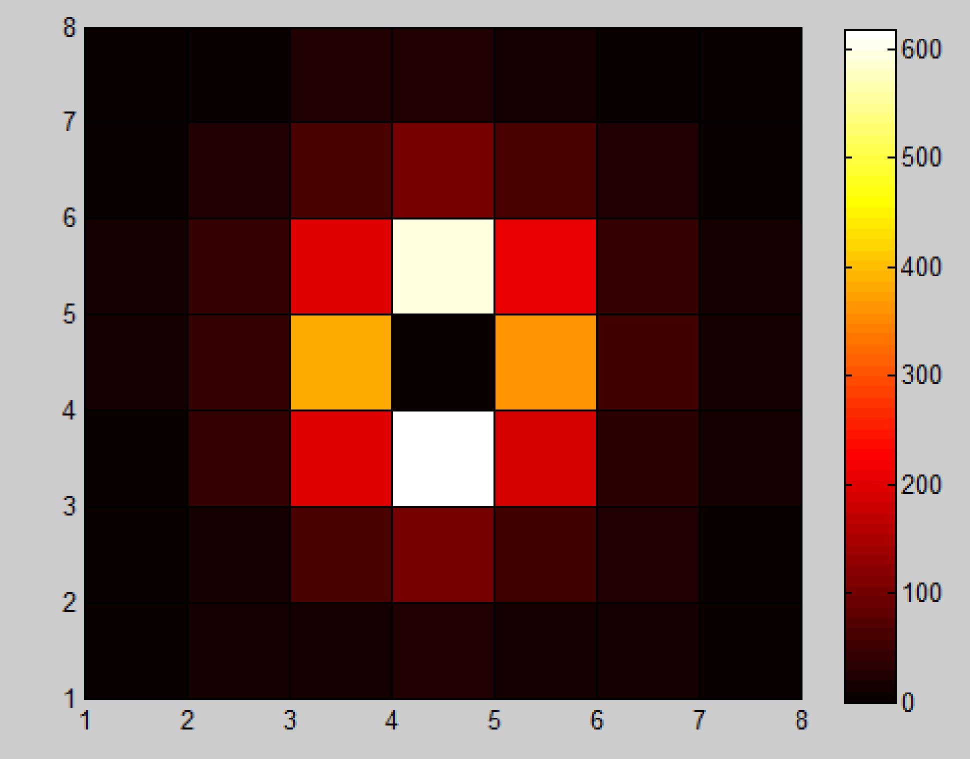

Figure B.3: Double interactions matrix (a) and Q distribution fitted to a cos(2θ) function for a 60% polarized beam with its polarization vector at 0°.

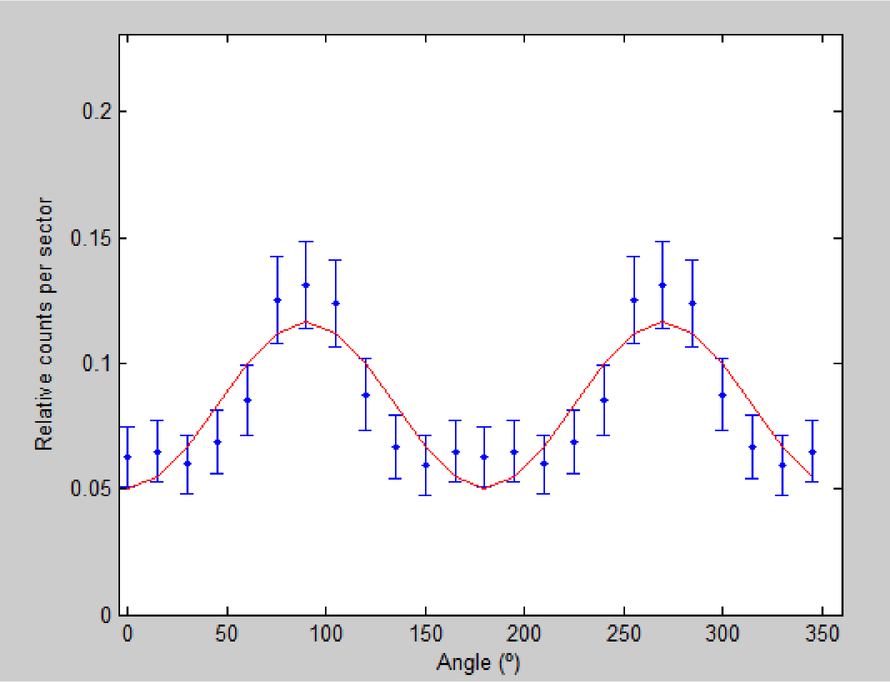

Figure B.4: N distribution fitted to a cos(2θ) function for a 60% polarized beam with its polarization vector at 0°.

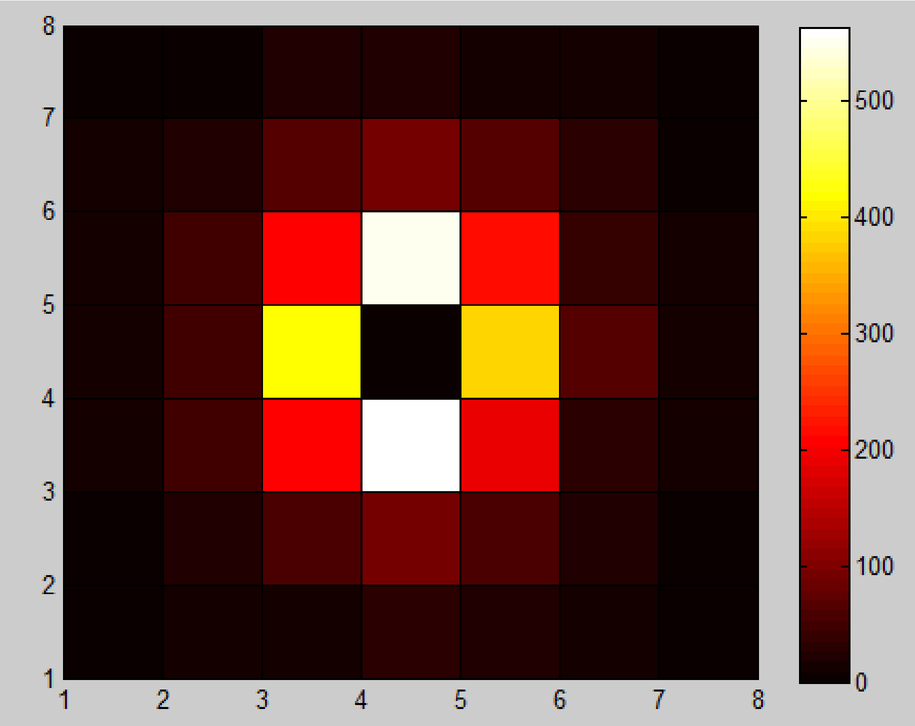

Figure B.5: Double interactions matrix (a) and Q distribution fitted to a cos(2θ) function for a 40% polarized beam with its polarization vector at 0°.

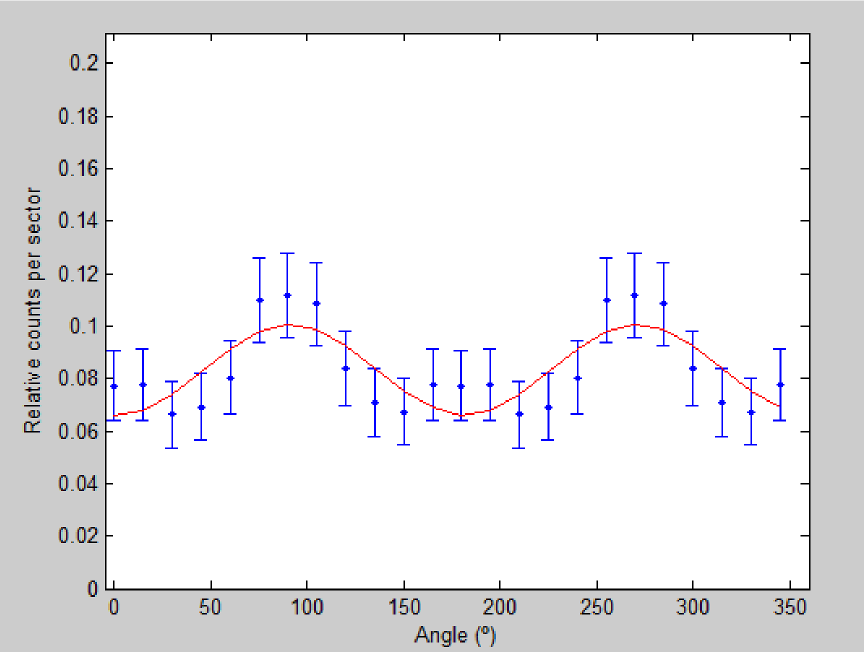

Figure B.6: N distribution fitted to a cos(2θ) function for a 40% polarized beam with its polarization vector at 0°.

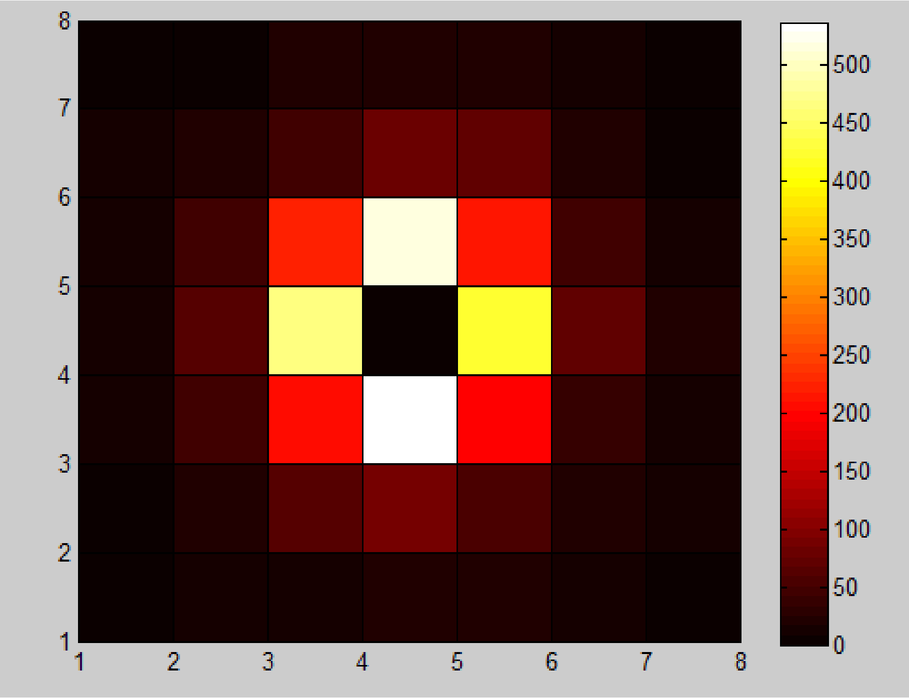

Figure B.7: Double interactions matrix (a) and Q distribution fitted to a cos(2θ) function for a 20% polarized beam with its polarization vector at 0°.

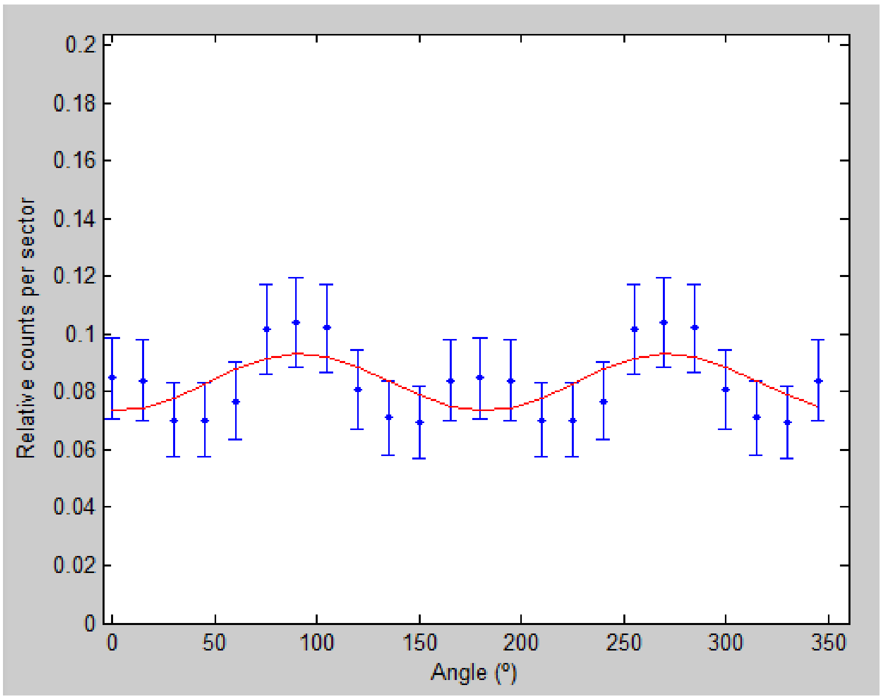

Figure B.8: N distribution fitted to a cos(2θ) function for a 20% polarized beam with its polarization vector at 0°.

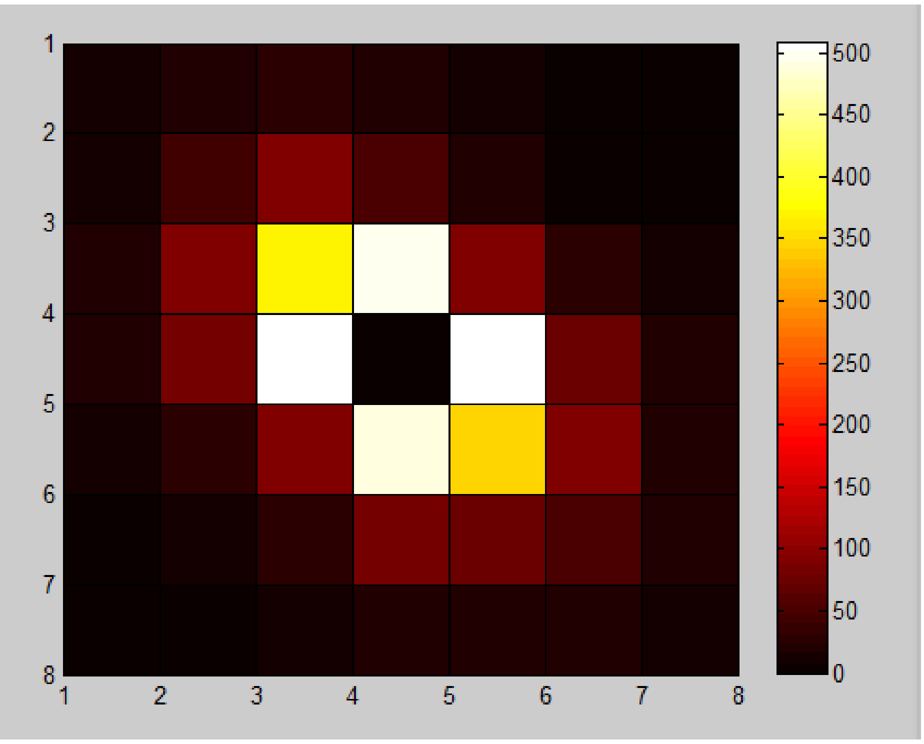

Figure B.9: Double interactions matrix (a) and Q distribution fitted to a cos(2θ) function for a 100% polarized beam with its polarization vector at 45°.

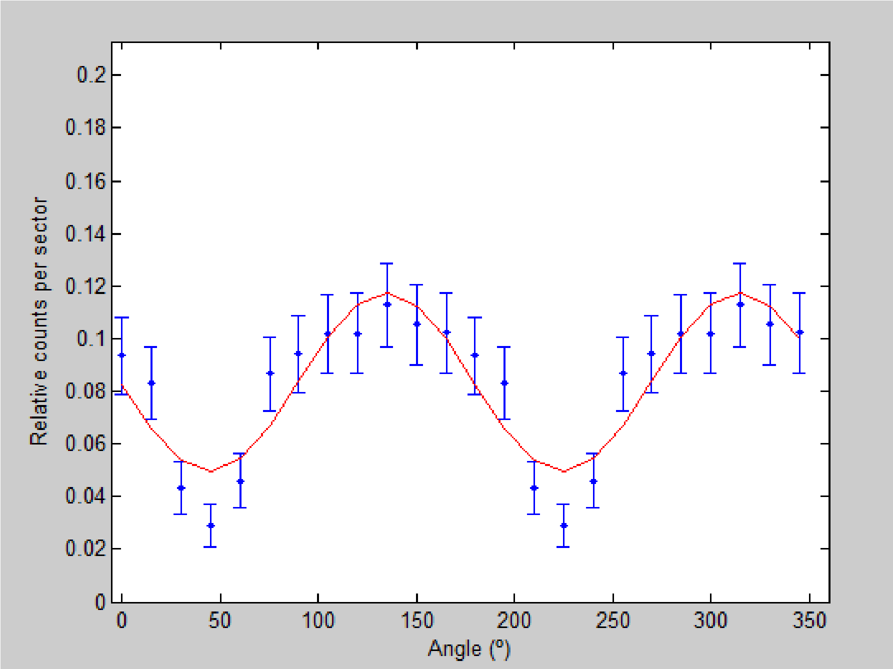

Figure B.10: N distribution fitted to a cos(2θ) function for a 100% polarized beam with its polarization vector at 45°.

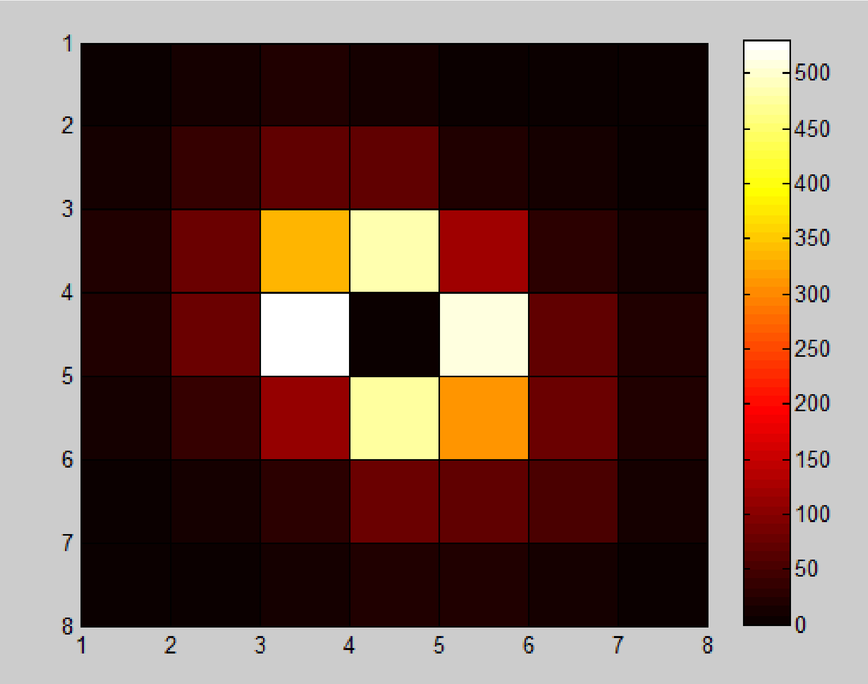

Figure B.11: Double interactions matrix (a) and Q distribution fitted to a cos(2θ) function for a 80% polarized beam with its polarization vector at 45°.

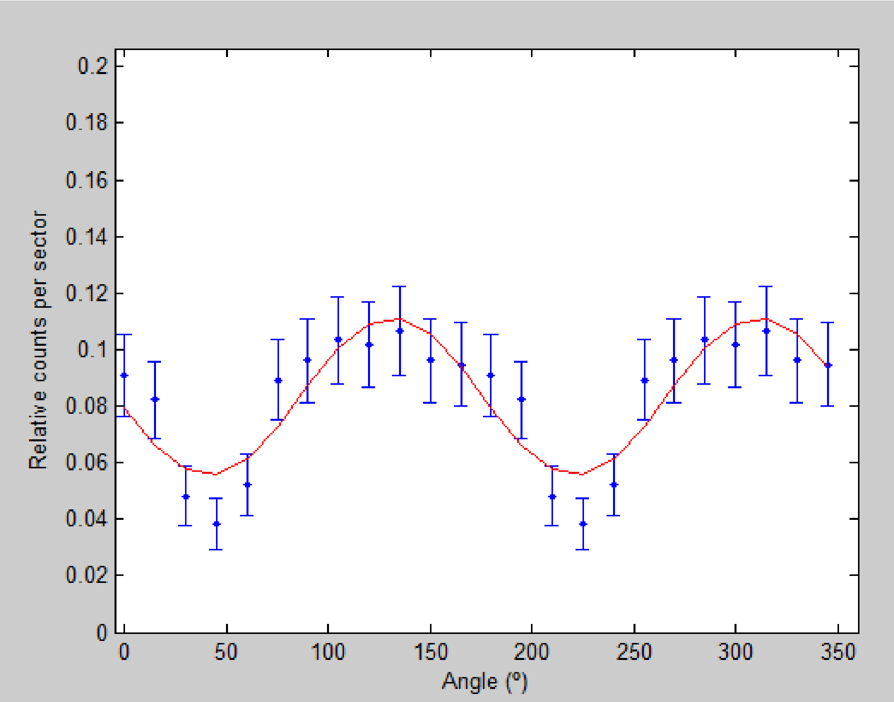

Figure B.12: N distribution fitted to a cos(2θ) function for a 80% polarized beam with its polarization vector at 45°.

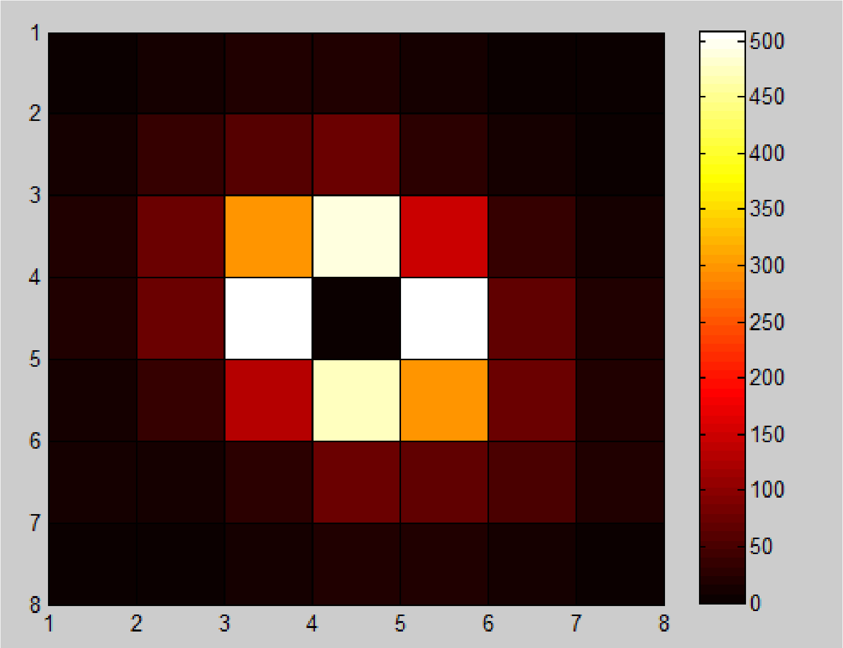

Figure B.13: Double interactions matrix (a) and Q distribution fitted to a cos(2θ) function for a 60% polarized beam with its polarization vector at 45°.

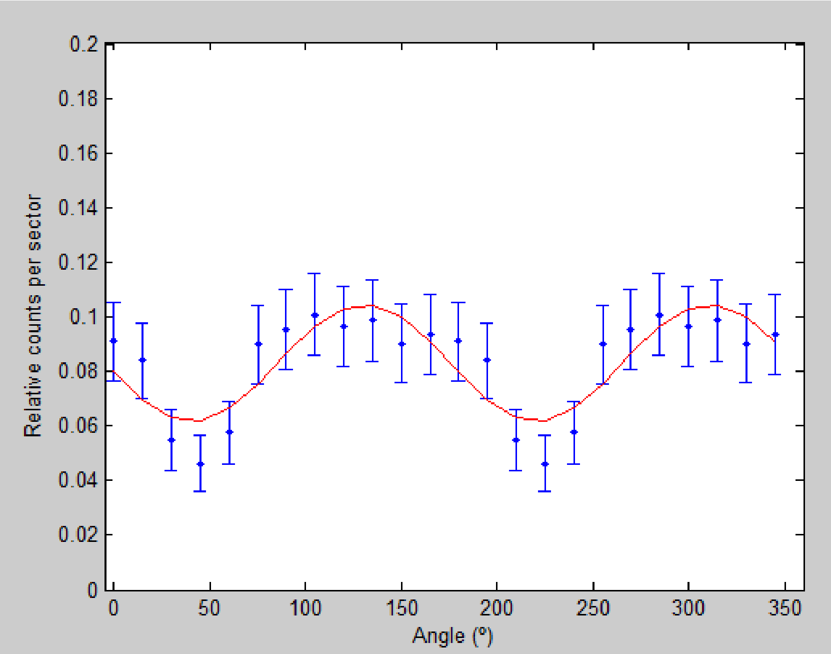

Figure B.14: N distribution fitted to a cos(2θ) function for a 60% polarized beam with its polarization vector at 45°.

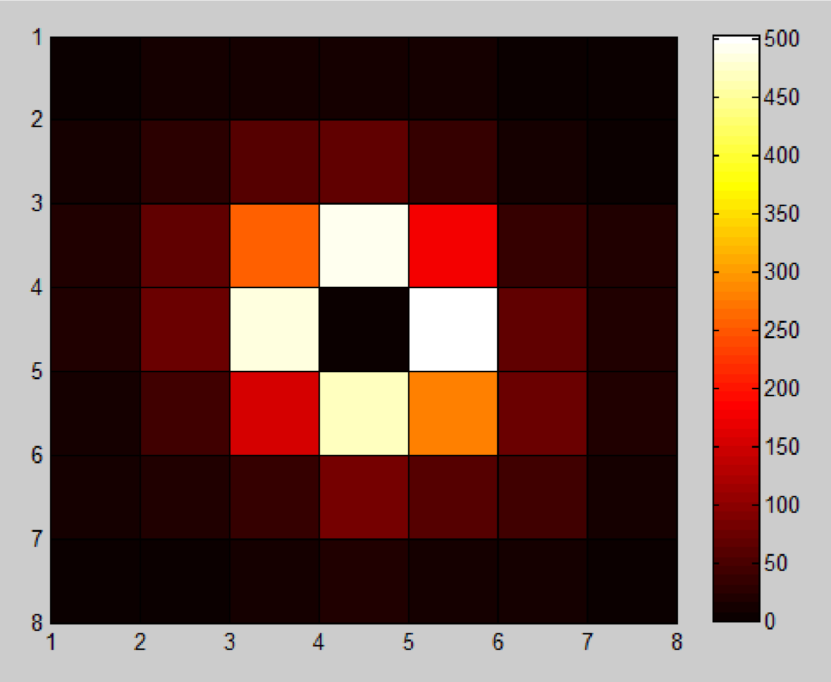

Figure B.15: Double interactions matrix (a) and Q distribution fitted to a cos(2θ) function for a 0% polarized beam with its polarization vector at 45°.

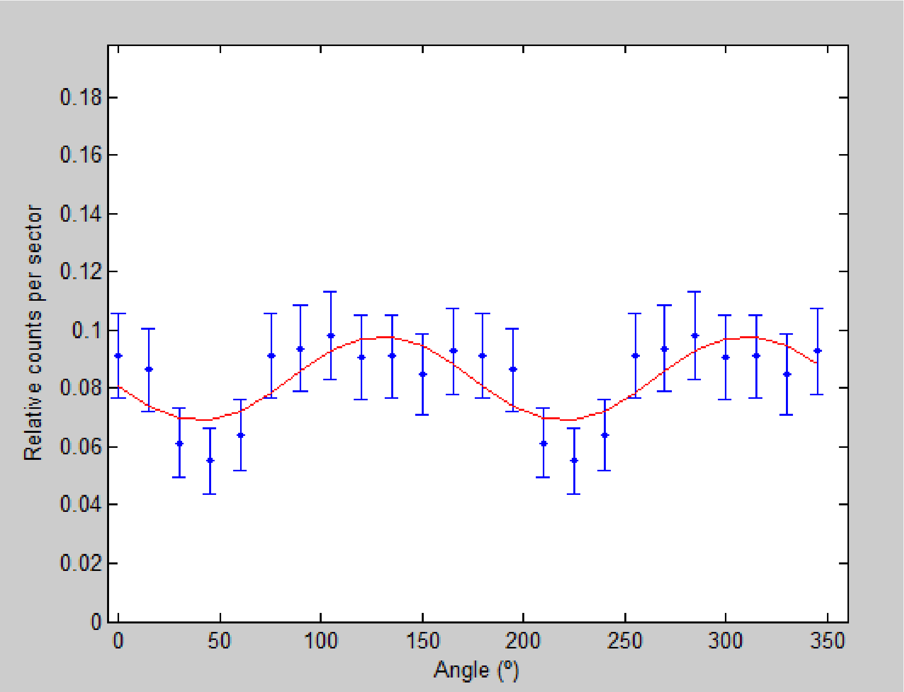

Figure B.16: N distribution fitted to a cos(2θ) function for a 40% polarized beam with its polarization vector at 45°.

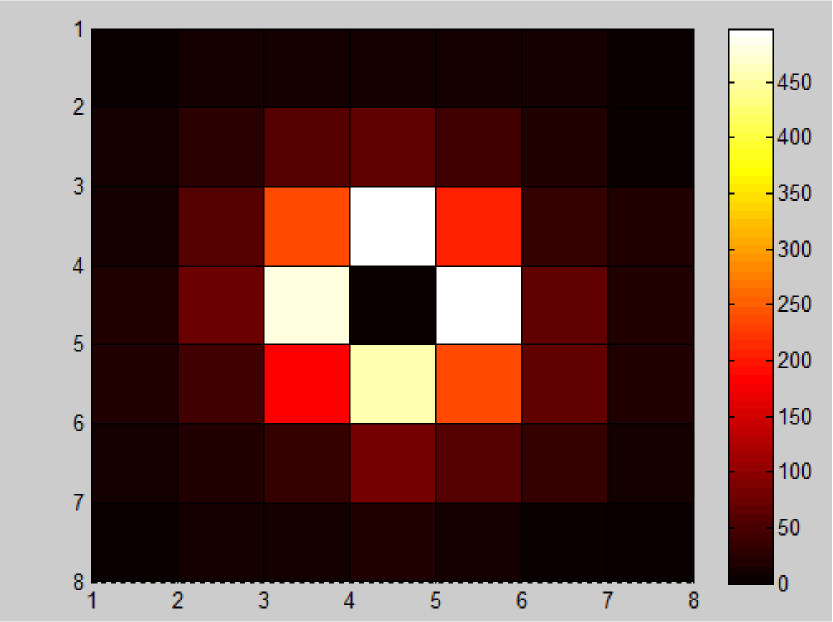

Figure B.17: Double interactions matrix (a) and Q distribution fitted to a cos(2θ) function for a 20% polarized beam with its polarization vector at 45°.

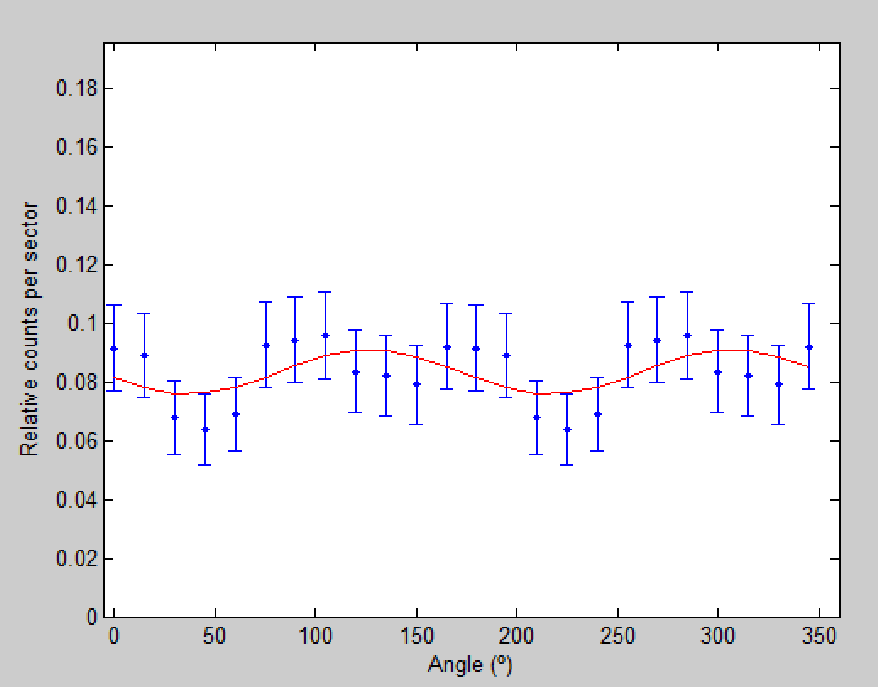

Figure B.18: N distribution fitted to a cos(2θ) function for a 20% polarized beam with its polarization vector at 45°.

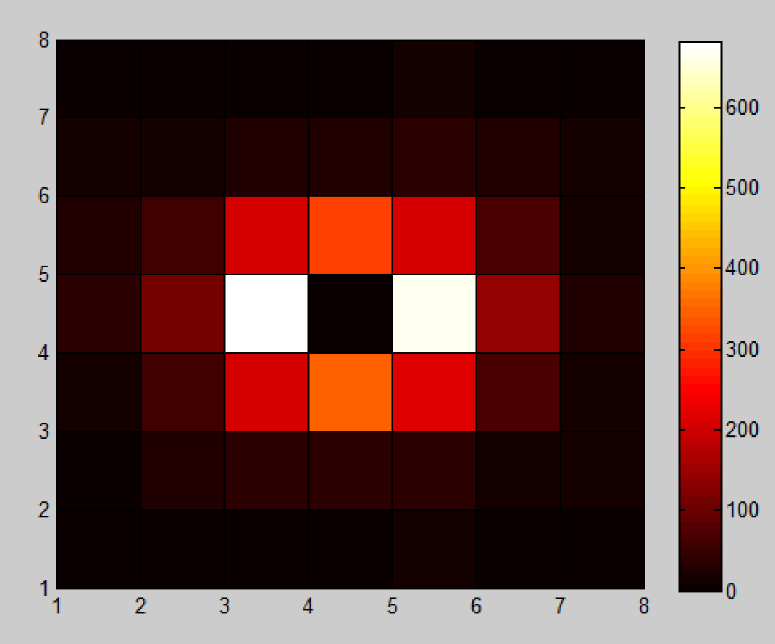

Figure B.19: Double interactions matrix (a) and Q distribution fitted to a cos(2θ) function for a 100% polarized beam with its polarization vector at 90.

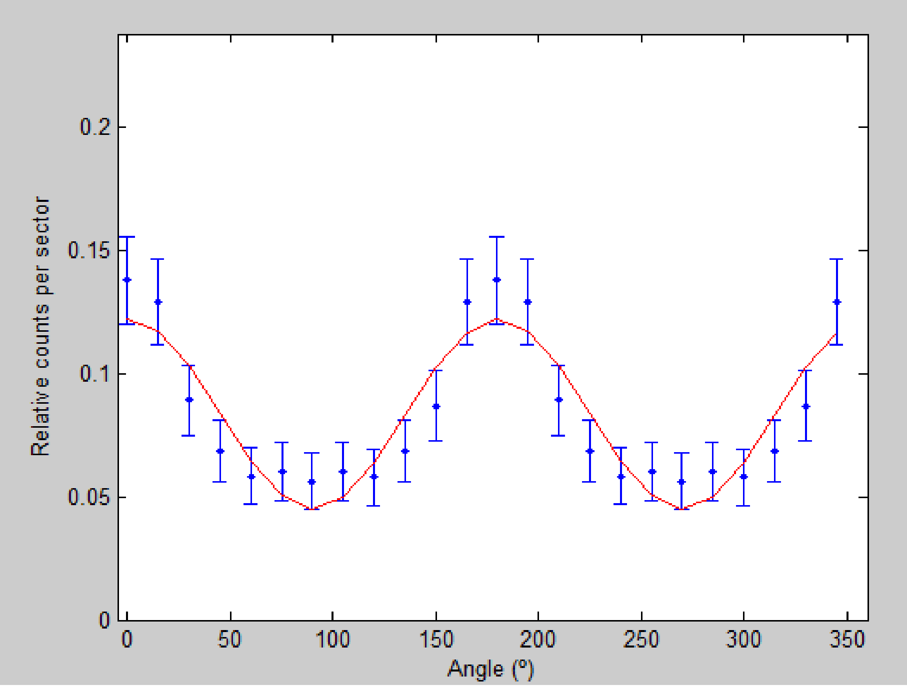

Figure B.20: N distribution fitted to a cos(2θ) function for a 100% polarized beam with its polarization vector at 90.

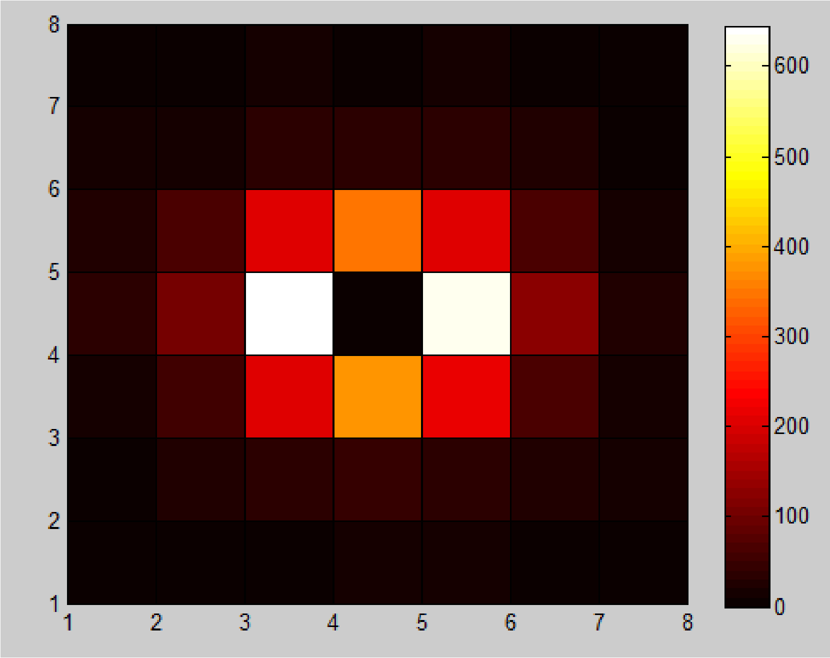

Figure B.21: Double interactions matrix (a) and Q distribution fitted to a cos(2θ) function for a 80% polarized beam with its polarization vector at 90.

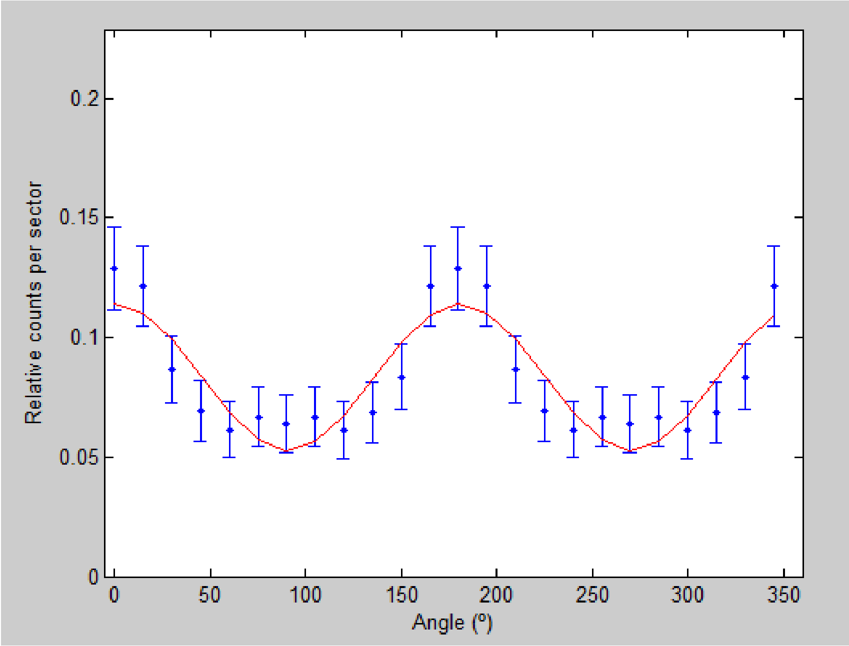

Figure B.22: N distribution fitted to a cos(2θ) function for a 80% polarized beam with its polarization vector at 90.

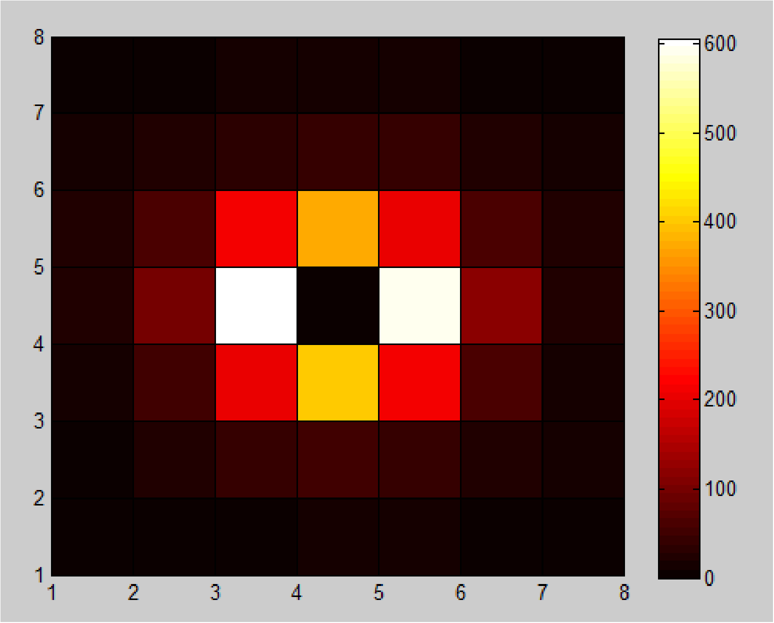

Figure 23: Double interactions matrix (a) and Q distribution fitted to a cos(2θ) function for a 60% polarized beam with its polarization vector at 90.

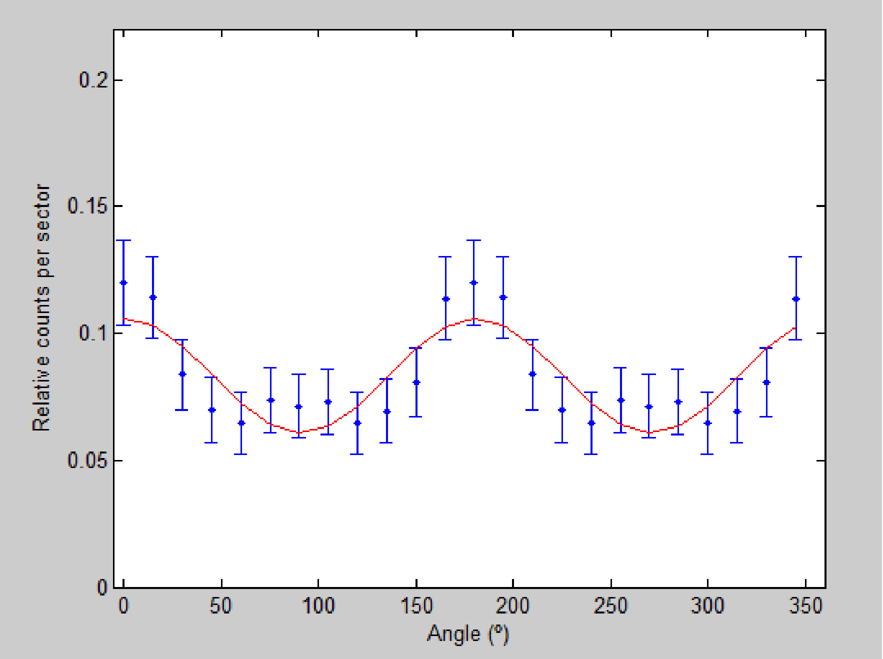

Figure B.24: N distribution fitted to a cos(2θ) function for a 60% polarized beam with its polarization vector at 90.

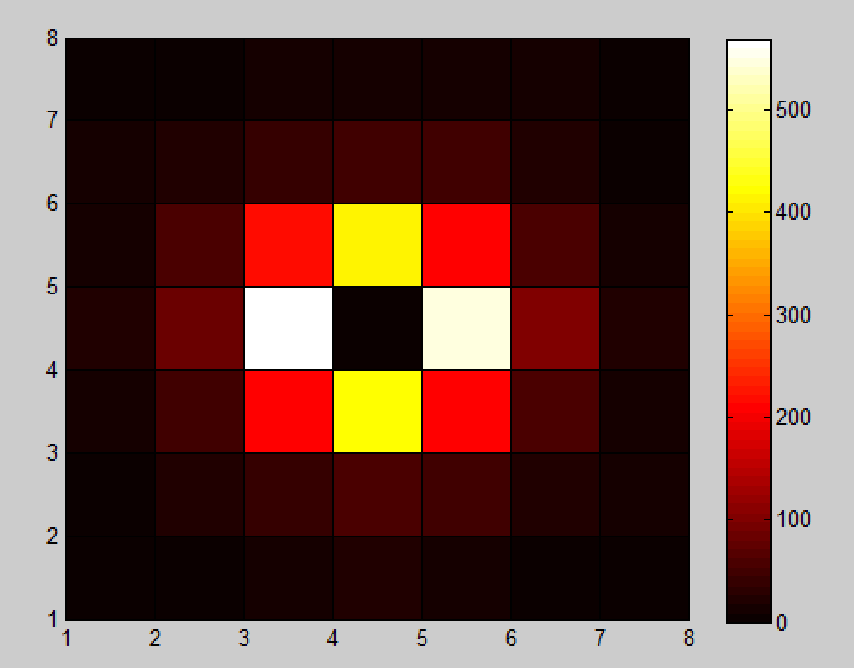

Figure B.25: Double interactions matrix (a) and Q distribution fitted to a cos(2θ) function for a 0% polarized beam with its polarization vector at 90°

.

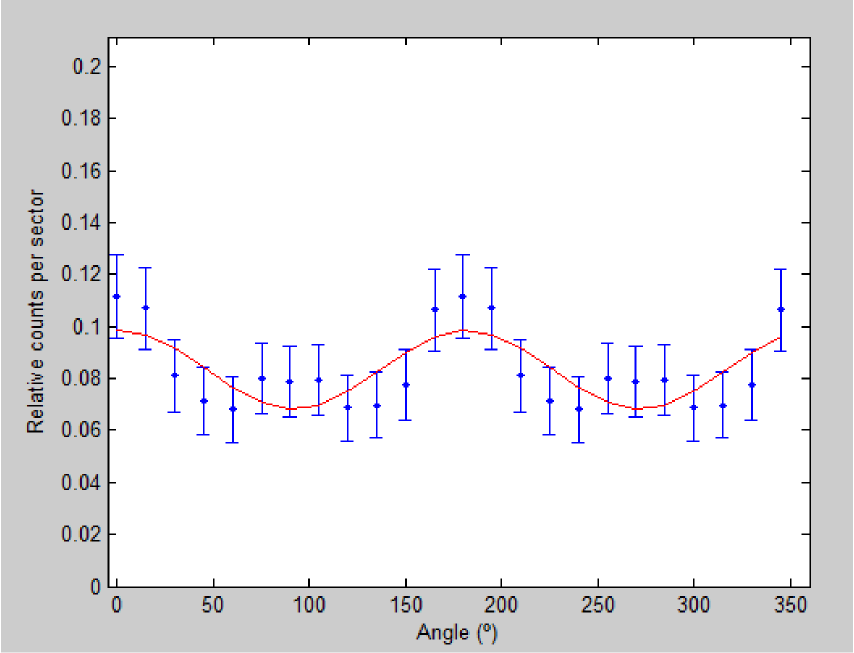

Figure B.26: N distribution fitted to a cos(2θ) function for a 40% polarized beam with its polarization vector at 90°.

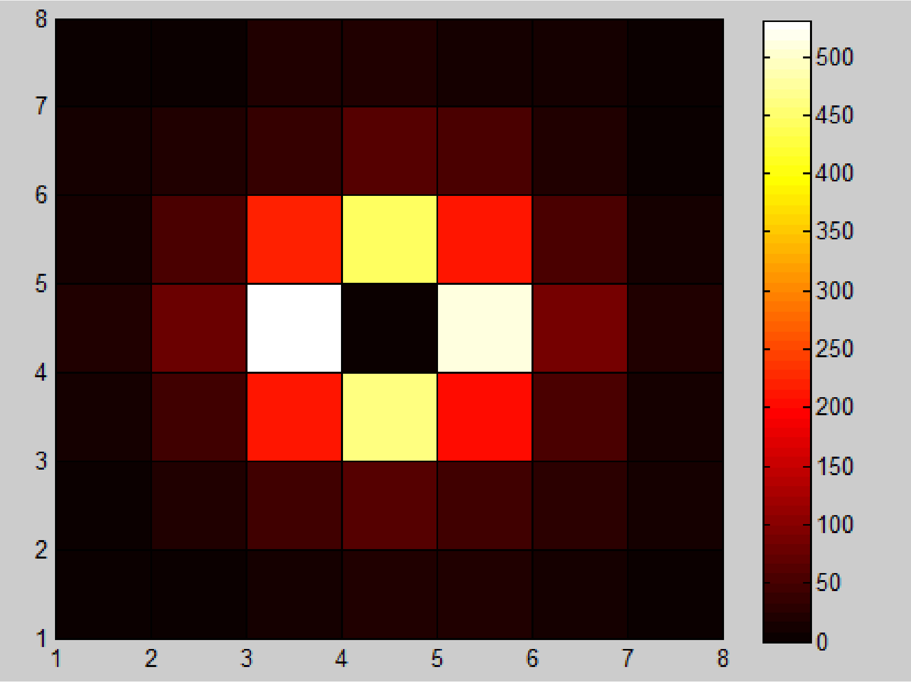

Figure B.27: Double interactions matrix (a) and Q distribution fitted to a cos(2θ) function for a 20% polarized beam with its polarization vector at 90°.

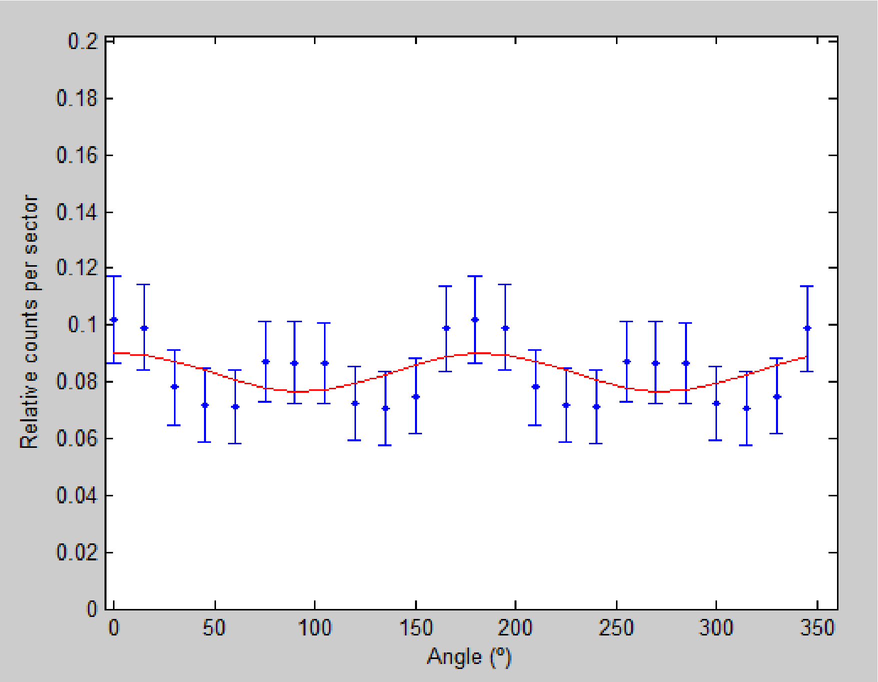

Figure B.28: N distribution fitted to a cos(2θ) function for a 20% polarized beam with its polarization vector at 90°.

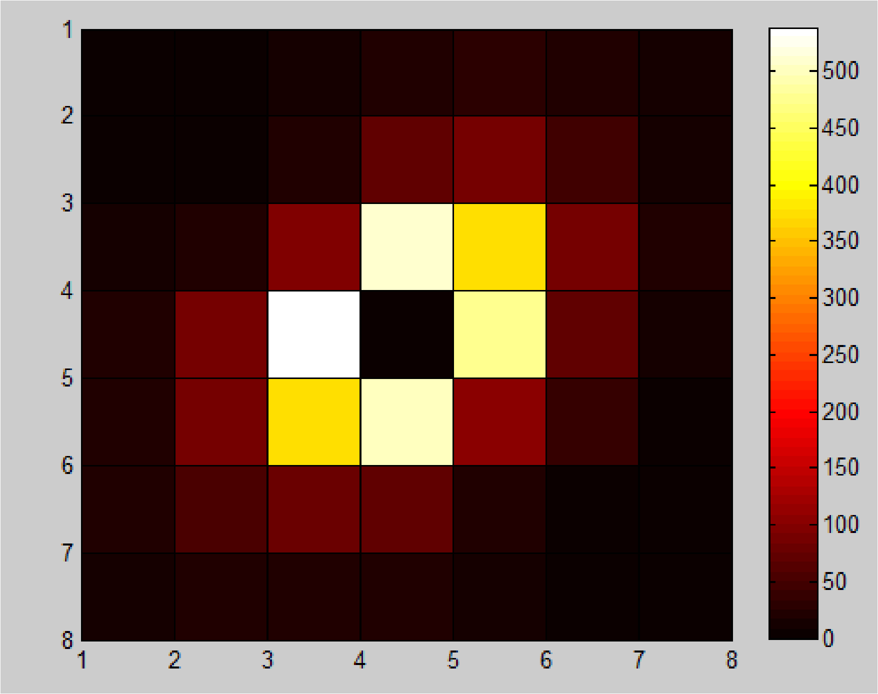

Figure B.29: Double interactions matrix (a) and Q distribution fitted to a cos(2θ) function for a 100% polarized beam with its polarization vector at 135°.

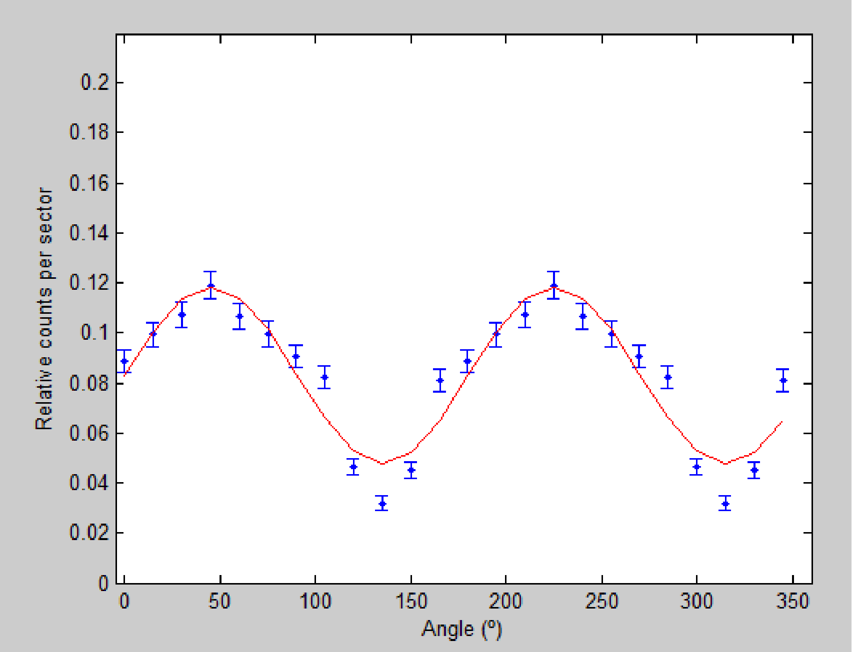

Figure B.30: N distribution fitted to a cos(2θ) function for a 100% polarized beam with its polarization vector at 135°.

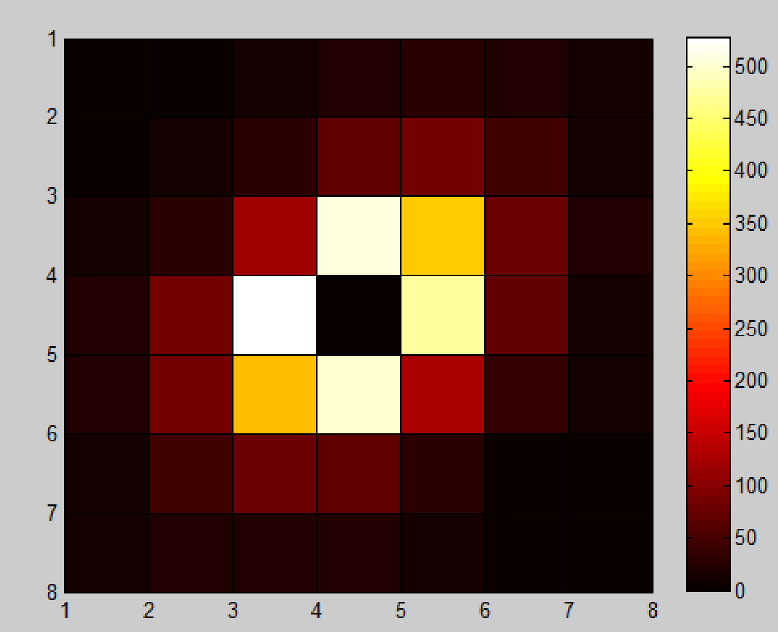

Figure B.31: Double interactions matrix (a) and Q distribution fitted to a cos(2θ) function for a 80% polarized beam with its polarization vector at 135°.

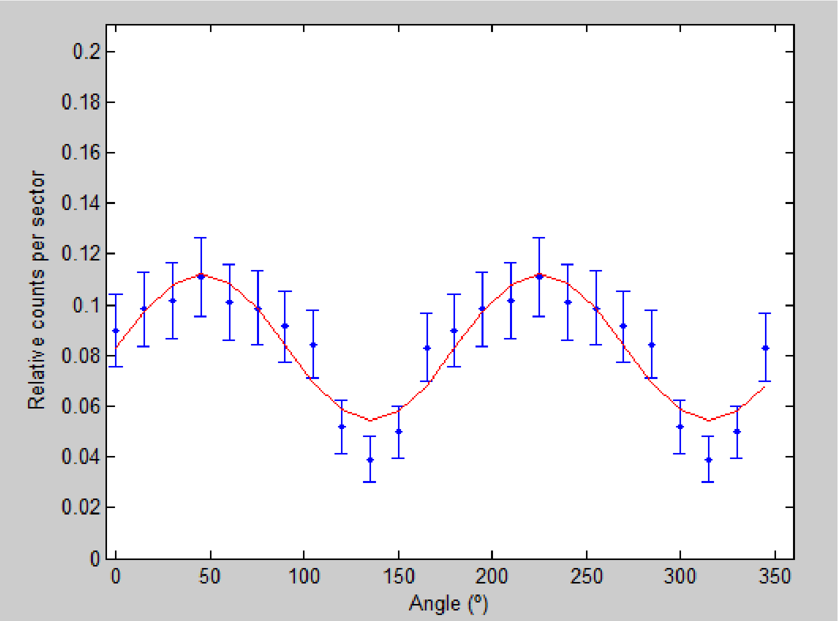

Figure B.32: N distribution fitted to a cos(2θ) function for a 80% polarized beam with its polarization vector at 135°.

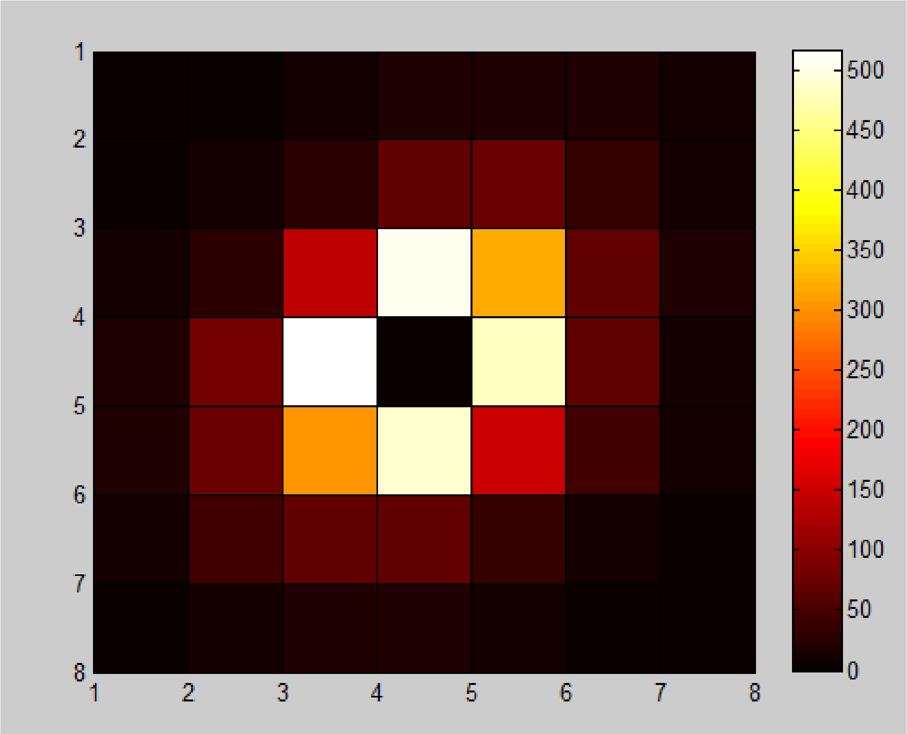

Figure B.33: Double interactions matrix (a) and Q distribution fitted to a cos(2θ) function for a 60% polarized beam with its polarization vector at 135°.

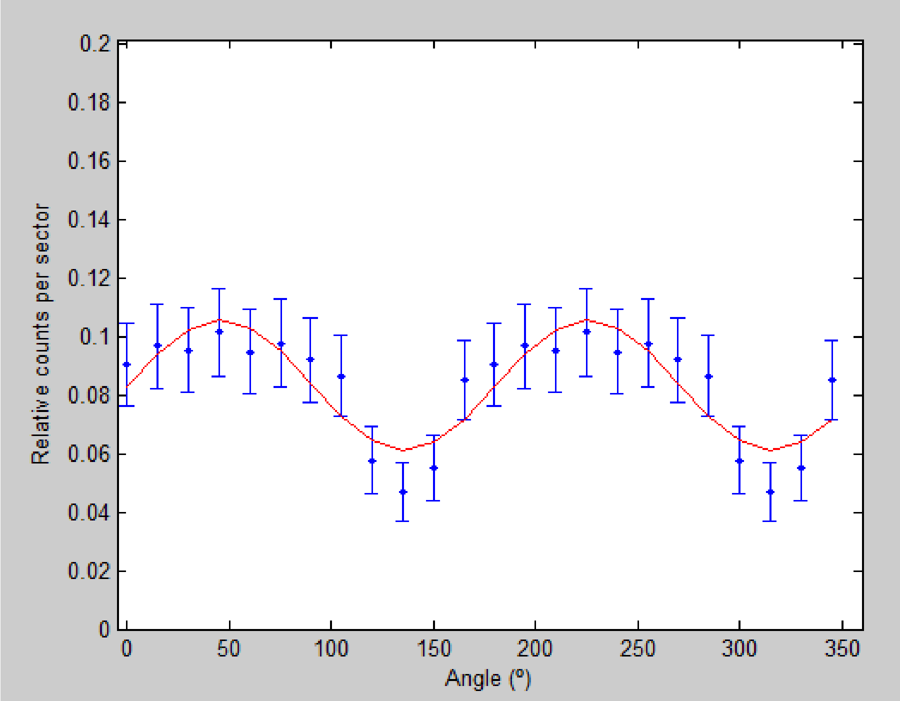

Figure B.34: N distribution fitted to a cos(2θ) function for a 60% polarized beam with its polarization vector at 135°.

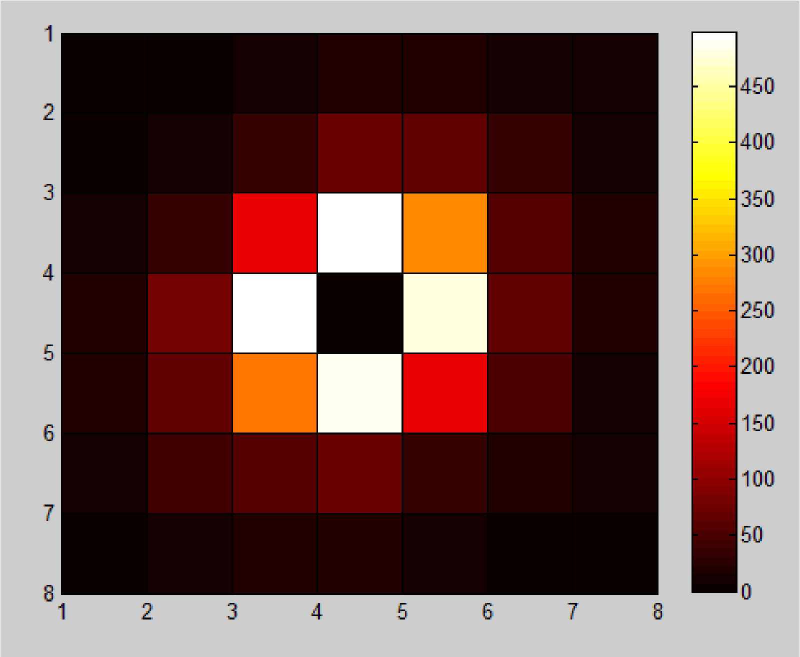

Figure B.35: Double interactions matrix (a) and Q distribution fitted to a cos(2θ) function for a 0% polarized beam with its polarization vector at 135°.

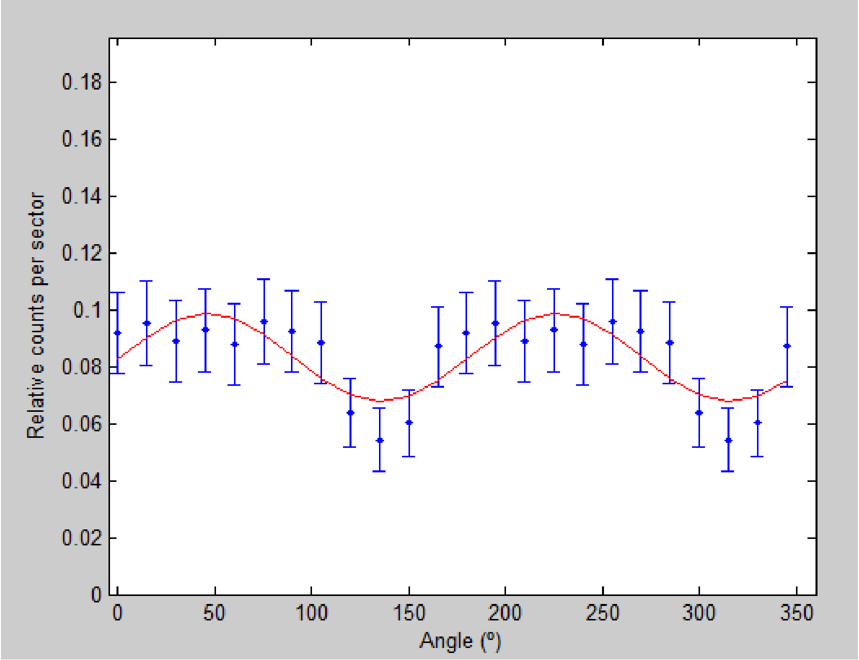

Figure B.36: N distribution fitted to a cos(2θ) function for a 40% polarized beam with its polarization vector at 135°.

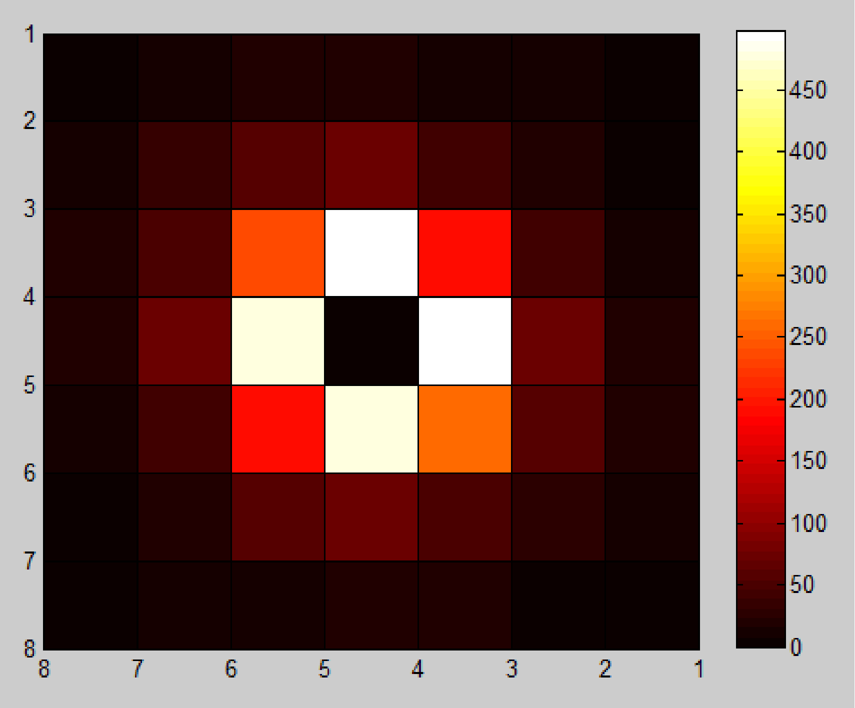

Figure B.37: Double interactions matrix (a) and Q distribution fitted to a cos(2θ) function for a 20% polarized beam with its polarization vector at 135°.

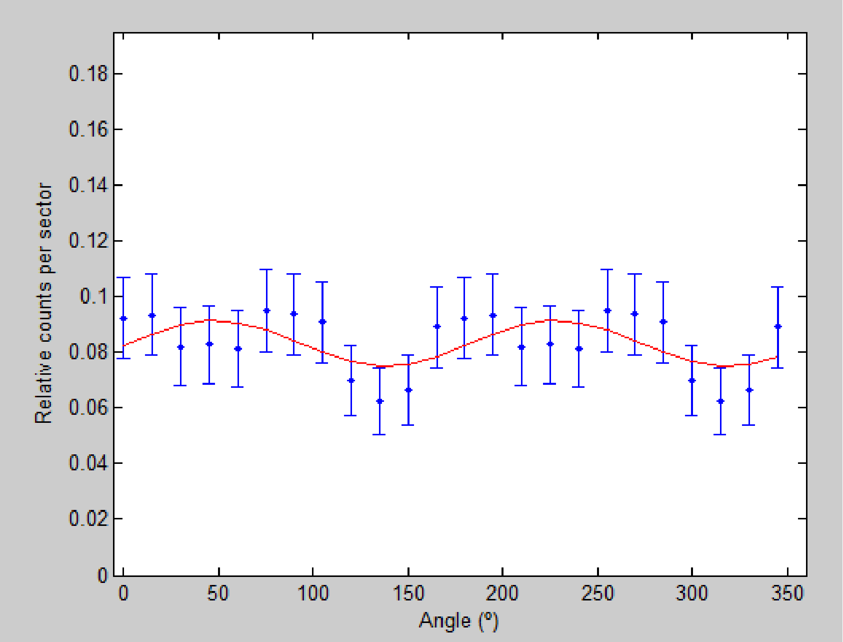

Figure B.38: N distribution fitted to a cos(2θ) function for a 20% polarized beam with its polarization vector at 135°.